Spring 2020

Bulk Properties Correlated to the Hydrogen Bond Organization in Dendrimers, Hyperbranched Polymers, and Linear Polymers

Beibei Chen

BULK PROPERTIES CORRELATED TO THE HYDROGEN BOND ORGANIZATION IN DENDRIMERS, HYPERBRANCHED POLYMERS, AND LINEAR POLYMERS

by

Beibei Chen

A Dissertation
Submitted to the Graduate School,
the College of Arts and Sciences
and the School of Polymer Science and Engineering
at The University of Southern Mississippi
in Partial Fulfillment of the Requirements
for the Degree of Doctor of Philosophy

Approved by:

Dr. Sergei I. Nazarenko, Committee Chair
Dr. Robson F. Storey
Dr. Jeffrey S. Wiggins
Dr. Yoan C. Simon
Dr. Ras B. Pandey

Dr. Sergei I. Nazarenko Committee Chair	Dr. Derek L. Patton Director of School	Dr. Karen S. Coats Dean of the Graduate School

May 2020

ABSTRACT

Although a lot of research was conducted on dendritic polymers, our understanding of their structure-property is still limited. Our previous study, which focused on a family of dendritic polymers based on 2,2-bis(hydroxymethyl) propionic acid (bis-MPA) as a monomer, discovered unique hydrogen bond organizations contributed by their dendritic structures. However, the influence of the H-bond organization on bulk properties has yet to be understood. The goal of this dissertation is to elucidate the correlation between the H-bond organization with the dielectric and volumetric properties of bis-MPA based dendritic polymers, with an emphasis on developing a fundamental understanding of to what extent structural irregularity affects the bulk properties of dendritic polymers.

Chapter I of the dissertation provided a background of dendritic polymers with special focus on those based on bis-MPA, the formation of hydrogen bonding, H-bonded clusters, and the H-bond mediated mesophase in bis-MPA based dendritic polymers, and a brief introduction of dielectric spectroscopy. In Chapter II, the chemical nature, the formation of hydrogen bonding, volumetric, and thermodynamic properties of a bis-MPA based dendrimer and hyperbranched polymer (HPB) were carefully analyzed and compared. In chapter III, the gamma-relaxation of both the dendrimer and HBP was investigated via dielectric spectroscopy, where unique dielectric properties, such as high dielectric constant, were observed, especially for the dendrimer. Via molecular dynamics simulation, unique dielectric properties were ascribed to the formation of the H-bonded clusters. In chapter IV, combined with dynamic mechanic analysis, the relaxation of both the dendrimer and HBP detected at high temperatures by dielectric spectroscopy was

ascribed to the proton hopping through hydrogen bonds via the Grotthuss mechanism. The influences on H-bonded clusters on the proton hopping process were also analyzed. In Chapter V, the study of the correlation between hydrogen bonding formation and bulk properties was extended to a linear copolymer system based on dimethanol-functionalized norbornene. It was discovered that the formation of hydrogen bonding, which is affected by the stereochemistry of the monomer, plays an important role in defining the gas barrier property of the copolymers.

ACKNOWLEDGMENTS

First, I would like to thank my advisor, Dr. Sergei Nazarenko, for offering his support and guidance throughout my entire Ph.D. study. His critical thinking and enthusiasm for science inspire me to be a good researcher. I thank him for getting me involved in a variety of projects, from practical engineering to fundamental science, which allows me to develop different kinds of skills for my future career.

I want to thank my committee members, Dr. Robson Storey, Dr. Jeffery Wiggins, Dr. Yoan Simon, and Dr. Ras Pandey, and other faculty members, for their guidance and contribution to my education.

I would like to thank Dr. Mohamed K. Hassan for his kindness and patience in offering me excellent training on dielectric spectroscopy and sharing with me his rich experience in dielectric studies.

I would acknowledge Dr. Brain Olson for all his support and guidance on my computer simulation work. I thank him for writing and sharing the modeling scripts, helping me through all the simulation problems, and answering all my stupid questions.

I am so grateful to all my previous and present colleagues in the Nazarenko Research Group (NRG). I want to thank Dr. Maliha Syed for her excellent early work for this project and her guidance when I initially joined the group. I'd like to thank Dr. Kevin Meyers, Dr. Ramesh Ramakrishnan, Dr. Vivek Vasagar, Jacob Schekman, Karina Reynolds, Samantha Daymon, and Mustafa Zagho for being both excellent colleagues and good friends. I appreciate all their technical and mental supports.

I would also thank all my first-year classmates, friends, and colleagues in the School of Polymer Science and Engineering for being so generous and helpful.

I’d like to thank our assistant of research grants, Ms. Jody, for being so kind, joyful, and hard working. I really appreciate all her work for keeping this lab functioning properly so that we all can focus on our projects.

Finally, I gratefully acknowledge the financial supports from Petroleum Research Fund administrated by the American Chemical Society (ACS), National Science Foundation (NSF), Bryce Corporation, and ExxonMobil Corporation.

DEDICATION

This dissertation is dedicated to my mother and father, Xiaoxia Cui and Feng Chen, who gave me the endless support to complete this dissertation.

TABLE OF CONTENTS

LIST OF TABLES

LIST OF ILLUSTRATIONS

LIST OF SCHEMES

CHAPTER I - RESEARCH BACKGROUND

1.1 Introduction

Dendritic polymers drive a lot of research interests on their structure-property relationships due to their unique properties such as interior cavities, low viscosity, and high solubility as compared to their linear counterparts.[1-4] Dendrimers and hyperbranched polymers (HBPs) are the two main subclasses of dendritic polymers. Since the preparation of the monodispersed dendrimers requires a lot of synthetic efforts, HBPs were utilized as the cheap substitutes of dendrimers in many applications involving large quantities of materials due to their lower cost of synthesizing.[5] Thus, an understanding of how the properties of HBPs different from those of dendrimers, is imperative.

Among various dendritic polymer systems, one class of dendritic polymers based on 3-hydroxy-2-(hydroxymethyl)-2-methyl propionic acid (bis-MPA) has received particular interests.[6, 7] Previous studies have revealed the formation of hydrogen-bonded clusters and hydrogen bond mediated mesophase in bis-MPA based dendritic polymers, and their relationship with the volumetric properties, however, the corresponding experimental study on dendrimers has yet to be completed. On the other hand, dielectric studies conducted on bis-MPA based HBPs demonstrated that secondary relaxation processes were strongly affected by hydrogen bonding interaction in systems. However, how H-bonds define the secondary relaxations has not been well explained. There should be a correlation between the dielectric relaxations and hydrogen-bonded clusters, which needs to be carefully studied. The purpose of this dissertation was to elucidate the correlation between the H-bond organization with the dielectric and volumetric properties of bis-MPA based dendritic polymers, with an emphasis on developing a fundamental

understanding of to what extent structural irregularity affects the bulk properties of dendritic polymers.

1.2 Dendritic polymers

Dendritic structures are one of the most prevalent topologies in both abiotic (lighting patterns, snowflakes) and biological systems (trees, nerve cells). However, they were introduced into the synthetic polymer world only about four decades ago as one of the four main classes of polymer structural organization along with linear, cross-linked, and chain-branched architectures.[8,9] Dendritic polymers are now defined as highly branched, starburst-shaped macromolecules with nanometer-scale dimensions. With their three-dimensional core-shell structures, dendritic polymers exhibit unique properties, such as interior cavities, low viscosity, and high solubility, as compared to their linear counterparts, which drive a lot of research interests on their structure-property relationships.[1-4]

Among the broad range of dendritic structures that have been reported, dendrimers and hyperbranched polymers (HBPs) are the two main subclasses.[8-10] Dendrimers are perfectly monodispersed molecules with regular branching structures. As shown in Figure 1.1, the structure of a dendrimer is defined by three components: a central core, interior layers (generations) composed of repeating units, and an exterior surface composed of numerous functional groups.[11] The first polymeric dendrimers, poly(propylene imine) (PPI), were synthesized by Vögtle's group in 1978.[12] However, the discovery of true monodispersed 'core-shell-periphery' dendrimers is credited to

Tomalia's group, who reported on the synthesis of poly(amidoamine) (PAMMA) dendrimers, and Newkome's group who reported on the synthesis of "arborol" systems, a synonymous term for dendrimers in 1985.[13, 14] The well-controlled molecular size, shape, and disposition of functionalities of dendrimers make them ideal candidates for applications in sensing and nanomedicine.[15-18]

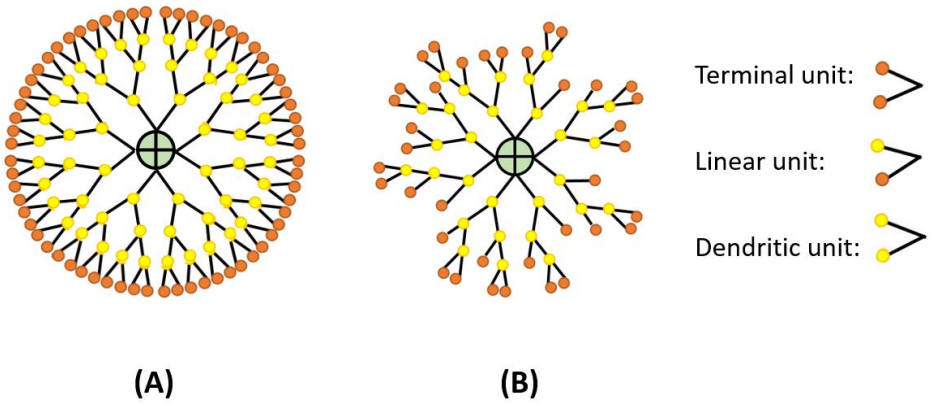

Figure 1.1 *Schematic presentation of an (A)dendrimer, a (B) hyperbranched polymer. Dendritic (D), terminal (T), and linear (L) structural unit types are shown to the right.*

Since labor-intensive procedures are typically required for synthesizing monodispersed dendrimers, hyperbranched polymers (HBPs), which can be prepared more easily, often using the one-pot approach, have received increasing interests.[19] In contrast to dendrimers, HBPs are poly-dispersed molecules with randomly branched structures.[3, 8, 9] With their irregular structures being halfway between linear and perfectly branched structures, hyperbranched macromolecules retain the main features of dendritic macromolecules and show properties intermediate to those of dendrimers and linear polymers.[10, 20] The first two classes of HBPs are the polyphenylene-based HBPs synthesized by Kim, etc. and the polyester-based HBPs prepared by Hawker, etc. in the

early 1990s.[19, 21] Due to their simple one-pot or pseudo-one pot synthetic methods, HBPs have found broad applications in industrial fields like coatings as well as high-tech fields like drug delivery. [17, 22, 23]

To better describe the branching perfection of the HBP structure, the average degree of branching (DB) was introduced. DB was defined by Frechet and Frey as:

$$DB_{Frechet} = \frac{D + T}{D + L + T} \quad (1)$$

$$DB_{Frey} = \frac{2D}{2D + T} \quad (2)$$

where the D, T, L is the molar fraction of the dendritic, terminal, and the linear units respectively in a polymer system based on AB_2 monomers (Figure 1.1).[19, 24] Despite the different definitions, DB for HBPs is between 0 and 1, and that for perfect dendrimers equals to 1. The definition by Frey was used in this dissertation as it was suggested to be more accurate for low-molar-mass HBPs. [6, 24]

1.3 Bis-MPA based hydroxylated hyperbranched polymers and dendrimers

Among various dendritic polymer systems, one class of dendritic polymers based on 3-hydroxy-2-(hydroxymethyl)-2-methyl propionic acid (bis-MPA) has received particular interests.[6, 7] As bis-MPA is chemically stable to decarboxylation and dehydration and readily available in bulk quantities, it has been extensively utilized as the building block for dendritic polymers. Efficient syntheses have been reported for both bis-MPA based HBPs and dendrimers via the one-pot method and the iterative method respectively. [25-28] Since both bis-MPA based HBPs and dendrimers show high solubility, biocompatibility, and biodegradability, they have been proposed for a range of

biomedical applications.[22, 23, 29, 30] Meanwhile, the bis-MPA based HBPs have been commercialized by Perstop® since the early 1990s and sold under the trade name Boltorn™, to the market for many industrial applications, in particular for coatings. [17, 31, 32]

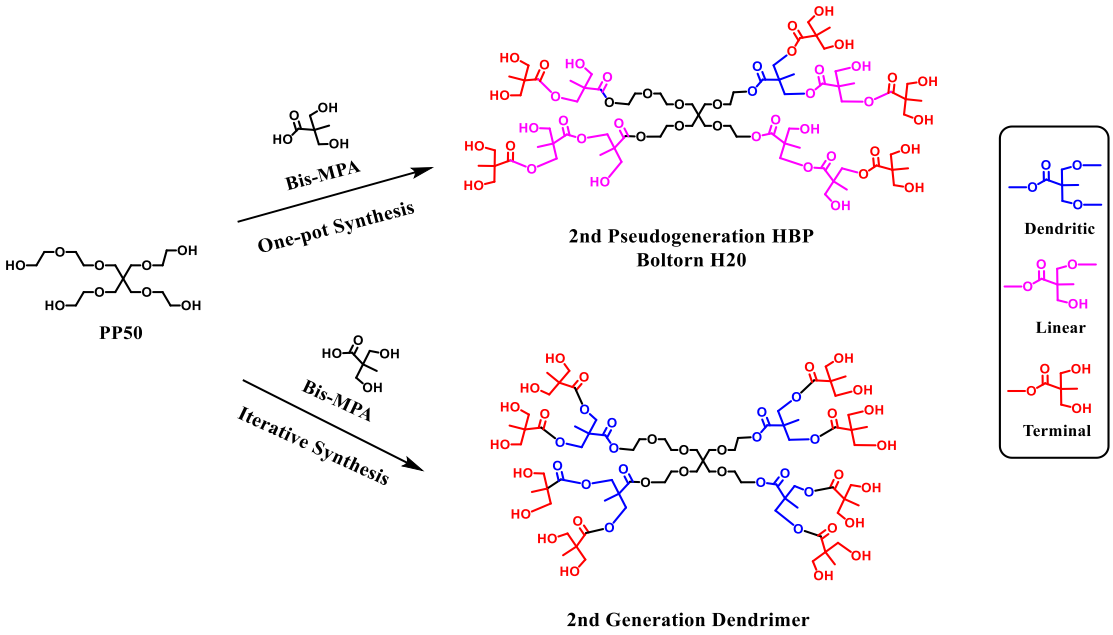

Figure 1.2 *Schematic of the chemical structure of a second-generation hyperbranched polymer (H20) and perfect dendrimer, which are both based on a PP50 core and a bis-MPA branching monomer. Dendritic (D), terminal (T), and linear (L) structural unit types are shown to the right.*

1.3.2 Bis-MPA based HPBs

The 2nd pesudogeneration Boltorn HBP is termed as Boltorn™ H20, where 2 stands for 2nd generation. The structure of Boltorn™ H20 was shown in Figure 1.2, in comparison with its dendrimer analog. Both structures feature bis-MPA repeat units and an asymmetric, tetra-functional PP50 (ethoxylated pentaerythritol) core. Dendritic (D),

terminal (T), and linear (L) structural unit types are also displayed in Figure 1.2. Using the definition by Frey, the DB of H20 was determined as 0.26.[6]

Boltorn HBPs are usually synthesized via a pseudo-one-pot method where stoichiometric amounts of bis-MPA for each theoretical dendrimer generation are added step wisely.[25, 26] As shown in Scheme 1.1, corresponding amounts of bis-MPA monomers for the first generation are firstly added to react with the PP50 core. After completion of the first generation, a new portion of the bis-MPA monomers corresponding to each successive generation is added to the resulting reaction mixture.

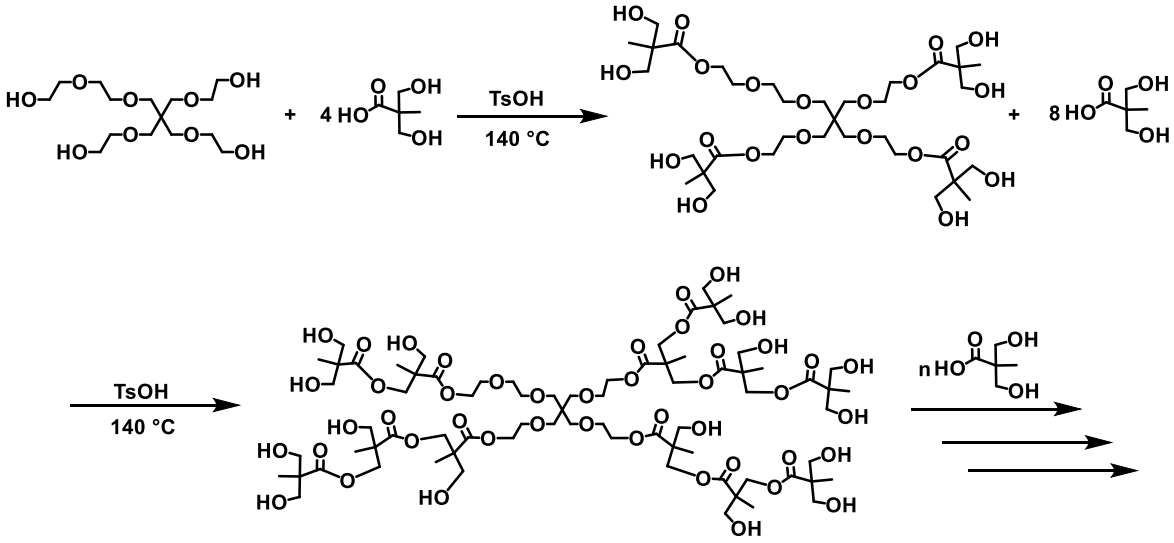

Scheme 1.1 *Pseudo-one pot synthesis of Boltorn hyperbranched polymers based on an ethoxylated pentaerythritol (PP50) core and bis-MPA repeat unit.*

The multifunctional core is used for controlling the polydispersity and preventing gelation. In addition to the PP50, tris(methylol) propane (TMP) is also commonly used as the core for preparing bis-MPA based HBPs. Since the melting point of PP40 and TMP is way below the reaction temperature, the bis-MPA monomer, of which melting point is above 180°C, will be phase-separated from the reaction mixture until the reaction

proceeds.[33] This leads to slow monomer addition. Other than the commonly used PP50 and TMP, di(trimethylolpropane) (Di-TMP), pentaerythritol (PE), 1,3,5-tris(2-hydroxyethyl) cyanuric acid (THECA), and glycerol were also employed as the core molecules for bis-MPA based HBPs (Figure 1.3).[34-36]

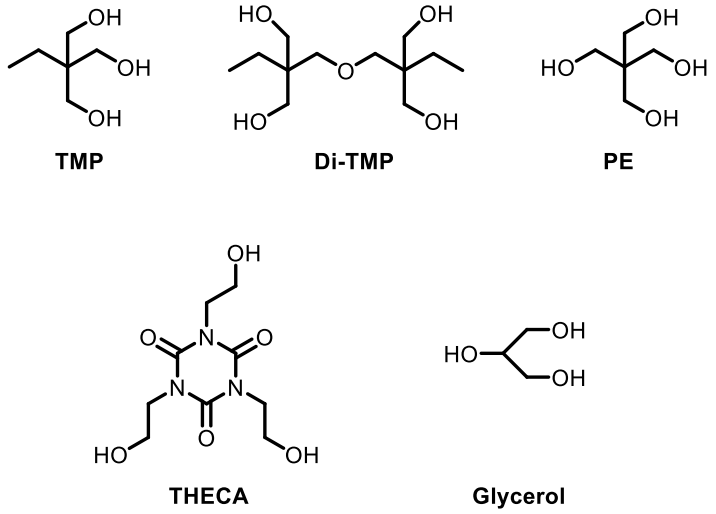

Figure 1.3 *Structures of different core molecules used in the synthesis of bis-MPA based HBPs.*

1.3.3 Bis-MPA based dendrimers

In contrast to bis-MPA based HBP, which are polydispersed and require no workup, dendrimers require robust chemical reactions for addition, protection, and deprotection coupled with tedious purification procedures. Though several fast and convenient synthetic routes have been developed for bis-MPA based dendrimers, they are only available on a multi-gram scale.[7, 28, 37] The availability of both polymers explains why the structure-property relationships of bis-MPA based HBPs have been widely studied however corresponding researches on dendrimers are usually missing.

Shown in Scheme 1.2 is the divergent synthetic approach designed by Ihre, etc., where the diol groups of bis-MPA are firstly protected by reacting with benzaldehyde dimethyl acetal catalyzed with p-toluenesulfonic acid (TSOH) in dry acetone. Then, the anhydride product (ii) will be prepared by self-condensation of the compound (i) in methylene chloride (CH_2Cl_2) in the presence of a coupling agent N, N'-dicyclohexylcarbodiimide (DCC). Coupling of (ii) to pentaerythritol (PE) core is conducted in a solvent mixture of pyridine and CH_2Cl_2 using 4-(dimethylamino) pyridine (DMAP) as an acylating agent to yield the protected first-generation dendrimer (iii). The final dendrimer, G1, will be obtained via hydrogenolysis of (iii) catalyzed by Pd/C. Higher generations of dendrimers can be prepared by repeating the steps of anhydride coupling and hydrogenolysis deprotection.

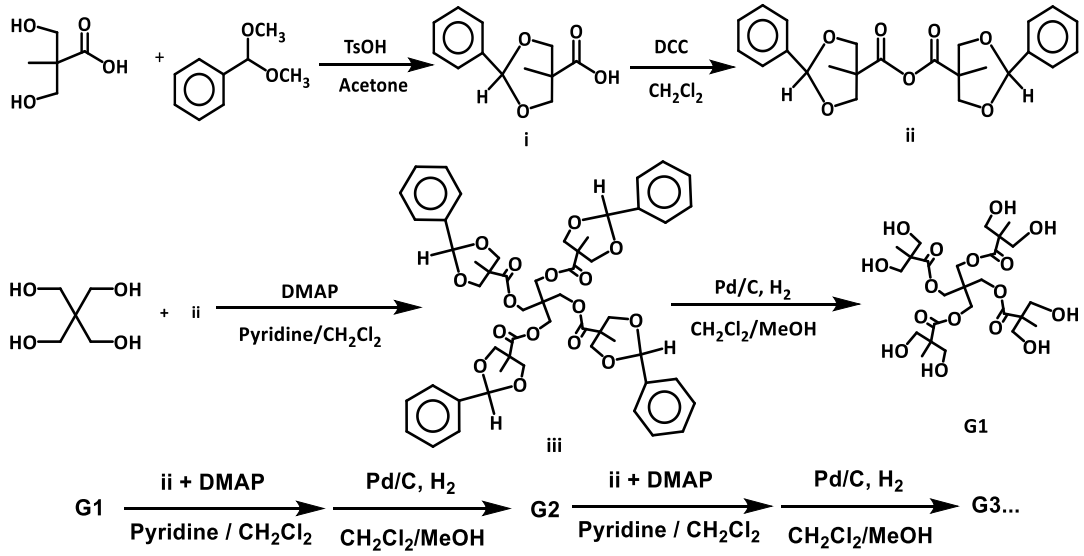

Scheme 1.2 *The divergent approach of synthesizing perfect dendrimers using an acetal-protected anhydride derivative of bis-MPA as an acylating agent.*[28]

1.4 Hydrogen bonding, hydrogen-bonded clusters, and hydrogen bonding mediated mesophase in bis-MPA based dendritic polymers

1.4.1 Hydrogen bonding

Due to the high concentration of hydroxyl groups, the bis-MPA based dendritic polymers are capable of forming extensive intra- and inter-hydrogen bonds within the systems. These H-bonds play an important role in defining the bulk properties of bis-MPA based polymers. This was most clearly demonstrated in the past by the derivatization of bis-MPA based HBPs with non-hydrogen bonding moieties. For example, Boltorn HBPs, which are solids at room temperature, turned into viscous liquids after the peripheral OH groups were replaced by short fatty acids.[38] Early studies also revealed that the formation of hydrogen bonding also strongly affects the structural ordering, rheological properties and relaxation processes.[39-42]

FTIR studies conducted by Zagar discovered that different types of H-bonds were formed in Boltorn HBPs, where the those between hydroxyls and between hydroxyls and carbonyls were found to be the dominant types, which are denoted as OH···OH and OH···C=O respectively.[43] Higher fraction of OH ··OH H-bonds were found in Boltorn™ H20 as compared to H40, which was attributed to higher concentration of terminal units in H20.[42, 43] This suggests that the structural differences between the HBPs and dendrimers may also be reflected in the fraction of OH···OH and OH···C=O H-bonds.

1.4.2 H-bonded chain-like clusters

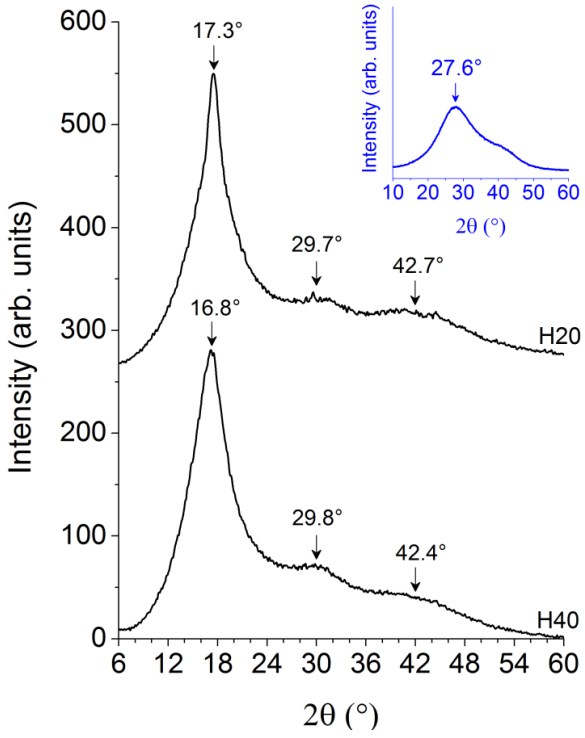

Figure 1.4 *Wide-angle X-ray diffraction (WAXS) patterns of Boltorn™ H20 and H40. Inset is the WAXS pattern of D.I. water.*[44]

In our previous study, the reflection at $2\theta \approx 30°$ on the WAXS patterns of the bis-MPA based dendritic polymers was found to be similar to the main amorphous halo on the WAXS of the D.I. water, which is at $2\theta \approx 28°$. The WAXS patterns of Boltorn™ H20 and H40 were shown as examples in Figure 1.4 with that of D.I. water displayed in the inset. It had been reported that the amorphous halo of D. I. water was originated from the ordering of oxygen atoms within three-dimensional H-bonded clusters which are pervasive in water. [45-47] Similarly, we discovered that the reflection peak at $2\theta \approx 30°$ of

bis-MPA based dendritic polymers was contributed by the short-range ordering of oxygen atoms associated with the H-bonded chain-like clusters of terminal hydroxyls in dendritic polymer systems.[44] As shown in Figure 1.5, the H-bonded chain-like clusters are formed by multiple consecutive O-H···O groups connected via H-bonds. Similar clustering structures were observed in small molecule H-bond formers, e.g. liquid hydrogen fluoride.[48, 49] It appears that longer chain-like clusters do not form in linear hydroxylated polymers due to the steric constraints imposed by the linear backbone.

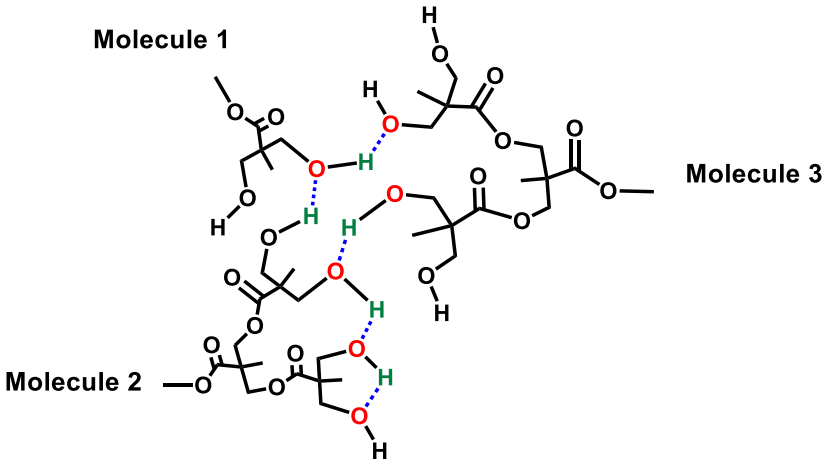

Figure 1.5 *Schematic of hydrogen-bonded clusters formed by OH···O groups. Acceptor oxygen atoms are highlighted in red and the donor hydrogen atoms are highlighted in green. For all structures shown, dotted lines represent hydrogen bonds and solid lines represent covalent bonds.*

1.4.3 Hydrogen bond mediated mesophase

In addition to the reflection at $2\theta \approx 30°$, another characteristic ordering feature of Boltorn HBPs is the sharp peak which can be observed at $2\theta \approx 17°$ on the WAXS patterns. (Figure 1.4) Early researches had discovered that that sharp peak was correlated to a structure ordering phenomenon mediated by H-bonds formed between long linear

segments in the Boltorn HBPs.[39, 50] In our previous work, we revealed that that sharp peak was superimposed on the broad amorphous halo of Boltorn HBPs, which was corresponding to the short-range order between C-C and C-O close packed atoms in the bulk of the polymer.[51] The origin of the narrow peak was assigned to the pseudo-hexagonal mesophase formed by linear segments.[44] (Figure 1.6) Compared with the three-dimensional ordering in the crystalline phase, the mesophase exhibits a two-dimensional ordering which was enthalpically driven by H-bonding without conformational ordering along the linear chain segments. The formation of mesophase is temperature-dependent and the size of which increases with the annealing time.[44]

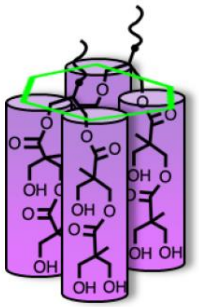

Figure 1.6 . *Schematic of the pseudo-hexagonal packing structure of mesophase formed by linear chain segments in Boltorn HBPs. The shape of each linear chain segment was approximated as cylindrical.*[44]

1.5 Dielectric property and dielectric spectroscopy

1.5.1 Dielectric property

The dielectric property, which is generally referring to the permittivity (ε), is a measure of the polarizability of a material when exposed to the electric field. When an external electric field is applied to a dielectric material, dipoles inside the material will be polarized, generating an opposite internal electric field, which reduces the overall

electrical field. The response of the dipoles to the external electric field (**E**) is described by the electric displacement (**D**), which is the total charge density induced at the electrodes.[52] The relationships between **E** and **P** can be described using the following equation.[53]

$$\boldsymbol{D} = \varepsilon_0 \boldsymbol{E} + \boldsymbol{P} \quad (3)$$

where ε_0 =8.854×10^{-12} F/m, which is the permittivity of the vacuum. **P** is the polarization density, which is the density of the dipole moments in the material. In a homogeneous, linear, non-dispersive, and isotropic dielectric medium, **P** is proportional to **E**:[54]

$$\boldsymbol{P} = \varepsilon_0 \chi \boldsymbol{E} = \varepsilon_0 (\varepsilon_r - 1) \boldsymbol{E} \quad (4)$$

$$\boldsymbol{D} = \varepsilon \boldsymbol{E} = \varepsilon_0 \varepsilon_r \boldsymbol{E} \quad (5)$$

where χ is the electric susceptibility of the material. ε and ε_r are the absolute and the relative permittivity of the material, respectively. ε_r is also denoted as the dielectric constant for common usage. Since relative permittivity is much more commonly used than the absolute value, ε is usually used for representing relative permittivity instead.

The dielectric constant is strongly dependent on the polarity of the material. For instance, at 20 °C, dielectric constants of n-hexane and benzene are around 2, whereas those for benzonitrile, water, and methanol, are around 26, 80, and 30, respectively.[46, 55, 56] Due to the intrinsically low polarity, polymers usually exhibit relatively low dielectric constant as compared to inorganic materials. For instance, at 20 °C, the dielectric constant of polyamide (PA) is ~3 whereas that of magnesium oxide (MgO) and zirconium dioxide (ZrO_2) is about 9 and 25 respectively.[57-59]

Accordingly, the dielectric constants of polymers are dependent on the concentration of dipoles, i.e., polar groups. However, for commonly used polymers, the

differences in ε between polar and non-polar ones are not as significant as those in small molecules. For instance, at room temperature, ε for non-polar polymers, such as polypropylene (PP), is ~ 3, while that for polar polymers, such as polyacrylonitrile (PAN), polycarbonate (PC), and polyvinyl chloride (PVC) is all around 3~5. [57, 59, 60] It is due to the low concentration and lack of interaction between dipoles. Hydroxylated polymer systems, on the other hand, display higher dielectric constant values than those of other polar polymers, which is contributed by hydrogen bonding.[61-63] For instance, under ambient conditions, ε of polyvinyl alcohol (PVA) is around 5~8.[64, 65] It was also discovered that small H-bonded molecules such as D.I. water and methanol, exhibit very high dielectric constant as the molecules form clusters in groups of three.[56, 66, 67] Hence, it is possible that the formation of H-bonded chain-like clusters may also induce special dielectric properties in bis-MPA based dendritic polymer systems.

1.5.2 Dielectric spectroscopy

The dielectric spectroscopy measures the permittivity as a function of frequency under an alternating external electric field. It is a very powerful tool for probing molecular dynamics, especially the secondary relaxation processes in the polar polymers, as the corresponding changes in ε during thermal transitions are quite large, as compared to those in volume, enthalpy, or heat capacity, which measured by other commonly used thermal analysis techniques.[68] Moreover, it can measure the relaxation within very broad range scales of frequency and temperature.

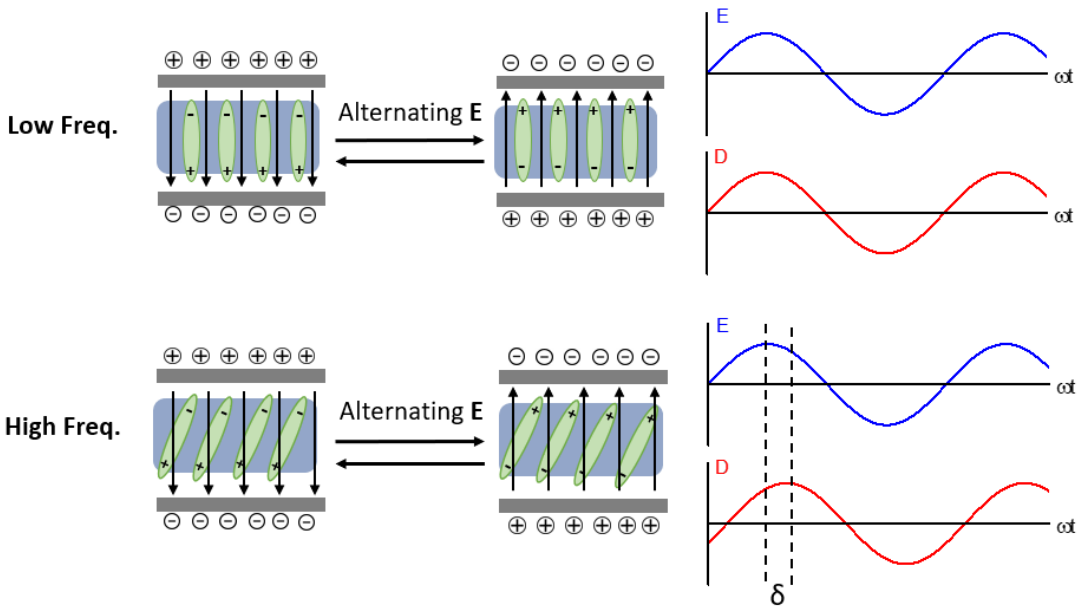

Figure 1.7 *Schematic of the mechanism of the dielectric spectroscopy.*

Figure 1.7 shows the basic mechanism of dielectric spectroscopy for measuring the relaxation processes. When the frequency of the alternating electric field is low, the ε stays constant with frequency changes as the dipole moments can perfectly align with the electric field. As the frequency increases to a certain extent, ε starts to change as the dipoles become unable to follow the electric field instantaneously, which leads to a lag between the orientation of **E** and **P**, which can be represented by a phase difference between **E** and **D** as shown in Figure 1.7. To better describe the frequency dependence of phase lag, ε is expressed in a complexed form: [53]

$$\varepsilon^*(\omega) = \varepsilon'(\omega) - i\varepsilon''(\omega) = \left|\frac{D_0}{\varepsilon_0 E_0}\right| (\cos\delta - i\sin\delta) \qquad (6)$$

where D_0 and E_0 are the amplitudes of the electric displacement and electric field respectively. ε′ and ε″ are the real and imaginary parts of the permittivity respectively. ε′ accounts for the in-phase part of **D**, whereas ε″ describes the out-phase part of **D**. i is the

imaginary unit, $i^2 = -1$. δ is the loss angle. Tan δ is termed as the dissipation factor, which is defined by tan $\delta = \varepsilon''/\varepsilon'$.

Shown in Figure 1.8 is a generic presentation of the frequency dependence of ε′ and ε″ for the relaxation at a constant temperature. [68] The ε_r and ε_u are the permittivity value at relaxed (f→0) and unrelaxed state (f→∞), respectively. It can be observed that when a relaxation takes place, ε′ decays from ε_r to ε_u while on ε″ shows a peak of which the maximum point is positioned at ω equals $1/\tau$, where τ is the characteristic relaxation time. Hence, the characteristic relaxation time is determined by the reciprocal of the peak frequency ω_{max}.

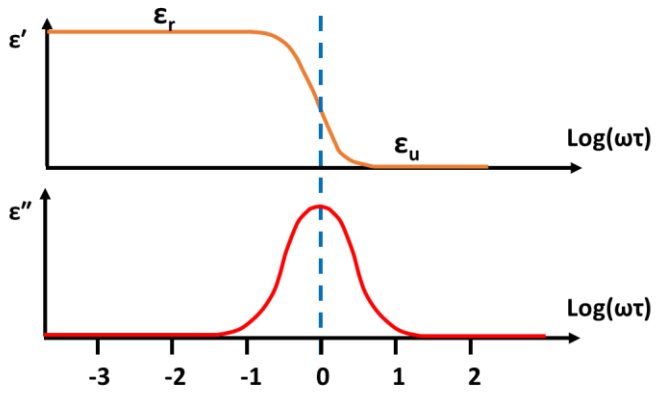

Figure 1.8 *Frequency dependence of ε′ and ε″ for a dielectric relaxation process.*

Dielectric spectroscopy was employed to probe molecular dynamics in bis-MPA based HBPs, and two sub-T_g relaxation processes were detected: γ- and β-relaxations, which were ascribed to the motions of hydroxyl and ester groups respectively. [40, 69-71] It was found that the bis-MPA based HBPs exhibit high activation for γ-relaxation, which was attributed to the strong inter-and intramolecular hydrogen bonding interaction.[40, 69-71] However, what role hydrogen bonding plays in defining mechanism of γ-relaxation was

not well explained. While γ-relaxation was reported by all studies conducted so far, it was debatable whether β-relaxation could be clearly resolved from the dielectric spectra of neat HBPs. Plus, it was also reported that another relaxation contributed by ionic motion, which was denoted as conductivity relaxation, was detected at a similar temperature range as β-relaxatoin.[69, 72] Hence, the nature of β-relaxation in bis-MPA based dendritic polymers need to be re-examined carefully. Similar studies should be extended to bis-MPA based dendrimers. It is also meaningful to compare how hydrogen bonding organization affects the dielectric properties in both HBPs and dendrimers.

1.6 Research overview

Despite a systematic study that has been performed on hydrogen bonding organization and hydrogen bonding mediated mesophase in bis-MPA based dendritic polymers, the experimental data of the corresponding dendrimers are still lacking. Hence, the related thermal, volumetric, and thermodynamic properties of dendrimers and how they differ from those of HBPs still remain unknown. Though the dielectric relaxations of bis-MPA based HBPs have been probed, a thorough understanding of the mechanism of the relaxations and their correlation with hydrogen bonding organization has yet to be developed. The purpose of this dissertation is to elucidate the correlation between the H-bond organization with the dielectric and volumetric properties of bis-MPA based dendritic polymers, with an emphasis on developing a fundamental understanding of to what extent structural irregularity affects the bulk properties of dendritic polymers. The following research objectives (R.O.) were utilized to accomplish the main goal.

R.O.1 Elucidate how structural irregularity and core molecule affect the formation of hydrogen bonding formation and hydrogen-bonded cluster formation.

R.O.2 Develop a fundamental understanding of the nature of dielectric relaxation processes in bis-MPA based HBPs and dendrimers.

R.O.3 Elucidate how dielectric properties and dielectric relaxation processes of bis-MPA based HBPs and dendrimers are correlated to the formation of hydrogen-bonded clusters in systems.

R.O.4 Develop a fundamental understanding of the correlation between the volumetric and thermodynamic properties and hydrogen bond organizations of bis-MPA based HBPs and dendrimers.

R.O.5 Model bis-MPA HBPs and dendrimers in the bulk to visualize the globular shape, hydrogen bond organization, and structural ordering.

R.O.6 Investigate the applicability of extending the study of the correlation between bulk properties and H-bond organization to hydroxylated linear polymer systems.

In Chapter II, the chemical composition of bis-MPA/PE dendrimer G2 and Boltorn^{TM} H20 was characterized via NMR, and H-bond formation was probe via FTIR. (R.O.1) The PVT behavior of both polymers was investigated, and volumetric and thermodynamic parameters were determined and compared. (R.O.4) In Chapter III, a dielectric analysis was conducted on both G2 and H20, their dielectric properties, as well as γ-relaxation, were investigated. (R.O.2 and 3). High dielectric constant values and associative behavior of γ-relaxation of G2 and H20 were ascribed to the formation of H-bonded clusters. Then G2, H20, and bis-MPA/PP50 dendrimer D20 were simulated via

MD simulation, and their molecular structure, bonding formation, and hydrogen-bonded cluster formation were analyzed. (R.O.1,2, and 3) The analysis of dielectric relaxation was continued in Chapter IV, where the other sub-T_g relaxation process of G2 and H20 discovered at higher temperatures was found to be correlated to ion translational motion. (R.O.2) The conductivity mechanism in both systems was found, and how it correlated to hydrogen bond origination was carefully studied. (R.O.3) In Chapter V, we extended the H-bond analysis study to a hydroxylated linear polymer system, in which the correlation between the H-bond formation and the gas barrier property was investigated. (R.O.6)

1.7 References

1. Bosman, A.; Janssen, H.; Meijer, E., About dendrimers: structure, physical properties, and applications. *Chem. Rev.* **1999,** *99* (7), 1665-1688.
2. Matthews, O. A.; Shipway, A. N.; Stoddart, J. F., Dendrimers—branching out from curiosities into new technologies. *Prog. Polym. Sci.* **1998,** *23* (1), 1-56.
3. Gao, C.; Yan, D., Hyperbranched polymers: from synthesis to applications. *Prog. Polym. Sci.* **2004,** *29* (3), 183-275.
4. Kim, Y. H., Hyperbranched polymers 10 years after. *J. Polym. Sci., Part A: Polym. Chem.* **1998,** *36* (11), 1685-1698.
5. Frechet, J. M., Functional polymers and dendrimers: reactivity, molecular architecture, and interfacial energy. *Science* **1994,** *263* (5154), 1710-1714.
6. Žagar, E.; Žigon, M., Aliphatic hyperbranched polyesters based on 2, 2-bis (methylol) propionic acid-Determination of structure, solution and bulk properties. *Prog. Polym. Sci.* **2011,** *36* (1), 53-88.
7. Carlmark, A.; Malmström, E.; Malkoch, M., Dendritic architectures based on bis-MPA: functional polymeric scaffolds for application-driven research. *Chem. Soc. Rev.* **2013,** *42* (13), 5858-5879.
8. Tomalia, D. A.; Fréchet, J. M. J., Discovery of dendrimers and dendritic polymers: A brief historical perspective. *J. Polym. Sci., Part A: Polym. Chem.* **2002,** *40* (16), 2719-2728.
9. Tomalia, D. A., Birth of a new macromolecular architecture: dendrimers as quantized building blocks for nanoscale synthetic polymer chemistry. *Prog. Polym. Sci.* **2005,** *30* (3), 294-324.

10. Voit, B. I., Dendritic polymers: from aesthetic macromolecules to commercially interesting materials. *Acta Polym.* **1995,** *46* (2), 87-99.
11. Tomalia, D. A.; Baker, H.; Dewald, J.; Hall, M.; Kallos, G.; Martin, S.; Roeck, J.; Ryder, J.; Smith, P., Dendritic macromolecules: synthesis of starburst dendrimers. *Macromolecules* **1986,** *19* (9), 2466-2468.
12. Vögtle, F.; Buhleier, E.; Wehner, W., Cascade and Nonskid-Chain-Like Syntheses of Molecular Cavity Topologies. *Synthesis* **1978,** *2*, 155-158.
13. Gunatillake, P. A.; Odian, G.; Tomalia, D. A., Thermal polymerization of a 2-(carboxyalkyl)-2-oxazoline. *Macromolecules* **1988,** *21* (6), 1556-1562.
14. Newkome, G. R.; Yao, Z.; Baker, G. R.; Gupta, V. K., Micelles. Part 1. Cascade molecules: a new approach to micelles. A [27]-arborol. *J. Org. Chem.* **1985,** *50* (11), 2003-2004.
15. Esfand, R.; Tomalia, D. A., Poly (amidoamine)(PAMAM) dendrimers: from biomimicry to drug delivery and biomedical applications. *Drug Discov. Today* **2001,** *6* (8), 427-436.
16. Svenson, S.; Tomalia, D. A., Dendrimers in biomedical applications—reflections on the field. *Adv. Drug Deliv. Rev.* **2005,** *57* (15), 2106-2129.
17. Hult, A.; Johansson, M.; Malmström, E., Dendritic resins for coating applications. In *Macromol Symp*, Basel: Hüthig & Wepf Verlag: 1995; Vol. 98, pp 1159-1161.
18. Hecht, S.; Fréchet, J. M., Dendritic encapsulation of function: applying nature's site isolation principle from biomimetics to materials science. *Angew. Chem. Int. Ed.* **2001,** *40* (1), 74-91.

19. Hawker, C.; Lee, R.; Fréchet, J., One-step synthesis of hyperbranched dendritic polyesters. *J. Am. Chem. Soc.* **1991,** *113* (12), 4583-4588.

20. Voit, B., New developments in hyperbranched polymers. *J. Polym. Sci., Part A: Polym. Chem.* **2000,** *38* (14), 2505-2525.

21. Kim, Y. H.; Webster, O. W., Hyperbranched polyphenylenes. *Macromolecules* **1992,** *25* (21), 5561-5572.

22. Zeng, X.; Zhang, Y.; Wu, Z.; Lundberg, P.; Malkoch, M.; Nyström, A. M., Hyperbranched copolymer micelles as delivery vehicles of doxorubicin in breast cancer cells. *J. Polym. Sci., Part A: Polym. Chem.* **2012,** *50* (2), 280-288.

23. Lee, C. C.; Gillies, E. R.; Fox, M. E.; Guillaudeu, S. J.; Fréchet, J. M.; Dy, E. E.; Szoka, F. C., A single dose of doxorubicin-functionalized bow-tie dendrimer cures mice bearing C-26 colon carcinomas. *Proc. Natl. Acad. Sci.* **2006,** *103* (45), 16649-16654.

24. Hölter, D.; Burgath, A.; Frey, H., Degree of branching in hyperbranched polymers. *Acta Polym.* **1997,** *48* (1-2), 30-35.

25. Malmström, E.; Johansson, M.; Hult, A., Hyperbranched aliphatic polyesters. *Macromolecules* **1995,** *28* (5), 1698-1703.

26. Magnusson, H.; Malmström, E.; Hult, A., Structure buildup in hyperbranched polymers from 2, 2-bis (hydroxymethyl) propionic acid. *Macromolecules* **2000,** *33* (8), 3099-3104.

27. Ihre, H.; Hult, A.; Fréchet, J. M.; Gitsov, I., Double-stage convergent approach for the synthesis of functionalized dendritic aliphatic polyesters based on 2, 2-bis (hydroxymethyl) propionic acid. *Macromolecules* **1998,** *31* (13), 4061-4068.

28. Ihre, H.; Padilla De Jesús, O. L.; Fréchet, J. M., Fast and convenient divergent synthesis of aliphatic ester dendrimers by anhydride coupling. *J. Am. Chem. Soc.* **2001,** *123* (25), 5908-5917.
29. Klee, J.; Schneider, C.; Hölter, D.; Burgath, A.; Frey, H.; Mülhaupt, R., Hyperbranched polyesters and their application in dental composites: monomers for low shrinking composites. *Polym. Adv. Technol.* **2001,** *12* (6), 346-354.
30. Zeng, X.; Zhang, Y.; Nyström, A. M., Endocytic uptake and intracellular trafficking of bis-MPA-based hyperbranched copolymer micelles in breast cancer cells. *Biomacromolecules* **2012,** *13* (11), 3814-3822.
31. Johansson, M.; Malmström, E.; Jansson, A.; Hult, A., Novel concept for low temperature curing powder coatings based on hyperbranched polyesters. *J. Coat. Technol.* **2000,** *72* (906), 49-54.
32. Boltorn product information. https://www.perstorp.com/~/media/files/perstorp/pb/boltorn.ashx.(assessed December 20, 2019)
33. Malmström, E.; Hult, A., Kinetics of formation of hyperbranched polyesters based on 2, 2-bis (methylol) propionic acid. *Macromolecules* **1996,** *29* (4), 1222-1228.
34. Pettersson, B., Hyperbranched polymers: unique design tools for multi-property control in resins and coatings. *Pigm. Resin. Technol.* **1996,** *25* (4), 4-14.
35. Jena, K. K.; Raju, K. S. N., Synthesis and characterization of hyperbranched polyurethane hybrids using tetraethoxysilane (TEOS) as cross-linker. *Ind. Eng. Chem. Res.* **2008,** *47* (23), 9214-9224.

36. Ikladious, N. E.; Mansour, S. H.; Rozik, N. N.; Dirnberger, K.; Eisenbach, C. D., New aliphatic hyperbranched polyester polyols based on 1, 3, 5-tris (2-hydroxyethyl) cyanuric acid as a core. *J. Polym. Sci., Part A: Polym. Chem.* **2008,** *46* (16), 5568-5579.

37. Walter, M. V.; Malkoch, M., Simplifying the synthesis of dendrimers: accelerated approaches. *Chem. Soc. Rev.* **2012,** *41* (13), 4593-4609.

38. Malmström, E.; Johansson, M.; Hult, A., The effect of terminal alkyl chains on hyperbranched polyesters based on 2, 2-bis (hydroxymethyl) propionic acid. *Macromol. Chem. Phys.* **1996,** *197* (10), 3199-3207.

39. Zagar, E.; Huskic, M.; Grdadolnik, J.; Zigon, M.; Zupancic-Valant, A., Effect of annealing on the rheological and thermal properties of aliphatic hyperbranched polyester based on 2, 2-bis (methylol) propionic acid. *Macromolecules* **2005,** *38* (9), 3933-3942.

40. Malmström, E.; Liu, F.; Boyd, R.; Hult, A.; Gedde, U., Relaxation processes in hyperbranched polyesters. *Polym. Bull.* **1994,** *32* (5-6), 679-685.

41. Tanis, I.; Karatasos, K., Local dynamics and hydrogen bonding in hyperbranched aliphatic polyesters. *Macromolecules* **2009,** *42* (24), 9581-9591.

42. Žagar, E.; Huskić, M.; Žigon, M., Structure-to-Properties Relationship of Aliphatic Hyperbranched Polyesters. *Macromol. Chem. Phys.* **2007,** *208* (13), 1379-1387.

43. Žagar, E.; Grdadolnik, J., An infrared spectroscopic study of H-bond network in hyperbranched polyester polyol. *J. Mol. Struct.* **2003,** *658* (3), 143-152.

44. Syed, M. N. Hydrogen Bond-Mediated Structural Order in Hydroxylated Bis-MPA Dendritic Polymers: Experimental and Molecular Dynamics Simulation Study. Ph.D. Thesis, The University of Southern Mississippi, 2015.
45. Jedlovszky, P.; Brodholt, J.; Bruni, F.; Ricci, M.; Soper, A.; Vallauri, R., Analysis of the hydrogen-bonded structure of water from ambient to supercritical conditions. *J. Chem. Phys.* **1998,** *108* (20), 8528-8540.
46. Head-Gordon, T.; Hura, G., Water structure from scattering experiments and simulation. *Chem. Rev.* **2002,** *102* (8), 2651-2670.
47. Ball, P., Water—an enduring mystery. *Nature* **2008,** *452* (7185), 291-292.
48. Röthlisberger, U.; Parrinello, M., Ab initio molecular dynamics simulation of liquid hydrogen fluoride. *J. Chem. Phys.* **1997,** *106* (11), 4658-4664.
49. McLain, S. E.; Benmore, C. J.; Siewenie, J. E.; Urquidi, J.; Turner, J. F., On the structure of liquid hydrogen fluoride. *Angew. Chem. Int. Ed.* **2004,** *43* (15), 1952-1955.
50. Rogunova, M.; Lynch, T.; Pretzer, W.; Kulzick, M.; Hiltner, A.; Baer, E., Solid-state structure and properties of hyperbranched polyols. *J. Appl. Polym. Sci.* **2000,** *77* (6), 1207-1217.
51. Alexander, L. E., Introduction to Diffraction By Polymers. In *X-ray diffraction methods in polymer science*, Krieger: Huntington, NY., 1969; pp 43-47.
52. Jonscher, A. K., Dielectric relaxation in solids. *J. Phys. D: Appl. Phys.* **1999,** *32* (14), R57.
53. Griffiths, D. J., Electric Fields in Matter. In *Introduction to electrodynamics (4th Edition)*, Pearson Education, Inc: Glenview, IL, 2012; pp 167-209.

54. Feynman, R. P.; Leighton, R. B.; Sands, M., The feynman lectures on physics; vol. i. *Am. J. Phys.* **1965,** *33* (9), 750-752.

55. Haynes, W. M.; Wohlfarth, C., Permittivity (Dielectric constant) of Liquids. In *CRC Handbook of Chemistry and Physics*, CRC Press: 2014; pp 6-153-6-175.

56. Bao, J. Z.; Swicord, M. L.; Davis, C. C., Microwave dielectric characterization of binary mixtures of water, methanol, and ethanol. *J. Chem. Phys.* **1996,** *104* (12), 4441-4450.

57. National Physical Laboratory Dielectric properties of materials. http://www.kayelaby.npl.co.uk/general_physics/2_6/2_6_5.html (accessed December 17, 2018).

58. Wu, M.; Alivov, Y.; Morkoç, H., High-κ dielectrics and advanced channel concepts for Si MOSFET. *J. Mater. Sci.: Mater. Electron.* **2008,** *19* (10), 915-951.

59. Haynes, W. M., Dielectric Constant of Selected Polymers. In *CRC Handbook of Chemistry and Physics*, CRC Press: 2014; pp 13-15.

60. Chemical Retrieval on the Web DIELECTRIC STRENGTH OF POLYMERS. https://polymerdatabase.com/polymer%20physics/Dielectric%20Strength.html (accessed December 17, 2018).

61. Kurosaki, S.; Furumaya, T., Hydrogen bond chains and dielectric relaxation of polyvinyl alcohol. *J. Polym. Sci.* **1960,** *43* (141), 137-148.

62. Sack, R., The dielectric properties of systems containing straight polar chains. *Aust. J. Chem.* **1952,** *5* (1), 135-145.

63. Sengwa, R. J.; Kaur, K.; Chaudhary, R., Dielectric properties of low molecular weight poly(ethylene glycol)s. *Polym Int* **2000,** *49* (6), 599-608.

64. Sinha, S.; Chatterjee, S. K.; Ghosh, J.; Meikap, A. K., Dielectric relaxation and ac conductivity behaviour of polyvinyl alcohol–HgSe quantum dot hybrid films. *J. Phys. D: Appl. Phys.* **2014,** *47* (27), 275301.

65. Dai, Z.-H.; Li, T.; Gao, Y.; Xu, J.; Weng, Y.; He, J.; Guo, B.-H., Improved dielectric and energy storage properties of poly (vinyl alcohol) nanocomposites by strengthening interfacial hydrogen-bonding interaction. *Colloids Surf. A* **2018,** *548*, 179-190.

66. Sharp, K. A., Water: structure and properties. *Encyclopedia of life sciences* **2001,** *10*.

67. Stillinger, F. H., Low-Frequency Dielectric Properties of Liquid and Solid Water. *The Liquid State of Matter: Fluids, Simple and Complex* **1982**, 341-431.

68. Vassilikou-Dova, A.; Kalogeras, I. M., Dielectric Analysis (DEA). In *Thermal Analysis of Polymers*, Menczel, J. D.; Prime, R. B., Eds. 2008; pp 497-613.

69. Zhu, P. W.; Zheng, S.; Simon, G., Dielectric relaxations in a hyperbranched polyester with terminal hydroxyl groups: effects of generation number. *Macromol. Chem. Phys.* **2001,** *202* (15), 3008-3017.

70. Turky, G.; Shaaban, S. S.; Schoenhals, A., Broadband Dielectric Spectroscopy On the Molecular Dynamics in Different Generations of Hyperbranched Polyester. *J. Appl. Polym. Sci.* **2009,** *113* (4), 2477-2484.

71. Androulaki, K.; Chrissopoulou, K.; Prevosto, D.; Labardi, M.; Anastasiadis, S. H., Dynamics of hyperbranched polymers under confinement: a dielectric relaxation study. *ACS Appl. Mater. Inter.* **2015,** *7* (23), 12387-12398.

72. Adrjanowicz, K.; Kaminski, K.; Dulski, M.; Jasiurkowska-Delaporte, M.; Kolodziejczyk, K.; Jarek, M.; Bartkowiak, G.; Hawelek, L.; Jurga, S.; Paluch, M.,

Dynamic Glass Transition and Electrical Conductivity Behavior Dominated by Proton Hopping Mechanism Studied in the Family of Hyperbranched Bis-MPA Polyesters. *Macromolecules* **2014,** *47* (16), 5798-5807.

CHAPTER II - BULK VOLUMETRIC AND THERMODYNAMIC PROPERTIES OF BIS-MPA BASED DENDRIMERS AND HYPERBRANCHED POLYMERS

Abstract

The chemical nature, the formation of hydrogen bonding, and the thermal transition of the dendrimer G2 and Boltorn^{TM} H20 was carefully analyzed and compared. Despite their similar hydroxyl concentration, the fraction of OH···OH H-bonds was found to be higher in G2. The volumetric properties of G2 and H20 were probed by using PVT dilatometry. The thermal expansion coefficient and the compressibility of G2 and H20 were also analyzed. It was found that the formation of a mesophase affects the thermal expansion behavior of H20 at higher temperatures. The Simha-Somcynsky equation of state (SS-EOS) was found to be able to describe the PVT surface of G2 and H20 with accuracy. Thermodynamic parameters, including the scaling parameters (P*, V*, T*), the molecular mass of the statistical segments (M_s), molar activation energy (ϵ^*), and molar volume (v*) were extracted from SS-EOS. It was found that the flexibility of the H20 molecule is higher and the hydrogen bonding interaction in G2 is greater. The specific free volume (V_f), occupied volume (V_{occ}), and fractional free volume (h) were also determined via fitting PVT data to the SS-EOS and their temperature dependency was analyzed. Higher free volume was found in H20 which contributes to its higher specific volume. The temperature and pressure dependence of G2 and H20 displayed good agreement with their thermal expansion coefficient and compressibility.

2.1 Introduction

Due to the availability of the bis-MPA based dendrimers, few studies have been conducted to probe their bulk properties. Though the study conducted by Zagar. etc has shown some differences between bis-MPA based HBPs and dendrimers on the thermal transitions and the structural ordering, a more systematic work of comparing their chemical nature, hydrogen bonding formation, and other bulk properties are still lacking.[1] The hydrogen bonding formation in bis-MPA based HBPs and dendrimer systems has been studied by us via MD simulation, where the dendrimers were found to have a higher fraction of OH ··OH H-bonds as compared to the corresponding HBPs. [2] Hence, an experimental study is needed to confirm it. Fourier-transform infrared spectroscopy (FTIR) is a useful tool to probe the hydrogen bonding as the vibration peaks for proton donors and acceptors would be red-shifted and intensified by the formation of H-bonds. [3-5] [6] The FTIR studies of bis-MPA based HBPs were reported, where a higher fraction of OH ··OH H-bonds was found in H20 as compared to H40. [7, 8]

The volumetric properties, including specific volume, thermal expansion coefficient, compressibility, and free volume are very critical to polymers as they provide information on molecular packing, thermal transition, relaxation behaviors, intermolecular interactions, and so on. Despite their importance, however, the studies of the volumetric properties of dendritic polymers were only limited to the poly (benzyl ether) dendrimer (PBED) systems [9, 10] In our previous study, we were able to simulate the volume-temperature curves of bis-MPA based HBPs and dendrimers which display good agreement with the experimental ones of HBPs. Still, an experimental study is needed for bis-MPA based dendrimers.

The volumetric properties of polymers can be measured by PVT dilatometry, which collects the specific volume data isothermally or isobarically via a linear variable differential transducer (LVDT). To extract free volume and other thermodynamic parameters, it is needed to apply the PVT data to an equation of state. Among various equations of stats that are derived for polymers, the Simha-Somcynsky equation of state, which was proved to have low deviations from experimental data within a wide temperature and pressure range, is adopted for this study.[11, 12] The SS-EOS was developed based on the lattice-hole theory, where a linear polymer was divided into s equivalent segments with each of them occupying one lattice site in the system. Each equivalent segment is termed as a s-mer of which the molar mass does not necessarily equal that of the repeat unit of the polymer chain. While the occupied sites account for the occupied volume, the unoccupied ones represent the free volume. The size of each lattice cell is defined by the separation distance at the minimum of the Lennard-Jones (L-J) potential. The differentiation of the Helmholtz free at thermodynamic equilibrium yield the SS-EOS in the form of coupled equations:[13]

$$(\tilde{P}\tilde{V})/\tilde{T} = \left[1 - y\left(2^{\frac{1}{2}}y\tilde{V}\right)^{-\frac{1}{3}}\right]^{-1} + y/\tilde{T}\left[2.002\left(y\tilde{V}\right)^{-4} - 2.409\left(y\tilde{V}\right)^{-2}\right] \quad (7)$$

$$3c\left[\left(2^{-\frac{1}{6}}\mathrm{y}\left(1/y\tilde{V}\right)^{\frac{1}{3}}-1/3\right)\Big/\left(1-2^{-\frac{1}{6}}\mathrm{y}\left(1/y\tilde{V}\right)^{\frac{1}{3}}\right)\right.$$

$$\left.-y\left(1/y\tilde{V}\right)^{2}\left(3.033\left(1/y\tilde{V}\right)^{2}-2.409\right)/6\tilde{T}\right]+(1-s) \qquad (8)$$

$$-s\ln(1-y)/y=0$$

where y=1-h is the fraction of occupied volume. The reduced variables are defined as $\tilde{P}=P/P^{*}$, $\tilde{V}=V/V^{*}$, and $\tilde{T}=T/T^{*}$, where P*, V*, and T* are the characteristic scaling parameters which depend on the specific molecules. The 3 scaling parameters are defined as

$$\left.\begin{array}{c}P^{*}=zq\epsilon^{*}/(sv^{*})\\T^{*}=zq\epsilon^{*}/(Rc)\\V^{*}=v^{*}/M_{s}\end{array}\right\}(P^{*}V^{*}T^{*})/M_{s}=Rc/s\Rightarrow R/3$$

where ϵ* is the maximum attraction energy of the 6-12 Lennard-Jones (L-J) interaction and v* is the corresponding molar volume at the minimum potential. R is the gas constant. $M_s = M_n/s$ is the molar segmental mass, where Mn is the average molecular weight of the macromolecules. 3c is the external volume-dependent degrees of freedom per chain. $qz = s(z-2)+2$ is the number of interchain contacts, where $z = 12$, is the coordination number. For macromolecule chains, s→∞ can be assumed that 3c/s→ 1.

Though it has been proven that the SS-EOS is able to fit many linear polymer systems with good accuracy, it is still questionable for its applicability to the dendritic polymer system as the model was developed based on linear polymers. [12, 14, 15] To date, there's only one study that exams the limits of the applicability of SS-EOS by comparing the thermodynamic properties between linear polystyrene (PS) and PBED.[9] It was

reported that the SS-EOS was able to describe the PVT surface, the compressibility, and the thermal expansion coefficient precisely.[9] However, similar research has not been extended to hydroxylated dendrimer systems in which hydrogen bonding interaction plays an important role in defining bulk properties.

In this study, the chemical and physical properties of a second-generation bis-MPA based dendrimer, G2, and its corresponding hyperbranched polymer (HBP), Boltorn™ H20, was probed and compared. The chemical composition and the formation of hydrogen bonds in both systems were well characterized. Thermal transitions, volumetric and thermodynamic properties, and their correlation with hydrogen bonding formation of the two systems were investigated. The applicability of the SS-EOS theory to the hydroxylated dendrimer system was also evaluated.

2.2 Experimental Section

2.2.1 Materials and sample preparation

The perfectly branched second-generation dendrimer, designated hereafter as G2, was kindly provided by Dr. Scott Grayson, Tulane University, New Orleans, LA. It was synthesized from bis-MPA branching monomer and pentaerythritol core using a diverging approach via anhydride coupling as described elsewhere.[16, 17] The theoretical molecular weight of G2 based on its structure was calculated as 1529.5 g/mol. Nearly the same weight, 1528.8 g/mol, was determined by Matrix-Assisted Laser Desorption/Ionization Time-of-Flight Mass Spectrometry (MALDI-ToF MS), thus confirming the unimolecular distribution of G2. (Appendix Figure A.1)

The second-generation HBP, Boltorn^{TM} H20, the schematics of which is shown in Figure 2.1, was kindly donated by Perstorp Polyols Inc. This commercially available dendritic polymer was synthesized via the one-pot method using ethoxylated pentaerythritol (PP50) core and 2,2-bis(methylol)propionic acid (bis-MPA) branching monomer.

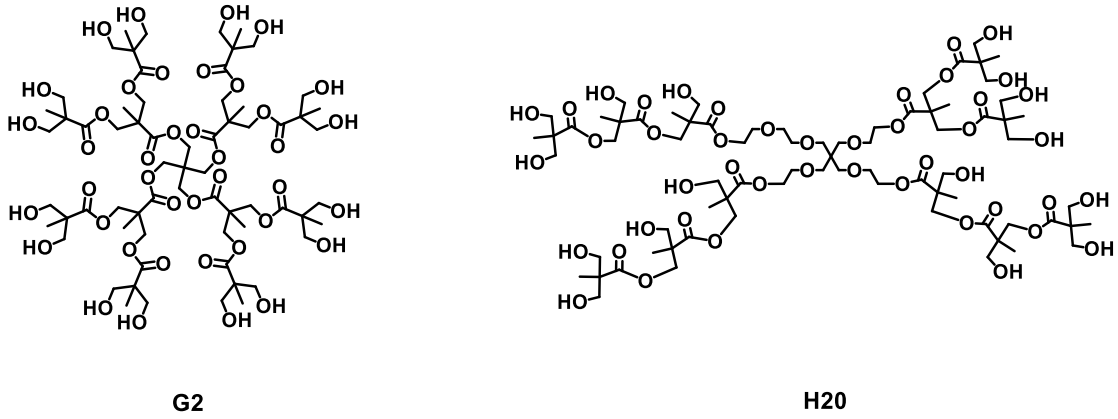

Figure 2.1 *Chemical structures of G2 and Boltorn^{TM} H20.*

Boltorn hyperbranched polyesters of this class are typically designated in the literature as HX0, where X denotes the pseudo-generation number. The theoretical (based on composition) molecular weight of H20 is 1749 g/mol. As reported by Perstorp the number average molecular weight of H20 however is somewhat greater, i.e. 2100 g/mol. The degree of branching (DB) of H20 determined by NMR has been reported as 0.261 using the definition given by Frey. [7, 18]

A Carver Melt Press (Model M) was used to prepare thin sheets of H20 and G2. Pellets of H20 and powder for G2 were dried under vacuum for at least 24 hours at 80°C prior to compression molding. The appropriate amount of each polymer was placed in a

mold of 0.34 mm thickness, which was sandwiched between two Teflon sheets, with two metal plates on each side. The platens were placed in the press at 140°C and held for about 10 min without pressure. The pressure was first increased to 2,500 psi followed by a release of pressure to remove air bubbles, then increased to 7,500 psi at which polymers were finally molded. The mold was cooled at a rate of about 10°C per minute by flowing water through the press plates. The molded samples were then removed and placed in a desiccant chamber until further testing.

2.2.2 Experimental methods

The ^{1}H NMR spectra were collected using a Varian VXR 300 NMR spectrometer. Each sample was prepared by dissolving the polymer in DMSO-*d*6 at the concentration of 1% (wt/wt). Before the measurements, the samples were heated to 140°C for 1 hr and then quenched in liquid nitrogen to dissociate the hydrogen bonds in the systems.

The infrared spectra were collected using a Perkin-Elmer 1600 FTIR spectrometer. Thin films on the NaCl plates were prepared by solution casting using acetone. After solvent evaporation, the films were dried in vacuum for 12 hr to remove any traces of acetone and water.

Thermal behavior was investigated by differential scanning calorimetry (DSC) using a TA Instruments DSC Q-100. The calibration was carried out using indium and sapphire standards. Samples were first heated to 200°C at a rate of 10°C/min to erase thermal history, quenched to -90°C at 5°C/min, and then heated to 200°C at 10°C/min. The second heating scans were reported.

The Archimedes' principle was used to measure density. The measurements were conducted using a Mettler Toledo Balance (Model XS-104) equipped with a density kit. Small, 2×2mm film samples were cut and weighed before and after immersed in toluene. The density was calculated as follows.

$$\rho_P = \frac{W_A}{W_A - W_T} \cdot \rho_0 \tag{9}$$

where W_A and W_T are the sample weight measured in air and toluene, and ρ_0 is the density of the toluene, which is 0.870 g/cc. The final density was taken as the average of five measurements. The standard error of the density measurements did not exceed 0.002 g/cm^3.

The volumetric properties of G2 and H20 in the bulk were studied using the pressure-volume-temperature (PVT) techniques. The PVT measurements were conducted by utilizing a fully automated Gnomix-PVT-apparatus (Boulder, Col. USA) with mercury employed as a confining fluid. Specific volumes, with accuracy ±0.002 cm3/g, were recorded from 30°C to 120°C above the T_g of each sample. All reported here PVT data were collected in isothermal mode. At each temperature interval, the pressure was increased with an increment of 10 MPa steps from 10 to 150 MPa. The specific volume at 1atm was extrapolated by fitting the PVT data collected at elevated pressures to Tait equation of state.[19]

$$\frac{v(P,T)}{v(0,T)} = 1 - Cln(1 + \frac{P}{b(T)}) \tag{10}$$

where $b(T) = b_1 \exp(-b_2 T)$, v(P, T) is the molar volume as a function of pressure, P, at a given temperature, T. v(0, T) is the molar volume at zero (atmospheric) pressure at the same given temperature. C, b_1, and b_2 are fitting parameters for this equation, which were

determined by fitting the volume data along an isotherm with different pressures. This routine is directly built into Gnomix-PVT-apparatus software.

The PVT data were fitting to Simha-Somcynsky equation of state (SS-EOS) via using a home-made software named 'ssfit,' where the fitting parameters P*, V*, T* were determined by minimization of the χ^2 which was defined by

$$\chi^2 = \sum_{i=1}^{N} \frac{(M_i - F_i)^2}{v_i}$$

where M and F are the measured and the fit specific volumes respectively, and v is the square of the standard deviation of the measured specific volumes. Instead of the exact equation, the approximate solutions to the SS-EOS were determined by an analytical equation representation derived by Utracki and Simha:[20]

$$ln\tilde{V} = a_0 + a_1\tilde{T}^{3/2} + \tilde{P}[a_2 + (a_3 + a_4\tilde{P} + a_5\tilde{P}^2)\tilde{T}^2] \quad (11)$$

where the values of the constants are listed in the table below.

Table 2.1 . *Fitting coefficients for the analytical representation of the SS-EOS*

Coefficients	Value
a_0	-0.10346
a_1	23.854
a_2	-0.1320
a_3	-333.7
a_4	1032.5
a_5	-1329.9

2.3 Results and Discussion

2.3.1 NMR

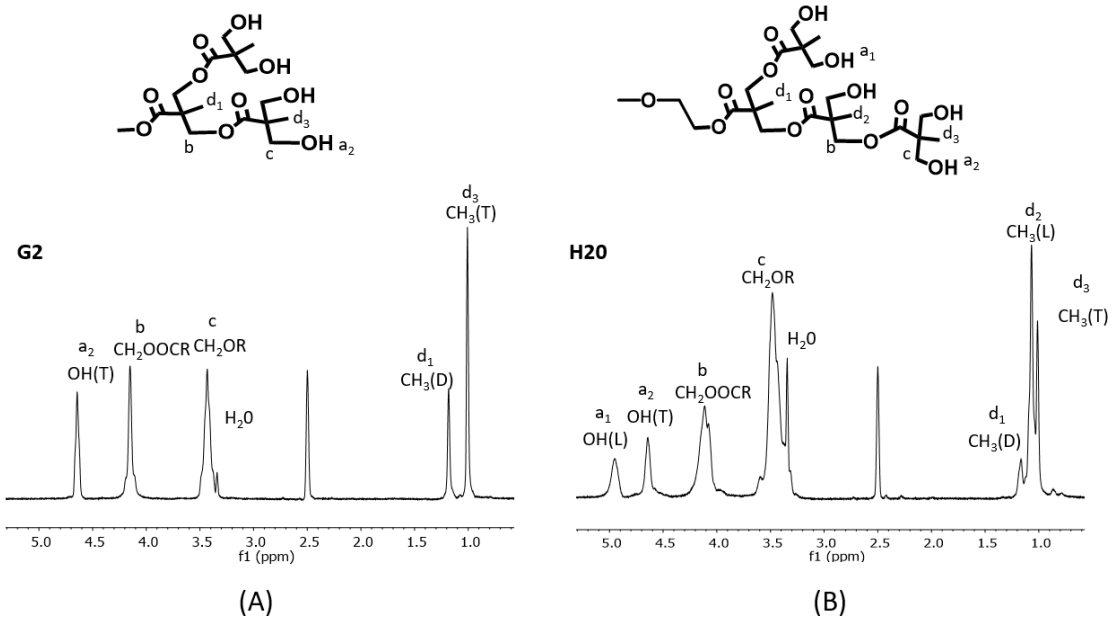

Figure 2.2 *^{1}H NMR spectra of (A)G2, (B) H20*

NMR specifically was used to probe the chemical structure and architecture of the studied molecules in this system. Figure 2.2 shows the characteristic ^{1}H NMR spectra obtained for (A) G2 and (B) H20 systems with the corresponding peak assignments. The most obvious difference between NMR patterns for G2 and H20 systems is the presence in the former of only terminal hydroxyl groups, while the H20 spectrum shows both terminal and linear hydroxyl units. The integrated values of each peak are listed in Table 2.2 and used to calculate and compare several important structural parameters, i.e. the degree of branching by Frey, hydroxyl/carbonyl ratio, the number of hydroxyl groups per molecule, the concentration of hydroxyl groups, and the number average molecular weight for each

polymer. These parameters are also displayed in Table 2.2**.** The degree of branching (DB) by Frey was calculated from

$$DB = \frac{2 * I(CH_3)_D}{2 * I(CH_3)_D + I(CH_3)_L} \quad (12)$$

Naturally, G2 showed the degree of branching 1.00 while the degree of branching for H20 was considerably lower, i.e. 0.258 (0.261 was reported by Perstorp). The hydroxyl/carbonyl ratio was calculated directly from the corresponding peak areas as follows,

$$\frac{[OH]}{[CO]} = \frac{I(OH)}{2 * I(CH_2OOCR)} \quad (13)$$

The average number of OH groups per molecule (n(OH)) and the number average molecular weight ($\overline{M_n}$) of H20 were determined according to the methodology proposed by Žagar et. Al, where a large fraction of HBPs without the core (B_2) was firstly discovered as a result of incomplete conversion. Hence, the equivalent number of B_2, N(B_2), was determined by the number of unreacted carboxylic acid groups, [21]

$$N(B_2) = I(COOH)_{unreacted} = I(OH) - I(OH)_{theor.} \quad (14)$$

where $I(OH)_{theor.} = 4 * N(PP50) + 2 * N(bis-MPA) - N(bis-MPA)$ (15)

where N(PP50) and N(bis-MPA) were determined by as follows:

$$N(PP50) = \frac{I(CH_2)_{PP50}}{14 * 2} = \frac{1}{28} * [I(CH_2OR) + I(CH_2OOCR) - \frac{4}{3} * I(CH_3)] \quad (16)$$

$$N(bis-MPA) = \frac{ICH_3}{3} \quad (17)$$

Then n(OH) and $\overline{M_n}$, were determined by:

$$n(OH) = \frac{I(OH)}{N(PP50) + N(B2)} \quad (18)$$

$$\overline{M_n} = (DP - 1)(M_{bis-MPA} - M_{H_2O} + x_{PP50}M_{PP50} + x_{B_2}M_{bis-MPA}) \quad (19)$$

where $DP = \frac{N(PP50)+N(bis-MPA)}{N(PP50)+N(B2)}$, $x_{PP50} = \frac{N(PP50)}{N(B_2)+N(PP50)}$, and $x_{B_2} = 1 - x_{PP50}$.

Finally, the OH concentration per gram of the sample ([OH]) was calculated by:

$$[OH] = \frac{n(OH)}{\overline{M_n}} \times 1000 \quad (20)$$

The calculated here values of n(OH) and $\overline{M_n}$ for H20 polymer were in good agreement with those reported for H20 by Zagar et al., i.e., 8.9 and 930 g/mol respectively, but considerably smaller than those theoretically predicted, assuming that the conversion of the polymerization is 100%, i.e., 16 and 1749 g/mol.[21] The [OH] value was also consistent with the OH-value reported by the Perstorp company, which is 490~520 KOH/g. Therefore, we also confirm here that about 50% of the reaction products for H20 indeed resulted from incomplete conversion, which was determined as 90%.[21, 22] On the other hand, as expected from MALDI-TOF data, G2 system exhibited N(OH) and $\overline{M_n}$ values which are in excellent agreement with the theoretically predicted numbers, i.e.16 and 1529.5 g/mol respectively. It should be noted that despite the determined N(OH) quantities for G2 and H20 were considerably different, the OH group concentration as well as OH/CO group ratio values were comparable.

Table 2.2 *Integrals of the ^{1}H NMR signals of individual protons for G2, H20*

Assignment	**G2**	**H20**
$I(CH_3)_D$	12	3.86
$I(CH_3)_L$	-	22.16
$I(CH_3)_T$	24.7	10.14
$I(CH_2OR)$	32.67	47.69
$I(CH_2OOCR)$	24.35	24.13
$I(OH)_T$	16.11	9.56
$I(OH)_L$	-	7.02
Calculated values		
DB	1.00	0.258
[OH]/[CO]	1.32	1.37
n(OH)	16.15	8.25
$\overline{M_n}$ (g/mol)	1563	859
[OH] (mmol/g)	10.31	9.60
$[CH_3]$ (mmol/g)	7.85	6.99

2.3.2 FTIR

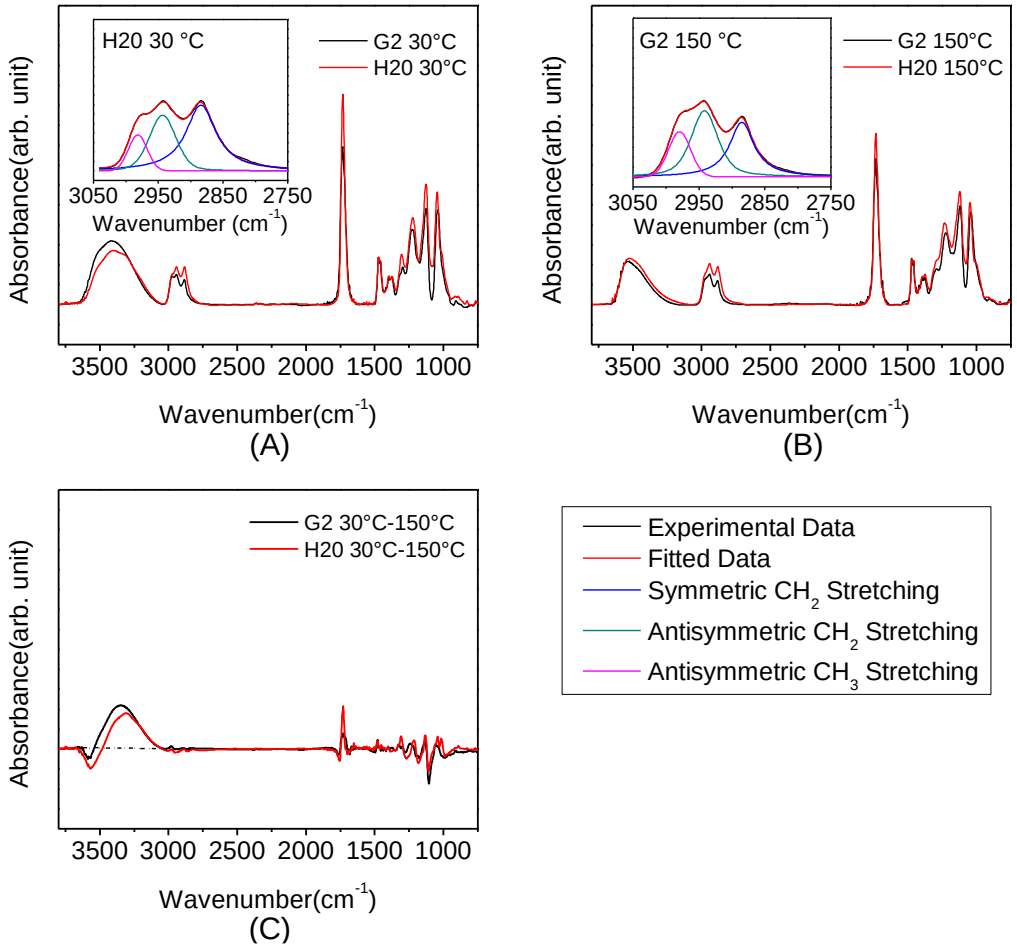

Figure 2.3 *FTIR spectra of G2 and H20. (A)30 °C, (B) 150 °C, (C) difference spectra obtained by subtraction of the spectra (B) from the spectra (A). The insets in (A) and (B) are the peak deconvolution of the methyl and methylene stretching peak of H20 at 20 °C and G2 at 150°C, respectively.*

FTIR was mainly used to probe the extent of hydrogen bonding of the involved hydroxyl and carbonyl groups. The FTIR spectra for H20 and G2 systems recorded at 30 °C and 150 °C are presented in Figure 2.3 (A) and (B). These spectra were normalized using the antisymmetric vibration peak of the methyl groups centered at 2978 cm^{-1}. The

intensity of this methyl stretching peak was determined via peak deconvolution shown as the insets in Figure 2.3 (A) and (B). The rationale of using this methyl peak for normalization was determined by the fact that the concentration of these groups was similar for G2 and H20, and they also do not participate in hydrogen bonding, so the position, shape, and intensity of this peak were not affected. At 30 °C, both G2 and H20 polymers displayed rather intense and very broad asymmetrically shaped IR band centered at about 3400 cm^{-1} which was assigned to the stretch vibration of the combination of free but mainly hydrogen-bonded hydroxyl groups (vOH).[8, 23] The reported frequency range of the free hydroxyl stretch vibration is 3644-3635 cm^{-1}, so there was a considerable red-shift, which reflects the reduced force constant of the O-H oscillator and enhanced anharmonicity of the vibrational potential with hydrogen bonding. [3-5] A broadening was attributed to the presence of a wide range of O-H···O hydrogen bond associations, which exhibit a broad distribution of bond angles and bond lengths. Besides, the hydroxyl groups can participate in hydrogen bonding as donors and acceptors in contrast to the carbonyl groups, which can serve as acceptors only. A well-documented signature of O-H···O bonding is also the increase of IR adsorption intensity as compared to free hydroxyl stretching adsorption. This is due to an increased overall dipole moment of O-H···O associations as compared when the corresponding moieties are unbonded.[6]

The sharp absorption peak centered at 1732cm^{-1} was assigned to the stretching vibration of the carbonyl groups (vCO). The reported frequency range of the free carbonyl stretching vibration is 1750-1735 cm^{-1}.[24] Similar to vOH, vCO can be affected by hydrogen bonding but the effect is smaller than in the case of vOH. [8, 25] At 30 °C, one

can see that the intensity of vOH peak for G2 is greater than that for H20. Interestingly, the differences in the intensity of the vCO peak are the opposite. The peak area ratio, AvOH/AvCO, was calculated for both G2 and H20 systems at 30°C to be 2.8 and 2.3, respectively, and used to compare with the corresponding hydroxyl to carbonyl group ratios determined by NMR, i.e. 1.3 (G2) and 1.4 (H20). The observed strong disagreement clearly indicates that in the case of hydrogen bonding the FTIR based hydroxyl/carbonyl peak ratio does not directly reflect the ratio of the concentrations of these moieties and therefore cannot be used for quantitative purposes. Somewhat greater AvOH/AvCO observed for G2 versus H20 implies that in the former system OH···OH was perhaps a predominant type of H-bond associations with a lesser number of carbonyl groups involved than in the case of H20. As expected, upon heating to 150°C, vOH and vCO peaks as a whole shifted to higher frequencies, i.e. 3535 and 1734 cm^{-1} (blue-shift), and the corresponding peak intensities were drastically reduced indicative of the transition from the state with mainly hydrogen-bonded hydroxyl and carbonyl groups to the state when they are predominantly free.[5, 6, 8, 25, 26] The blue-shift of vOH and vCO peaks at higher temperature and the transition from predominantly hydrogen-bonded to free hydroxyls is particularly apparent when looking at FTIR difference spectra displayed in Figure 2.3 (C) which clearly indicate for both G2 and H20 systems the presence of negative (at higher frequencies) and positive (at lower frequencies) differences in the corresponding hydroxyl and carbonyl stretching IR ranges. Furthermore, at 150 °C, the shape and intensity of vOH and vCO peaks for G2 became comparable with those for H20. The AvOH/AvCO ratio was also calculated for G2 and H20 at 150°C to be 1.3 and 1.5 respectively, showing now an excellent agreement with the NMR data.

2.3.3 DSC

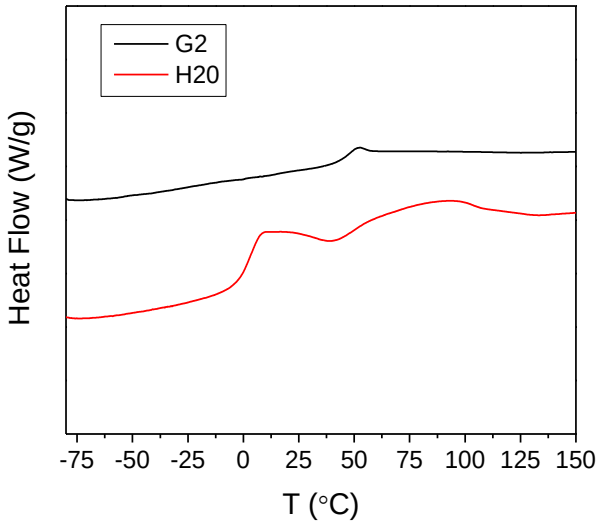

Figure 2.4 *DSC thermograms of H20 and G2*

Figure 2.4 shows the DSC curves of H20 and G2. Glass transition temperature, T_g, of both polymers was determined as 4 °C and 49 °C respectively. The lower T_g of H20 can be attributed to its low molecular weight, which is revealed by the NMR data, and the broad M_w dispersion resulting from the nature of the one-pot synthesis method.[22, 27] Besides, hydrogen bonding formation may also play a role in defining the T_g of both polymers. It was reported that T_g of hydroxylated HPBs drops significantly when hydroxyl chain ends are replaced by alkyl, benzoate, acetate groups.[28, 29] A huge reduction on T_g was also observed when H20 was esterified with acetyl chloride, which will be discussed in the following chapters.

Above T_g, G2 showed no transitions, whereas H20 displayed an exothermic peak followed by a broad endothermic peak. The exo- and endothermic peaks are ascribed to the

formation and cleavage of H-bonds respectively, which are correlated to the formation and melting of a mesophase formed by linear segments in HBPs. [1,2] Since G2 contains no linear segments, these peaks were absent on its DSC curve.

2.3.4 PVT

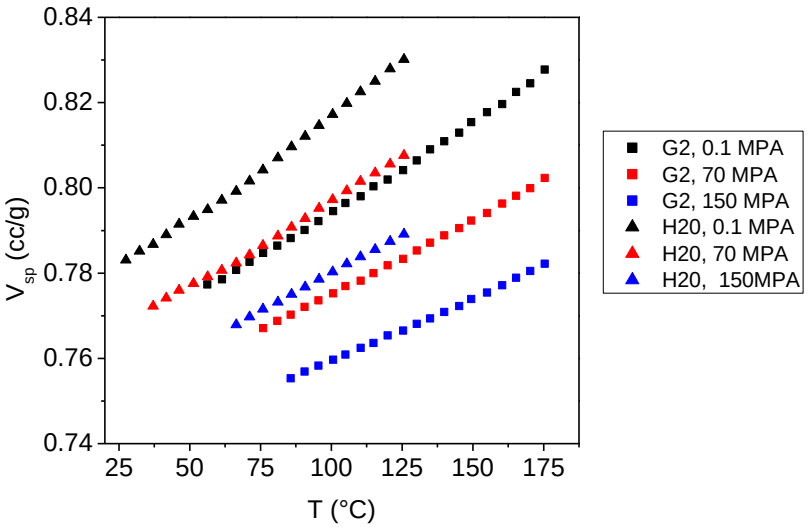

Figure 2.5 *Volume-temperature curves at the melt state for G2 and H20 at 0.1MPa, 70MPa, and 150MPa.*

The volume-temperature (V-T) curves at the melt state for both G2 and H20 at 0.1MPa, 70MPa, and 150MPa was presented in Figure 2.5. The specific volumes of both polymers increase monotonically with temperature, which indicates that there's no first-order transition above T_g. However, a very small hump was observed on the V-T curve of H20 at 0.1 MPa as compared to that of G2, which is very flat. The hump was found at temperature range around 50~70 °C, which coincides with the position of the melting peak for mesophase detected via DSC. Since the enthalpy of melting for the mesophase

was relatively small as compared to that for the crystalline phase in other polymers, the small hump could be an evidence for the mesophase ordering though the first-order transition cannot be identified on the V-T of H20. [2, 30-32] The formation of the mesophase may contribute to densification of H20 at lower temperature.

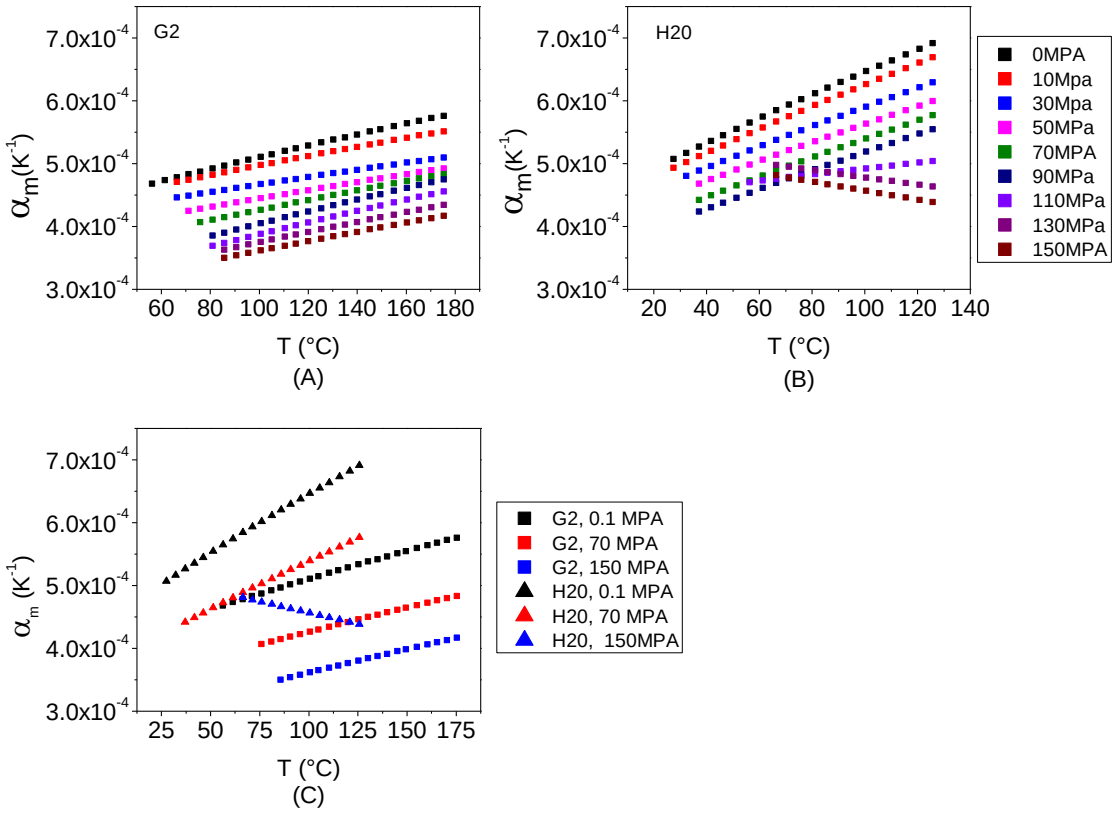

Figure 2.6 *Melt state thermal expansion coefficient, α_m, for (A) G2 and (B) H20 at 0.1,10, 30, 50, 70, 90, 110, 130, and 150 MPa, and for (C) G2 and H20 at 0.1, 70, and 150MPa.*

Under each pressure, H20 shows a higher specific volume than G2 within the same temperature range, which implies that H20 may contain more free volume than G2. The average melt thermal expansivity (E_m), which is defined as $E_m = (\frac{\partial V}{\partial T})_P$, can be determined by the slope of the linear regression of the V-T curves for G2 and H20 as

4.202×10^{-4} cc/(g·K) and 4.853×10^{-4} cc/(g·K) respectively. Higher thermal expansivity of H20 indicates that its translational mobility is higher than that of G2, which may be attributed to its low molecular weight and a high fraction of structures without core as it was revealed by NMR. Nevertheless, the E_m value calculated for H20 before the hump, i.e. below 60 °C, is 4.158×10^{-4} cc/(g·K), which is very close to that of G2. This indicates that the formation of the mesophase may restrict molecular mobility.

To better assess the volumetric properties of G2 and H20, and the effect on mesophase formation, the melt state thermal expansion coefficient (α_m), which is defined as $\alpha_m = (\frac{1}{V})(\frac{\partial V}{\partial T})_P$, was determined for both polymers. α_m values as a function of temperature under different pressures were calculated by taking the first derivative of the binomial fit of each V-T curve and normalizing it by the specific volume at each temperature. Figure 2.6 represents the α_m-T curves of G2 and H20 at melt state at pressures from 0.1 to 150 MPa. As shown in Figure 2.6 (C), the α_m values of H20 are higher than those of G2 at the same pressure, indicating that the free volume content is great in H20. The α_m values of both dendritic polymers are comparable with other linear systems.[15, 33] Interestingly, while all α_m-T curves of G2 increasing with temperature, some of H20 at high pressure show a decreasing trend against temperature. It may be due to the different temperature range used for calculating α_m as the start point for the melting state of H20 was shifted to a higher temperature as pressure increases. Or, it may be attributed to more mesophase formation induced by increasing pressure. To figure out the main cause, α_m of both polymers was recalculated at temperatures 60°C above T_g.

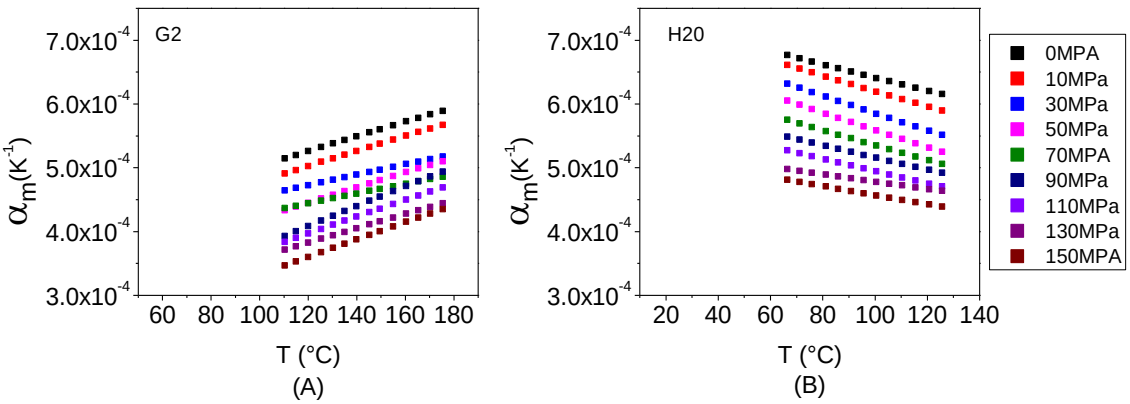

Figure 2.7 *Melt state thermal expansion coefficient, α_m, calculated from 60°C above T_g for (A) G2 and (B) H20 at 0.1,10, 30, 50, 70, 90, 110, 130, and 150 MPa.*

The recalculated α_m values for G2 from 110 to 175 °C and H20 from 66 °C to 125°C are shown in Figure 2.7. One can observe that the recalculated α_m values for G2 using the higher temperature display increasing trend versus temperature as compared to those determined using the entire temperature range for melt state. Moreover, the slopes determined for both sets of α_m curves are very similar. For instance, slopes of α_m-T curves generated with a full range at 0.1, 70, and 150 MPa were determined as 9.06×10^{-7}, 7.75×10^{-7}, 7.92×10^{-7} respectively, while those extracted from temperatures above 110°C were 1.15×10^{-6}, 7.61×10^{-6}, 1.12×10^{-6} respectively. This indicates that as a completely amorphous polymer, the thermal expansion behavior for G2 does not change with the temperature above T_g. On the other hand, the regenerated α_m-T curves for H20 using temperature above 66°C all show a decreasing trend against temperature. This explains that the decreasing trend against the temperature of the previously calculated α_m detected at 130 and 150 MPa is mainly due to the higher temperature range used for the calculation at high pressures. In contrast to G2, the α_m of H20 defined by using

temperatures above 66°C shows opposite temperature dependency to those determined by using the entire temperature range at the melt state. As G2 is completely amorphous, the temperature dependence of the thermal expansion behavior of H20, suggests that some thermal transitions happened at above T_g, which coincides with our founding of mesophase formation through DSC. We can conclude that the formation of the mesophase at temperatures between T_g and above 60°C affects the thermal expansion behavior at these higher temperatures. This also explains the small hump showing on the V-T curves of H20. Interestingly, the pressure seems to have little effect on the formation of the mesophase.

The isothermal compressibility, β_m, which is defined by $\beta_m = -(\frac{1}{V0})(\frac{\partial V}{\partial P})_T$, of both G2 and H20 was also analyzed and compared. The values of β_m at each temperature were determined by taking the first derivative of the binomial fit to each V-P curve and normalizing by the specific volume at each pressure. The calculated β_m values of G2 and H20 plotted as a function of pressure are shown in Figure 2.8 (A) and (B), where the isothermal compressibility of both polymers exhibit decreasing trend against pressure, which can be explained by the lower free volume content at the higher pressures. As shown in Figure 2.8 (C), under the same pressure, the compressibility of H20 is slightly higher than that of G2 at the same temperature, which suggests that the difference of free volume content in both systems may have fewer effects on the compressibility as compared to the thermal expansion coefficient.

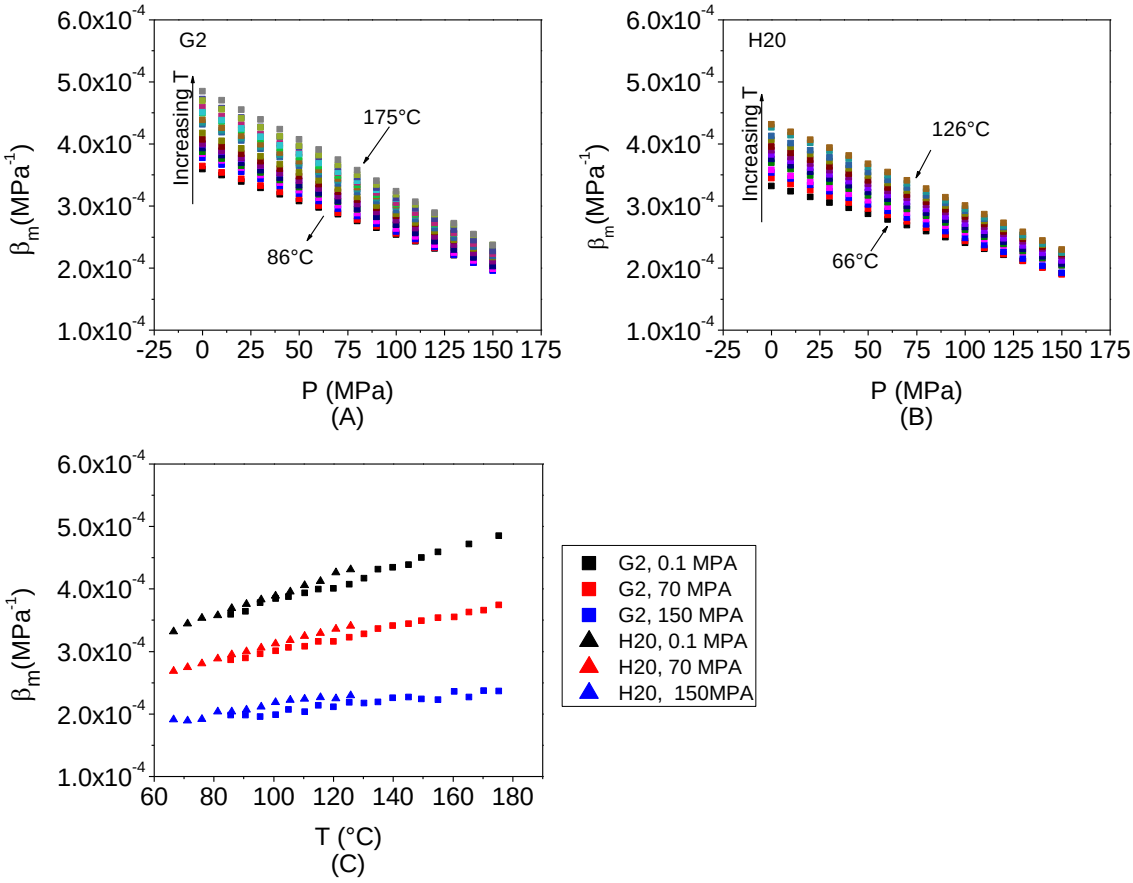

Figure 2.8 *The melt state compressibility, β_m, as a function of pressure for (A) G2 between 86-175°C and (B) H20 between 66 -126°C. (C) β_m, as a function of temperature for G2 and H20 at pressures equal to 0.1, 70, and 150 MPa.*

The thermodynamic properties and the free volume content in both G2 and H20 were then investigated via a fitting entire set of melt state PVT data to the SS-EOS. The volume-temperature (V-T) curves for both G2 and H20 at pressures from 0.1 to 150 MPA along with the SS-EOS fits are presented in Figure 2.9. It can be observed that the SS-EOS can fit the PVT surface well.

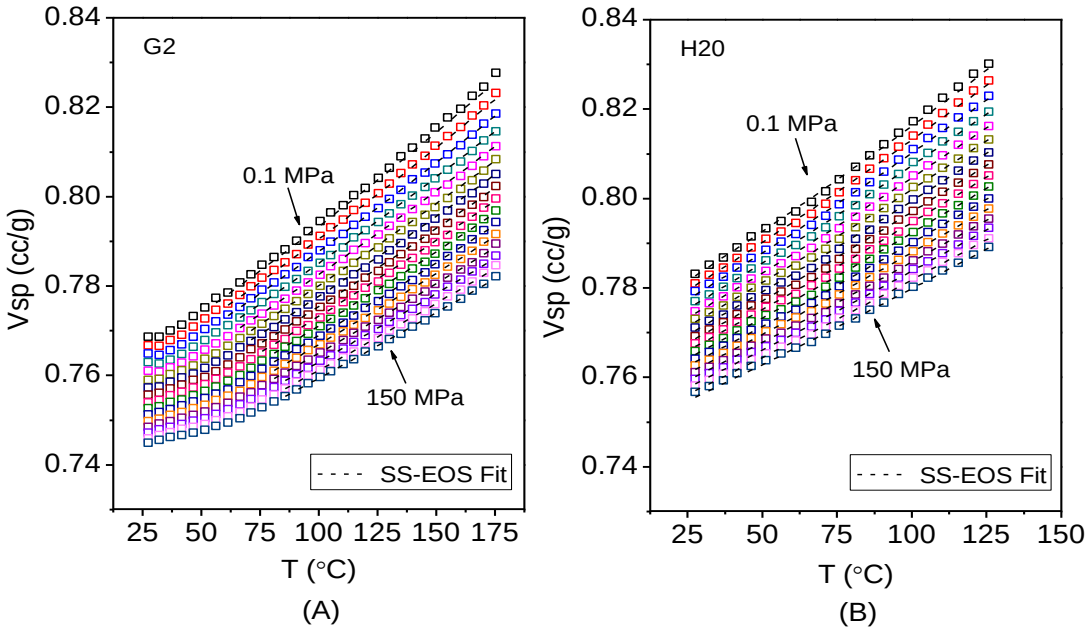

Figure 2.9 *Isobaric volume-temperature data and SS-EOS fit curves at 0.1, 10, 20, 30, 40, 50, 60, 70, 80, 90, 100, 110, 120, 130, 140, and 150 MPa for (A)G2 and (B) H20.*

The fitting parameters of the SS-EOS extracted for G2 and H20 are listed in Table 2.3. The correlation coefficient, r^2, of both G2 and H20 were determined to be 0.9999, which indicates that the SS-EOS can provide accurate fitting for both polymers. According to the lattice-hole theory, V* is the specific volume of s-mer which occupies one lattice site with the corresponding size to the minimum Lennard-Jones potential. The similar values of the scaling parameter V* determined for G2 and H20 is due to their similar chemical nature as V* is proportional to Van der Waals volume. [11] The V* values for both G2 and H20 are relatively small as compared to other linear polymer systems.[12] This can be due to their branching structure, as the poly(benzyl PBED) also shows lower V* as compared to the corresponding linear PS. [9] The molecular mass of the statistical

segments which occupies one lattice site, M_s, was calculated by $M_s = \frac{R}{3} \cdot \frac{T^*}{P^*V^*}$, where R = 8.314 J/(K·mol). The M_s values for G2 and H20 were determined as 38.5 and 22.25 g/mole, which are about 33% and 20% of the molecular mass of the bis-MPA repeat unit (115 g/mol) respectively. Lower M_s value of H20 suggests that the flexibility of H20 is higher, which is due to the ether linkage on the PP50 core. The trend of the M_s also reflects in the v*, which is defined as $v^* = V^* M_s$.The molar activation energy, ϵ*, which is proportional to T*, is higher for G2 than H20, which suggests that the hydrogen bonding interaction is higher in G2 as compared to H20. This probably due to the higher fraction of the OH···OH in G2, which requires more OHs to be associated.

Table 2.3 *Parameters extracted from the SS-EOS fit.*

	P*(MPa)	V*(cc/g)	T*(K)	M_s (g/mol)	v*(cc/mol)	ϵ*(kJ/mol)	r^2
G2	1144.1	0.7760	12346	38.5380	29.9055	3.4215	0.9999
H20	1333.2	0.7747	10708	28.7297	22.2581	2.9675	0.9999

The free volume and occupied volume were also extracted for G2 and H20 by utilizing the SS-EOS. The specific free volume (V_f), occupied volume (V_{occ}), and fractional free volume (h) for G2 and H20 were plotted as a function of temperature at different pressures in Figure 2.10. From Figure 2.10 (A) and (B), one can observe that at the same temperature, H20 displays greater the specific free volume than G2 while the occupied volume of G2 and H20 is similar, which suggests that the greater specific volume of H20 is mainly contributed by its higher free volume. The increasing trends of

V_f and h against temperature lead to the thermal expansivity of both polymers. This can be observed from Figure 2.10 (A) and (C), that the slopes of the V_f-T and the h-T curves for H20 are greater than those of G2, which agrees well with the greater thermal expansion coefficient of H20. The slower increase of free volume in G2 can be attributed to the stronger hydrogen bonding interaction, which revealed by ϵ^*.

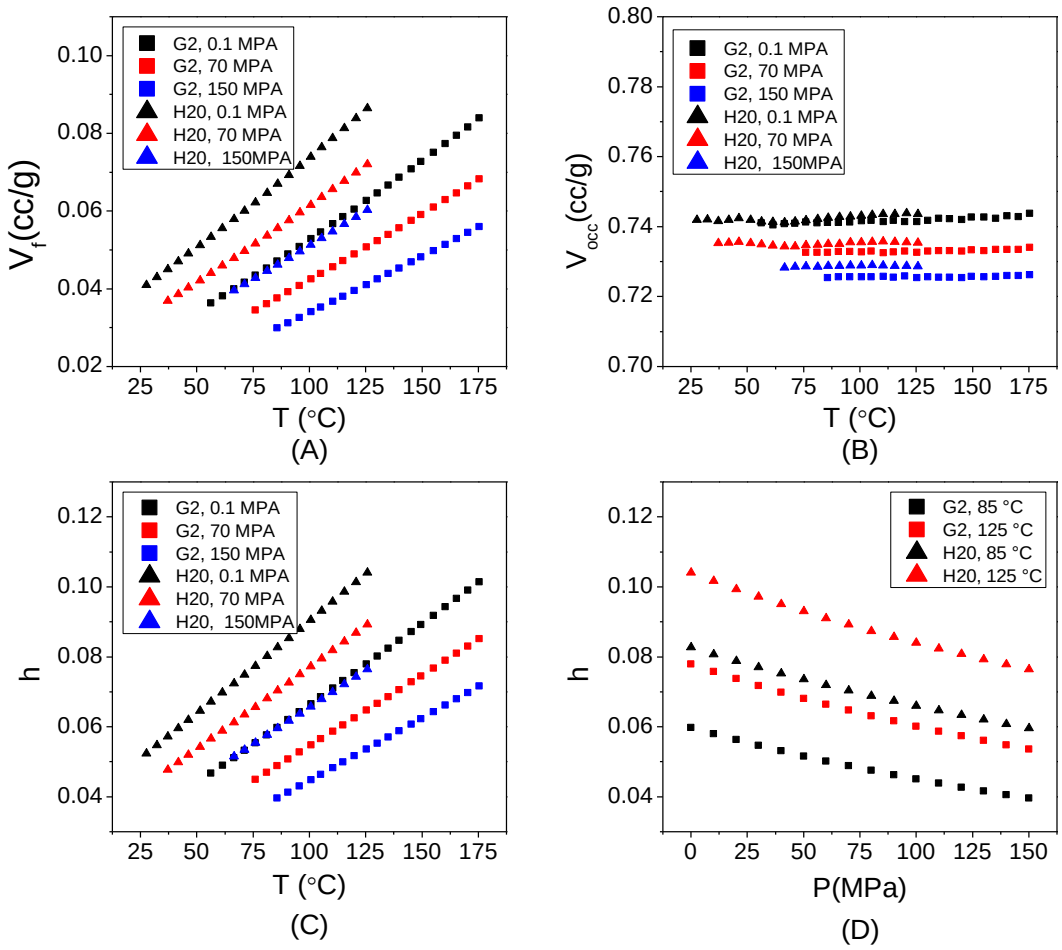

Figure 2.10 *Specific (A) free volume (V_f), (B) occupied volume (V_{occ}), and (C) fractional free volume (h) for G2 and H20 as a function of temperature at 0.1, 70, and 150 MPa. (D) fractional free volume for G2 and H20 as a function of pressure at 85°C and 125°C.*

On the other hand, as shown in Figure 2.10 (D), the pressure dependence of h for G2 and H20 is very close, which is consistent with the small difference between the compressibility of G2 and H20. Besides, the pressure dependency of V_{occ} suggests that in addition to free volume, the occupied volume also contributes to the compressibility.

2.4 Conclusion

The chemical nature of the G2 and Boltorn™ H20 was carefully analyzed and compared via NMR. Similar OH/CO ratios and OH concentrations were determined, which indicates that the chemical nature of G2 and H20 are very close. The formation of H-bonds in both polymers was assessed via FTIR, where a higher fraction of OH···OH H-bonds was found in G2 as compared to H20.

The glass transition temperature of G2 and H20 was measured by DSC. DSC results showed that Tg of H20 was much lower than that of G2, which is due to its lower molecular weight, and broad molecular weight distribution as revealed by NMR.

The volumetric properties of G2 and H20 were probed via PVT dilatometry, where H20 displays greater thermal expansivity as compared to G2. A small hump can be observed on the V-T curves of H20 at above T_g, which is due to the formation of the mesophase. Through the analysis of the thermal expansion coefficient, it was found that the formation of mesophase at temperatures between Tg and 60°C above Tg affects the thermal expansion behavior of H20 at higher temperatures. The compressibility of G2 and H20 was also analyzed, which shows a decreasing trend against pressure. At the same temperature, H20 shows slightly greater compressibility than that of G2.

The SS-EOS was found to be able to fit the PVT surface of G2 and H20 with accuracy. The thermodynamic parameters extracted from SS-EOS reveal that the flexibility of the H20 molecule is higher than that of G2, which is attributed to the ether bonds in the PP50 core. It was also found that the hydrogen bonding interaction in G2 is greater, which can be ascribed to the higher fraction of OH···OH H-bonds. Free volume and occupied volume were also determined via the fitting of SS-EOS. Higher free volume was found in H20 which contributes to its higher specific volume. The slower increase of free volume with temperature in G2 can be attributed to the stronger hydrogen bonding interaction. The pressure dependence of h for G2 and H20 is very close, which shows good consistent with the small difference between the compressibility of G2 and H20.

2.5 References

1. Zagar, E.; Huskic, M.; Grdadolnik, J.; Zigon, M.; Zupancic-Valant, A., Effect of annealing on the rheological and thermal properties of aliphatic hyperbranched polyester based on 2, 2-bis (methylol) propionic acid. *Macromolecules* **2005,** *38* (9), 3933-3942.
2. Syed, M. N. Hydrogen Bond-Mediated Structural Order in Hydroxylated Bis-MPA Dendritic Polymers: Experimental and Molecular Dynamics Simulation Study. Ph.D. Thesis, The University of Southern Mississippi, 2015.
3. Nibbering, E. T. J.; Dreyer, J.; Kühn, O.; Bredenbeck, J.; Hamm, P.; Elsaesser, T., Vibrational dynamics of hydrogen bonds. In *Analysis and Control of Ultrafast Photoinduced Reactions*, Kühn, O.; Wöste, L., Eds. Springer Berlin Heidelberg: Berlin, Heidelberg, 2007; pp 619-687.
4. Lin-Vien, D.; Colthup, N. B.; Fateley, W. G.; Grasselli, J. G., CHAPTER 4 - Alcohols and Phenols. In *The Handbook of Infrared and Raman Characteristic Frequencies of Organic Molecules*, Lin-Vien, D.; Colthup, N. B.; Fateley, W. G.; Grasselli, J. G., Eds. Academic Press: San Diego, 1991; pp 45-60.
5. Athokpam, B.; Ramesh, S. G.; McKenzie, R. H., Effect of hydrogen bonding on the infrared absorption intensity of OH stretch vibrations. *Chem. Phys.* **2017,** *488*, 43-54.
6. Iogansen, A., Direct proportionality of the hydrogen bonding energy and the intensification of the stretching ν (XH) vibration in infrared spectra. *Spectrochimica Acta Part A: Molecular and Biomolecular Spectroscopy* **1999,** *55* (7), 1585-1612.
7. Žagar, E.; Huskić, M.; Žigon, M., Structure-to-Properties Relationship of Aliphatic Hyperbranched Polyesters. *Macromol. Chem. Phys.* **2007,** *208* (13), 1379-1387.

8. Žagar, E.; Grdadolnik, J., An infrared spectroscopic study of H-bond network in hyperbranched polyester polyol. *J. Mol. Struct.* **2003,** *658* (3), 143-152.
9. Simha, R.; Utracki, L. A., PVT properties of linear and dendritic polymers. *J. Polym. Sci., Part B: Polym. Phys.* **2010,** *48* (3), 322-332.
10. Hay, G.; Mackay, M. E.; Hawker, C. J., Thermodynamic properties of dendrimers compared with linear polymers: General observations. *J. Polym. Sci., Part B: Polym. Phys.* **2001,** *39* (15), 1766-1777.
11. Utracki, L. A.; Jamieson, A. M., *Polymer physics: from suspensions to nanocomposites and beyond*. John Wiley & Sons: 2011.
12. Rodgers, P. A., Pressure–volume–temperature relationships for polymeric liquids: A review of equations of state and their characteristic parameters for 56 polymers. *J. Appl. Polym. Sci.* **1993,** *48* (6), 1061-1080.
13. Simha, R.; Carri, G., Free volume, hole theory and thermal properties. *J. Polym. Sci., Part B: Polym. Phys.* **1994,** *32* (16), 2645-2651.
14. Zoller, P., PVT relationships and equations of state of polymers. In *Polymer handbook*, Brandrup, J.; Immergut, E. H., Eds. John Wiley & Sons: New York, 1989; pp 475-483.
15. Dlubek, G.; Bondarenko, V.; Pionteck, J.; Supej, M.; Wutzler, A.; Krause-Rehberg, R., Free volume in two differently plasticized poly (vinyl chloride) s: a positron lifetime and PVT study. *Polymer* **2003,** *44* (6), 1921-1926.
16. Ihre, H.; Padilla De Jesús, O. L.; Fréchet, J. M., Fast and convenient divergent synthesis of aliphatic ester dendrimers by anhydride coupling. *J. Am. Chem. Soc.* **2001,** *123* (25), 5908-5917.

17. Elmahdy, M. M.; Chrissopoulou, K.; Afratis, A.; Floudas, G.; Anastasiadis, S. H., Effect of Confinement on Polymer Segmental Motion and Ion Mobility in PEO/Layered Silicate Nanocomposites. *Macromolecules* **2006,** *39* (16), 5170-5173.
18. Hölter, D.; Burgath, A.; Frey, H., Degree of branching in hyperbranched polymers. *Acta Polym.* **1997,** *48* (1-2), 30-35.
19. Olabisi, O.; Simha, R., A semiempirical equation of state for polymer melts. *J. Appl. Polym. Sci.* **1977,** *21* (1), 149-163.
20. Utracki, L. A.; Simha, R., Analytical representation of solutions to lattice-hole theory. *Macromol Theor Simul* **2001,** *10* (1), 17-24.
21. Žagar, E.; Žigon, M.; Podzimek, S., Characterization of commercial aliphatic hyperbranched polyesters. *Polymer* **2006,** *47* (1), 166-175.
22. Žagar, E.; Žigon, M., Aliphatic hyperbranched polyesters based on 2, 2-bis (methylol) propionic acid-Determination of structure, solution and bulk properties. *Prog. Polym. Sci.* **2011,** *36* (1), 53-88.
23. Adrjanowicz, K.; Kaminski, K.; Dulski, M.; Jasiurkowska-Delaporte, M.; Kolodziejczyk, K.; Jarek, M.; Bartkowiak, G.; Hawelek, L.; Jurga, S.; Paluch, M., Dynamic Glass Transition and Electrical Conductivity Behavior Dominated by Proton Hopping Mechanism Studied in the Family of Hyperbranched Bis-MPA Polyesters. *Macromolecules* **2014,** *47* (16), 5798-5807.
24. Krisanangkura, P.; Packard, A. M.; Burgher, J.; Blum, F. D., Bound fractions of methacrylate polymers adsorbed on silica using FTIR. *J. Polym. Sci., Part B: Polym. Phys.* **2010,** *48* (17), 1911-1918.

25. Coleman, M. M.; Lee, K. H.; Skrovanek, D. J.; Painter, P. C., Hydrogen bonding in polymers. 4. Infrared temperature studies of a simple polyurethane. *Macromolecules* **1986,** *19* (8), 2149-2157.

26. Tanis, I.; Karatasos, K., Local dynamics and hydrogen bonding in hyperbranched aliphatic polyesters. *Macromolecules* **2009,** *42* (24), 9581-9591.

27. Žagar, E.; Žigon, M., Molar mass distribution of a commercial aliphatic hyperbranched polyester based on 2, 2-bis (methylol) propionic acid. *J. Chromatogr. A* **2004,** *1034* (1), 77-83.

28. Malmström, E.; Johansson, M.; Hult, A., The effect of terminal alkyl chains on hyperbranched polyesters based on 2, 2-bis (hydroxymethyl) propionic acid. *Macromol. Chem. Phys.* **1996,** *197* (10), 3199-3207.

29. Malmström, E.; Hult, A.; Gedde, U.; Liu, F.; Boyd, R., Relaxation processes in hyperbranched polyesters: influence of terminal groups. *Polymer* **1997,** *38* (19), 4873-4879.

30. Lagaron, J. M.; Vickers, M. E.; Powell, A. K.; Davidson, N. S., Crystalline structure in aliphatic polyketones. *Polymer* **2000,** *41* (8), 3011-3017.

31. Jang, J.; Lee, D. K., Plasticizer effect on the melting and crystallization behavior of polyvinyl alcohol. *Polymer* **2003,** *44* (26), 8139-8146.

32. Hamada, F.; Wunderlich, B.; Sumida, T.; Hayashi, S.; Nakajima, A., Density and heat of fusion of folded chain polyethylene crystals. *J. Phys. Chem.* **1968,** *72* (1), 178-185.

33. Dlubek, G. n.; Pionteck, J. r.; Rätzke, K.; Kruse, J.; Faupel, F., Temperature Dependence of the Free Volume in Amorphous Teflon AF1600 and AF2400: A

Pressure− Volume− Temperature and Positron Lifetime Study. *Macromolecules* **2008,** *41* (16), 6125-6133.

CHAPTER III - COMPARATIVE STUDY OF DIELECTRIC RELAXATION CORRELATED TO HYDROGEN BONDING ORGANIZATION BETWEEN BIS-MPA BASED HYPERBRANCHED POLYMER AND DENDRIMER: GAMMA-RELAXATION

Abstract

Dynamic relaxation studies performed on 2,2-bis(hydroxymethyl)propionic acid (bis-MPA) based hyperbranched polymers (HBPs) have not yet been extended to their dendrimer analogs which require considerable synthetic efforts. In this chapter, a comparative study was conducted on a bis-MPA based second-generation HBP, BoltornTM H20, with its dendrimer analog, G2. The γ-relaxation of both G2 and H20, which is strongly affected by hydrogen bonding, was investigated via dielectric spectroscopy, and their hydrogen bonding organization which is mainly affected by branching irregularity and core structure was studied via molecular dynamics simulation. High dielectric constant and high permittivity strength were determined for G2 and H20, especially for G2, which was ascribed to the formation of H-bonded associations. The pre-exponential factors of γ-relaxation show a large deviation from the ideal value for Debye relaxation, especially for G2, which reveals the associative nature of the γ-relaxation. Through dielectric analysis of partially and fully esterified H20, these unique dielectric properties of H20 and G2, including high dielectric constant, high permittivity strength, high activation energy, and low preexponential factor attributed to the formation of H-bonded chain-like clusters. Molecular dynamics simulation was conducted to analyze the hydrogen bonding organization. The chain-like cluster $O_{N+1}H_N$, defined as a string of consecutive O-H···O groups connected by H-bonded was also identified in the

G2 system. A similar study was also conducted on H20 and its corresponding dendrimer, D20, in order to reveal how core structure and branching irregularity affect the formation of H-bonded clusters. G2 displays a higher fraction of long clusters than H20, which is inconsistent with its higher dielectric constant and its larger deviation from Debye type relaxation. A higher fraction of long clusters in G2 was due to its higher portion of OH···OH H-bonds, which agrees well with the FTIR results. How the core structure and branching irregularity affects the formation of H-bonds was also analyzed.

3.1 Introduction

The H-bond organization and molecular dynamics of Boltorn™ H20 and H30 were probed via atomistic molecular dynamics (MD) simulation by Tanis etc., where the most abundant type of H-bonds was identified as those between hydroxyls, and slower local dynamics were ascribed to a higher fraction of intramolecular hydrogen bonding. [1] Following that, our previous study on the H-bond organization within the bis-MPA based dendritic polymers identified 'chain-like' clusters formed by H-bonded O-H···O groups in systems via MD simulation. [2] However, the existence of the clusters becomes questionable when considering broad structure deviations of Boltorn™ type HBPs, which cannot be completely simulated. [3,4] Besides, the formation of the mesophase of the HBPs cannot be computed via MD simulation due to the limitation of the time scale. [2] On the other hand, dendrimers, which are monodispersed, well-defined, and completely amorphous, would be ideal for simulation studies. Hence, a simulation study on the hydrogen bonding formation of a well-defined bis-MPA based dendrimer system can be easily verified via experimental methods.

Dielectric spectroscopy was employed to probe the molecular dynamics in bis-MPA based HBPs due to its high sensitivity and wide range of temperatures and frequencies. However, these studies have not yet been extended to their dendrimer analogs due to their strict synthetic requirements. According to the early studies conducted on bis-MPA based HBPs using dielectric relaxation spectroscopy, high activation values were reported for their γ-relaxation, which was assigned to hydroxyl motions and were attributed to the extensive hydrogen bonding in the system. [5-8] For instance, in the most recent study conducted by Androulaki, etc., the activation energy of γ-relaxation of neat HBPs, which is ~65 kJ/mole, was significantly reduced by half when the HBPs were intercalated by hydrophilic sodium montmorillonite (MMT). [8] Though it was agreed that the high activation energy was strongly correlated to hydrogen bonding within bis-MPA based HBP systems, other features of the γ-relaxation, such as pre-exponential factor and permittivity strength, have been rarely discussed. Therefore, how hydrogen bonding defines the mechanism of γ-relaxation was not well explained. Additionally, as these studies were all focused on the relaxation processes, their high dielectric constant and the rationale behind it has been neglected. It was found that small H-bonded molecules, for instance, water exhibits very high dielectric constant values at ambient conditions. Except for the high density of dipoles, one of the major factors for the high dielectric constant is that water forms association via H-bonds and respond to electric fields cooperatively in groups of about three rather than individually. [9, 10] Hence, we assume that that the high dielectric constant of bis-MPA based dendritic polymers may be correlated with the formation of H-bonded clusters.

Therefore, a simulation study on the hydrogen bonding in addition to a dielectric study on the molecular dynamics of a bis-MPA based well-defined dendrimer system would provide us an insightful understanding of the mechanism of the sub-T_g relaxation in hydroxylated dendritic polymers. Moreover, comparing the well-defined dendrimer with corresponding HBP will reveal how hydrogen formation and correlated relaxation properties are affected by structural irregularity and polydispersity. It was hypothesized that the high dielectric constant and high activation energy of the γ-relaxation of bis-MPA based dendritic polymers is due to the formation of H-bonded clusters.

3.2 Experimental Section

3.2.1 Materials and sample preparation

The second-generation hyperbranched polyester (HBP), Boltorn™ H20 was kindly donated by Perstorp Polyols Inc. This commercially available dendritic polymer was synthesized via the one-pot method using ethoxylated pentaerythritol (PP50) core and 2,2-bis(methylol)propionic acid (bis-MPA) branching monomer.

Boltorn hyperbranched polyesters of this class are typically designated in the literature as HX0, where X denotes the pseudo-generation number. The theoretical (based on composition) molecular weight of H20 is 1749 g/mol. As reported by Perstorp the number average molecular weight of H20 however is somewhat greater, i.e. 2100 g/mol. The degree of branching (DB) of H20 determined by NMR has been reported as 0.261 using the definition given by Frey[11].

For a comparison with H20, the perfectly branched second-generation dendrimer, designated hereafter as G2, was synthesized in house from bis-MPA branching monomer

and pentaerythritol core using a diverging approach via anhydride coupling as described elsewhere. [13, 14] The molecular weight of G2 based on its structure was calculated as 1529.5 g/mol. Nearly the same weight, 1528.8 g/mol, was determined by MALDI-ToF MS, thus confirming the unimolecular distribution of G2. Thin films of G2 and H20 were prepared using the Carver Melt Press by following the procedure detailed in Chapter II.

End capping modification of H20 (targeting 50% of esterification) was carried out following the methodology of alkylation proposed by Malmstrom and Hult as shown in Scheme 3.1. [15] In a 500 ml round bottom flask, 5.0 g (2.86 mmol) of H20 was first dissolved in 40 ml of acetone. Then, triethylamine (3.47 g/ 34.4 mmol) and 4-dimethyl aminopyridine (DMAP) (0.30g/2.4 mmol) were successively added to the flask and mixed with the solution. The flask was cooled to 0^{o}C using an ice-water bath. In parallel, liquid acetyl chloride (1.80g/22.9mmol) was mixed with 50 ml acetone in a dropping funnel and added to the flask dropwise over 3 hours to initiate the reaction which then continued overnight until completion. To separate the modified polymer from trimethylamine hydrochloride, $NaHCO_3$ containing water solution (10% wt/wt) was poured into the flask. After the phase separation, the bottom liquid layer was enriched with the polymer while the top layer mainly contained a water-salt solution. The bottom liquid layer containing polymer was collected using a separatory funnel. Importantly, dichloromethane was added to ease the flow of a very viscous polymer enriched phase through the funnel. To further purify the polymer containing phase from $NaHCO_3$, HCl water solution (2M) was then added and the bottom layer containing the polymer phase was again collected. The last procedure was repeated until no bubbles were formed indicative of no NaHCO3 left in the polymer containing phase. Then the polymer

containing phase was washed with DI water to remove NaCl, separated and collected again. The remaining solution was separated from the aqueous phase and repeatedly checked with $AgNO_3$ for Cl ions and when not found, the procedure of purifying the modified polymer from the salts was assumed to be completed. The polymer containing phase was dried by adding $MgSO_4$ to remove water. The pure product was obtained after evaporation of the remaining traces of acetone and dichloromethane. The product resembled a highly viscous liquid. The structure of H20-derivative was analyzed by NMR and FTIR spectroscopy.

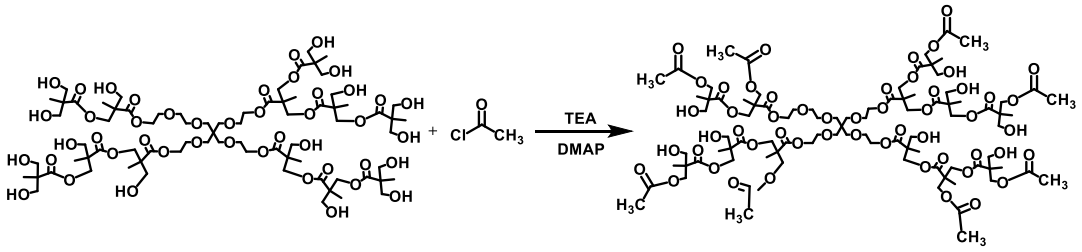

Scheme 3.1 *End capping modification of Boltorn^{TM} H20 with acetyl chloride.*

3.2.2 Experimental methods

Thermal behavior was investigated by differential scanning calorimetry (DSC) using a TA Instruments DSC Q-100. The calibration was carried out using indium and sapphire standards. Samples were first heated to 200°C at a rate of 10°C/min to erase thermal history, quenched to -90°C at 5°C/min, and then heated to 200°C at 10°C/min. The second heating scans were reported.

The infrared spectra were collected using a Perkin-Elmer 1600 FTIR spectrometer. Thin films on the NaCl plates were prepared by solution casting using

acetone. After solvent evaporation, the films were dried in vacuum for 12 hr to remove any traces of acetone and water.

The ^{1}H NMR spectra were collected using a Varian VXR 300 NMR spectrometer. For the measurements, the polymer was dissolved in DMSO-*d*6 at the concentration of 1% (wt/wt).

Dielectric measurements were carried out by a Novocontrol GmbH Concept 80 Broadband Dielectric Spectrometer using the frequency range 0.01 to 1 MHz and temperature range -100 to 100 °C respectively. Each sample was loaded into the sample cell (BDS1308) designed for testing liquids then heated to form a melt and then sandwiched between two stainless-steel electrodes separated by a Teflon ring-spacer with an inner diameter of 17.4 mm and thickness of 0.25 mm. Prior to the dielectric measurement, each electrode-sample assembly was dried in vacuum at 60 °C for 24hr and then conditioned in a nitrogen atmosphere with 20% RH for another 24hr. Dielectric spectra were recorded every five degrees during cooling. At each testing temperature, samples were thermally equilibrated for 30 min before data collection.

Wide-angle X-ray diffraction (WAXS) experiments were performed under 1 mbar using a Rigaku S-Max 3000 3 pinhole SAXS system, equipped with a rotating anode emitting X-ray with a wavelength of 0.154 nm (Cu Ka). The sample-to-detector distance was 82.5 mm, and the q-range was calibrated using a silver behenate standard. WAXS two-dimensional diffraction patterns were obtained using an image plate with an exposure time of 1 h. WAXS profiles were vertically shifted to facilitate a comparison of peak positions. WAXS data were analyzed using the SAXSGUI software package to obtain radically integrated WAXS intensity versus 2θ.

Molecular Dynamics (MD) Simulations

MD simulations were used to model the structure of G2, G2-CH3, H20, and D20 system in the bulk, among which G2-CH3 is the fully acetylated G2 and D20 is the corresponding dendrimer of H20. Chemical structures of these 4 dendric polymers were shown in Figure 3.1. The simulation was conducted using Materials Studio software available from Accelrys® (Accelrys Software, Inc., San Diego). The Amorphous Cell program was used to construct an initial amorphous packing structure containing in each case 50 molecules. Each atom and molecule in the amorphous cell were assigned a unique name, e.g. O22, H5876 Molecule5, etc. The amorphous cell was constructed with a starting density of 0.5 $g \cdot cm^{-3}$ and atomistically modeled using the Discover program and the COMPASS forcefield. The Ewald summation method was used for all energy calculations. Following minimization, MD runs of alternating NVT and NPT ensembles, between 650 K and 298 K and 1750-0.1 MPa were performed to obtain a relaxed amorphous cell at 298 K and 1 atm. The appropriateness of the forcefield and the simulation protocol adopted for the systems were verified by comparing the final densities obtained from simulations with ones determined experimentally. In the final stage of the simulation, 1ns production runs (NVE ensembles) with a time step of 1 fs and frame-saving frequency of 0.1ps were performed, creating final trajectory files consisting of 10,000 frames, which were used for further analysis.

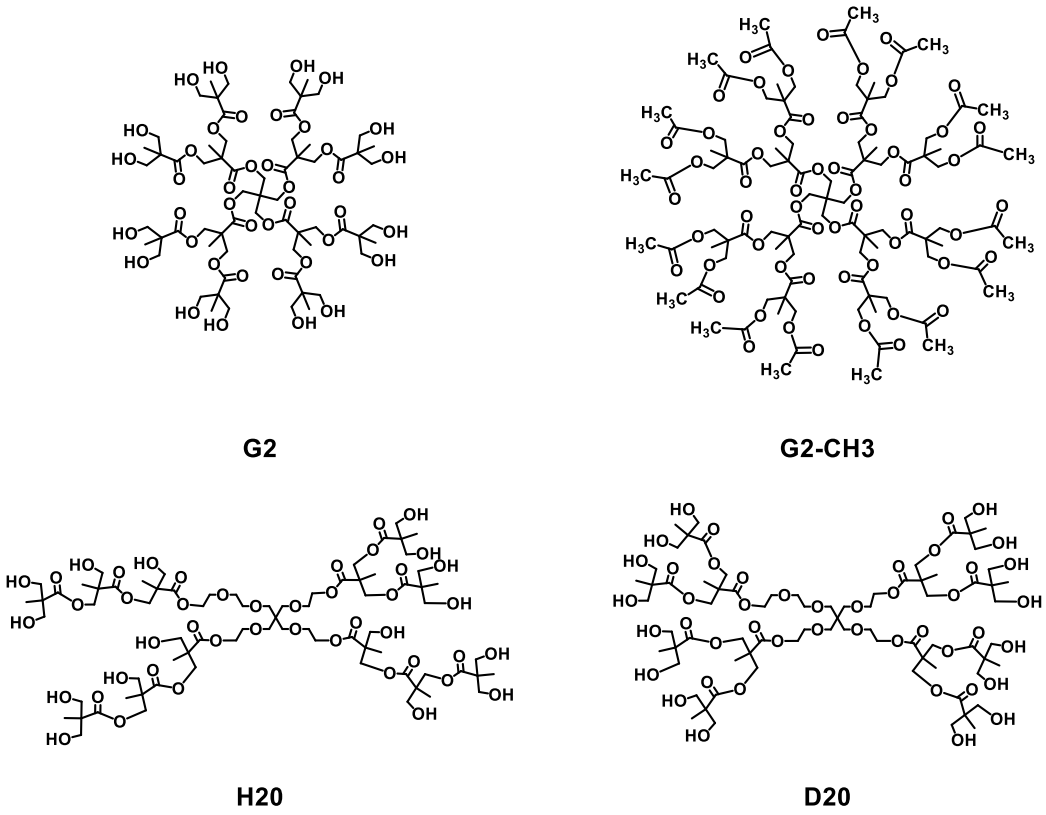

Figure 3.1 *Chemical structures of G2, G2-CH3, H20, D20.*

The structure of the three systems was analyzed using the Forcite program. The radius of gyration of dendritic molecules in the bulk, pair correlation function (PCF), and the X-ray scattering pattern, have been calculated. The global configuration of each dendritic polymer was described by the radius of gyration, R_g, which is the root mean square distance of the atoms in the molecule from their common center of mass, calculated as follows

$$R_g{}^2 = \frac{\sum_{i=1}^{N} m_i s_i^2}{\sum_{i=1}^{N} m_i} \tag{21}$$

where m_i denotes the mass of atom *i*, *s* denotes the distance of atom *i* from the center of mass, and N denotes the total number of atoms.[16] The R_g was calculated for all molecules in the amorphous cell and over all frames in the trajectory file.

The pair correlation function (PCF), g(r), which describes how the number density of atoms varies as a function of distance from a reference particle has been calculated as follows

$$g(r) = \frac{1}{4\pi r^2}\frac{1}{N\rho}\sum_{i=1}^{N}\sum_{k\neq i}^{N}\langle\delta(r - |r_k - r_i|)\rangle \tag{22}$$

where *N* is the total number of atoms, $\rho=N/V$ is the average number density of atoms in the cell, and the angle brackets indicate an ensemble average. [17] The total, and inter- and intramolecular g(r) was calculated using a bin interval of 0.1 Å. Periodic self-interactions were included in the calculations.

X-ray scattering patterns were simulated within a 2θ scattering angle range of 1 to 60° using λ = 0.15417 nm. The scattering intensity was calculated based on the Debye scattering equation as follows

$$I(Q) = \sum_i \sum_j f_i(Q) f_j(Q) \frac{\sin(Q r_{ij})}{Q r_{ij}} \tag{23}$$

where *Q* is the scattering vector ($Q = |\boldsymbol{Q}| = 4\pi sin(\theta)/\lambda$), r_{ij} is the vector joining atoms *i* and *j* $\left(r_{ij} = |r_i - r_j|\right)$, and $f_i(Q)$ and $f_j(Q)$ are the atomic scattering factors of these atoms respectively.[18] The Forcite script utilized a binning function to calculate atom pair separations, r_{ij}, for each atomic pair, which are averaged over all atoms in the amorphous cell and all frames in the trajectory file.[19] Atom pair separations greater than the cutoff

distance were not included in the calculation. For all simulations, the cutoff distance was set to half the length of each respective amorphous cell.

A custom-made program, 'Traced Hbonds' was employed to investigate the formation of the H-bonds in all simulated systems. In this study, the H-bond was defined as the attractive interaction between one donor hydrogen from a hydroxyl group and acceptor oxygen from another moiety. As shown in Figure 3.2, the proton acceptor group OY can be anyone from hydroxyl, carbonyl, ester, and ether groups. The criteria of the H-bond were a maximum hydrogen acceptor distance of 2.5 Å and a minimum donor-acceptor angle of 90°. The software was used to analyze the final trajectory files for all hydroxylated systems.

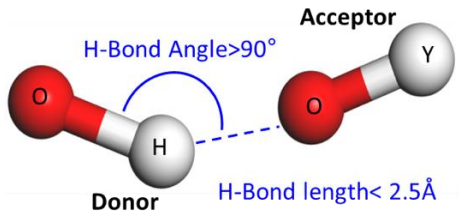

Figure 3.2 *Schematic of a hydrogen bond between a donor hydroxyl group, O-H, and an acceptor group, O-Y. The dashed line represents the hydrogen bond. The hydrogen donor atom is highlighted in blue and the oxygen acceptor atom in red. The hydrogen bond length and angle are indicated.*

The chain-like cluster, represented by $O_{N+1}H_N$, was defined as a string of consecutive O-H···O groups connected by H-bond which starts with oxygen from the donor hydroxyl group and ends with an oxygen atom from an acceptor group. The length of one hydrogen bonded chain-like cluster was defined by the number H-bonds it

contains. For instance, the H-bonded cluster shown in Figure 3.3 starts with the 1st O and ends with the 4th O, of which length equals to 3.

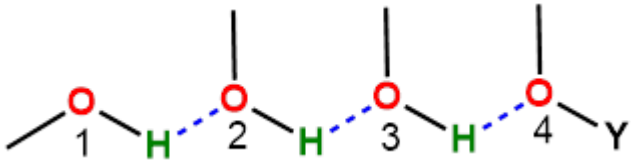

Figure 3.3 *Schematic of a hydrogen-bonded cluster where the H-bond was represented by blue dash line, acceptor oxygen atoms are highlighted in red, and the donor hydrogen atoms are highlighted in green.*

3.3 Results and Discussion

3.3.1 NMR

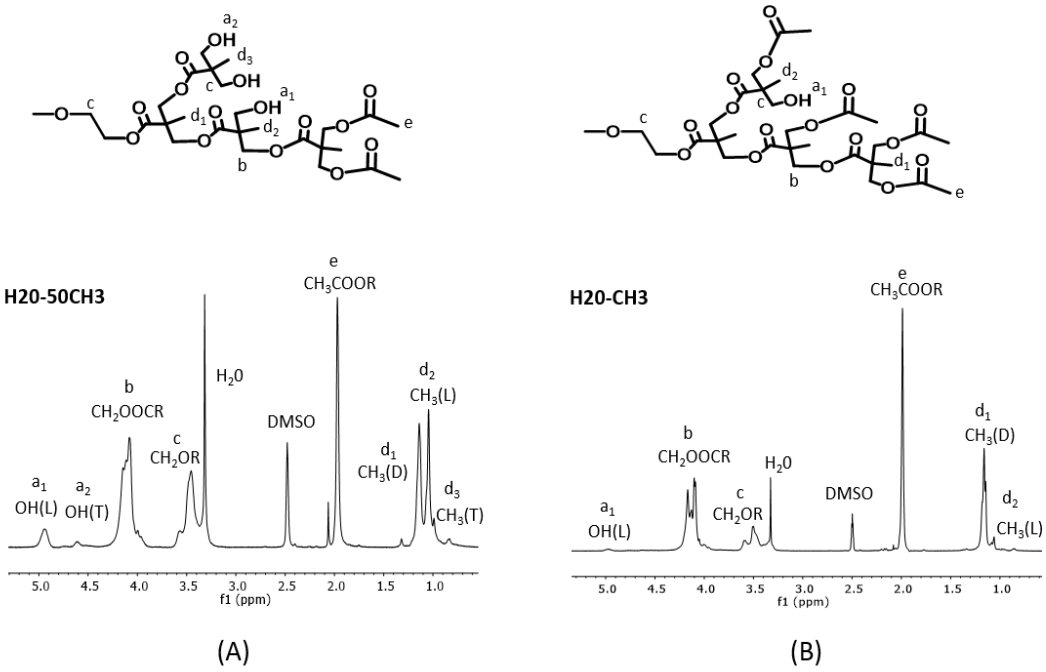

Figure 3.4 *NMR spectra of (A)H20-50CH3, (B) H20-CH3.*

The partially and fully esterified H20 was termed as H20-50CH3 and H20-CH3 respectively, where 50 stands for the theoretical degree of esterification. The NMR spectra of H20-50CH3 and H20-CH3 are presented in Figure 3.4 and the integrated values of each peak are also listed in Table 3.1. Derivatization of H20 with acetyl chloride changed the NMR spectrum significantly. An extra peak appeared at 1.99 ppm for both H20-50CH3 and H20-CH3, which was assigned to the protons concomitant with acetyl methyl groups, the products of hydroxyl group esterification. Comparing H20-50CH3 with H20-CH3, the intensity of proton signals associated with both terminal and linear hydroxyls was noticeably reduced but to a different extent. The greater $I(OH)_L$ peak as compared to $I(OH)_T$ indicates that the remaining unreacted hydroxyls in H20-50CH3 after derivation are predominantly linear hydroxyls. For H20-CH3, only small traces of linear hydroxyls can be detected, indicating the esterification is close to completion. By comparing the $[I(OH)_T + I(OH)_L]/I(CH_3)$ ratio for H20-50CH3 and H20-CH3 with unmodified H20, the actual degree of esterification of them was determined to be 60.1% and 97.3% respectively, where the former one is little higher than the target value.

Table 3.1 *Integrals of the ^{1}H NMR signals of individual protons for H20, H20-50CH3, and H20-CH3.*

Assignment	H20	H20-50CH3	H20-CH3
I(CH_3)D	3.86	17.66	32.09
I(CH_3)L	22.16	14.69	3.86
I(CH_3)T	10.14	3.4	-
I(CH_2OR)	47.69	24.04	18.56
I(CH_2OOCR)	24.13	38.82	54.12
I(OH)T	9.56	1.9	-
I(OH)L	7.02	4.28	0.44
I(CH_3COOR)	-	24.44	42.39
Calculated values			
DB	0.258		
OH/CH_3	1.38	0.55	0.04
Degree of esterification		60.1%	97.3%

3.3.2 FTIR

Figure 3.5 shows a comparison of the FTIR spectra of H20 with the two derivatized systems at room temperature. The antisymmetric methylene stretching peak at 2945 cm^{-1} (peak deconvolution is shown in the insets) was used for spectra normalization in this case as the concentration of these units remains unchanged during esterification reaction. It can be observed that after esterification, the intensity of vOH and vCO peaks was significantly reduced and enhanced respectively. The disappearance of vOH in H20-

CH3 also indicates the completion of the esterification reaction. Importantly, when comparing H20-50CH3 with H20, derivatization with acetyl chloride produced a minor blue-shift effect as compared to the effect of temperature but noticeably reduced the intensity of vOH peak practically all over the corresponding frequency range. The difference spectrum displayed in Figure 3.5 (C) shows no negative difference in this case as compared to the temperature effect. We believe that a decrease of vOH peak intensity can be in part due to a decrease in the number of hydroxyl groups as well as due to some weakening of hydrogen bond associations. Importantly, it seems derivatization, however, does not produce a large number of free (unbonded) hydroxyl groups. As the NMR results indicate that the remaining hydroxyl in H20-50CH3 is mainly linear hydroxyls, we believe that hydrogen bonding still exists in the system which is predominantly between hydroxyl hydrogens and the carbonyl oxygens. Note, the concentration of carbonyl groups greatly increases upon derivatization as one can clearly see on the FTIR difference spectrum (Figure 3.5 (C)).

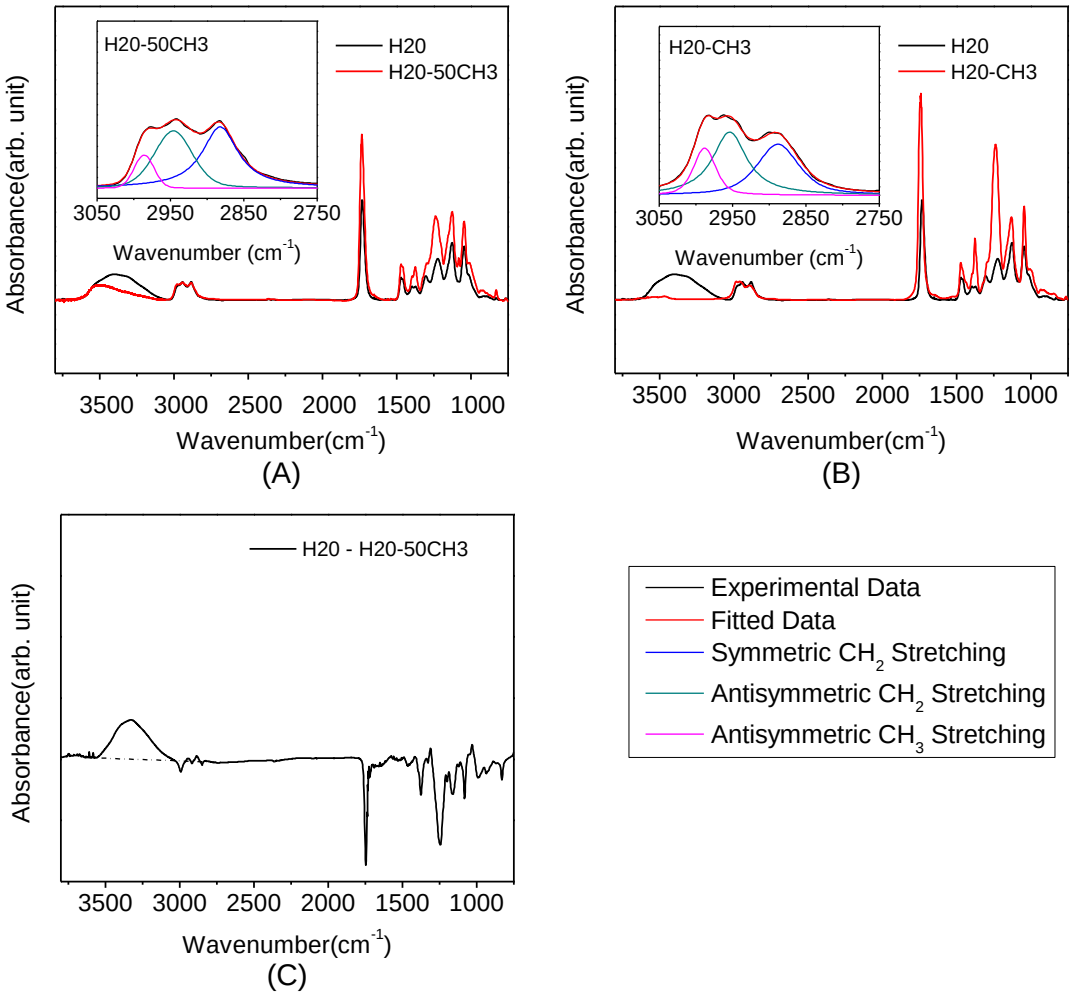

Figure 3.5 *Combined FTIR spectra of (A)H20-50CH3 and (B) H20-CH3 with H20, difference spectra obtained by subtraction of the spectra of H20-50CH3 from that of H20. The insets in (A) and (B) are the peak deconvolution of the methyl and methylene stretching peak of H20-50CH3 and H20-100CH3 respectively.*

3.3.3 DSC

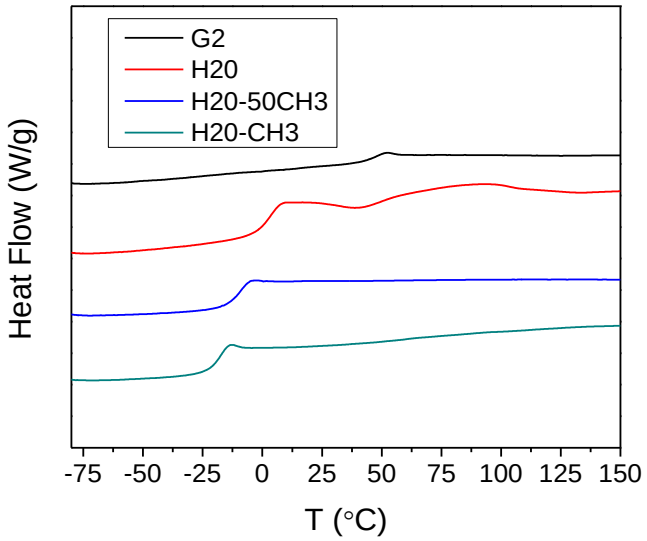

Figure 3.6 *DSC thermograms of G2, H20, H20-50CH3, and H20-CH3.*

It was informative to compare thermal transitions in H20-50CH3 and H20-CH3 systems with those in G2 and H20. The DSC curves of the four investigated systems are shown in Figure 3.6. Glass transition temperature, T_g, of G2, H20, H20-50CH3, and H20-CH3 was determined as 49°C, 4°C, -11°C and -18°C respectively. As discussed in the previous chapter, the lower T_g of H20 originates from its low M_w and broad M_w distribution resulting from the nature of the one-pot synthesis method.[3, 20] Lower T_g of the esterified systems as compared to H20 can be attributed to the reduction and the weakening of hydrogen bonding as reflected by the FTIR spectra.

Above T_g, like G2, both H20-50CH3 and H20-CH3 show no transitions, whereas H20 displays formation and melting peaks for the mesophase.[2, 21] This indicates that the formation of the mesophase in both H20-50CH3 and H20-CH3 has been disrupted.

3.3.4 Dielectric analysis

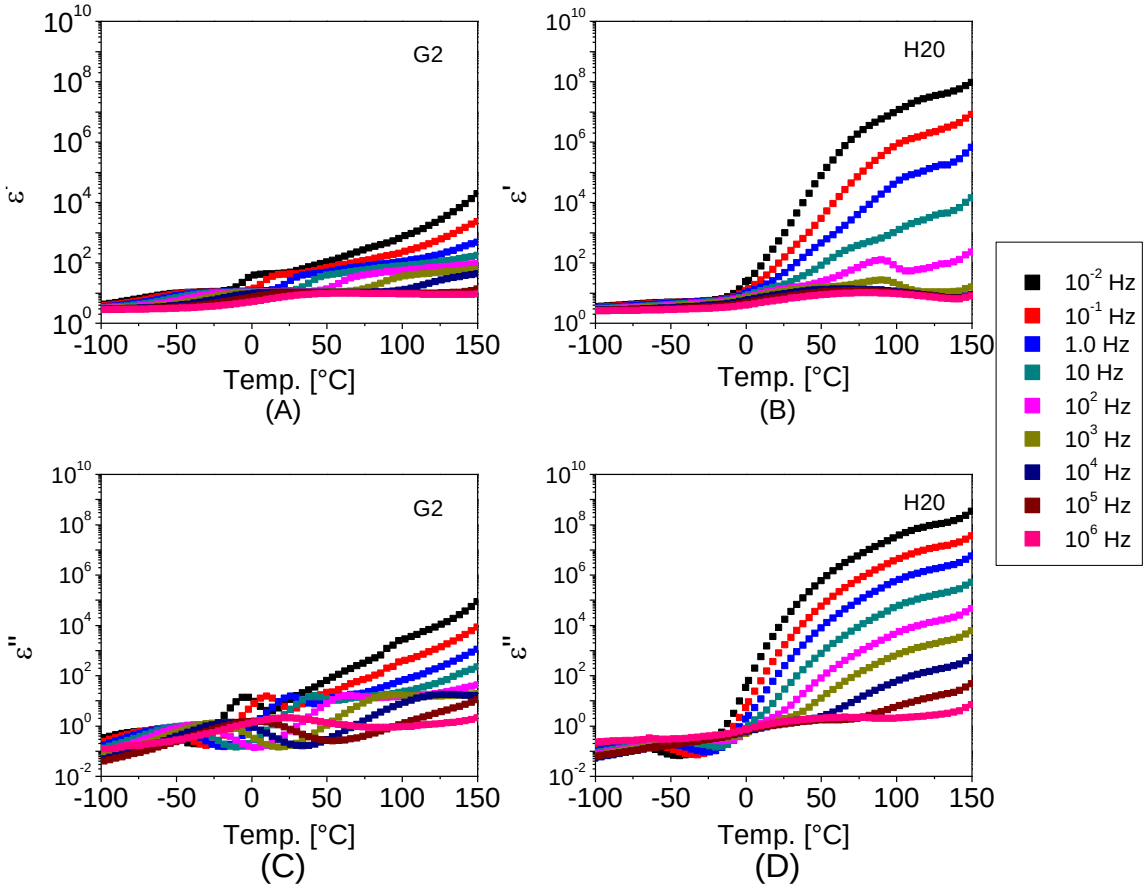

Figure 3.7 *The real part of complex dielectric permittivity of (A) G2 and (B) H20 and the imaginary part of complex dielectric permittivity of (C) G2 and (D) H20 against temperature under different frequencies.*

Figure 3.7 shows the real and imaginary part of the complex permittivity for H20 and G2, $\varepsilon'$and ε", as a function of temperature at frequencies from 0.1 to 10^6 Hz. One sub-T_g relaxation process was identified on ε" spectra of both G2 and H20 at similar low-temperature range. Relaxation peaks for H20 can be observed at -70~0°C at low frequencies whereas those for G2 can be observed at -70~30°C over the eight different frequencies. This relaxation process was identified as γ-relaxation and was ascribed to the

motions of hydroxyls according to the literature.[5-7] Above T_γ, another sub-T_g relaxation was observed on the ε" spectra of G2 and absent on that of H20. This relaxation will be discussed in the next chapter. At temperatures above T_g especially at low frequencies, both polymers exhibit abrupt increases of $\varepsilon'$and ε", which are due to the effect of electrode polarization and DC conductivity.[6, 7, 22]. Hence, the α-relaxation for both systems is masked.

Other than the relaxation, it can be found that both H20 and G2 exhibit very high dielectric constant values. For instance, at 20 °C and 1MHz where the effects of DC conductivity can be neglected, the ε' values of H20 and G2 are determined as 5.8 and 11.4, respectively. Comparing with common polymers, such as polyamide (PA), polycarbonate (PC), polypropylene (PP) and polyvinyl chloride (PVC), of which the ε' values are around 3 at similar conditions, those of G2 and H20 are considerably higher especially G2.[23-25] It should be noted that the high ε′values were detected on the plateau region right after γ-relaxation, hence we assume that high ε′values are related to the polarization involved in γ-relaxation. In addition, within the temperature range of γ-relaxation, the ε′ of H20 and G2 also exhibit strong frequency dependence, especially for G2. From 0.01Hz to 1MHz, ε' of G2 drops from ~10 to ~3, and that of H20 reduces from ~5 to ~3. The frequency dependence of ε' of both polymers is strong compared with common polymers, among which are not only just non-polar ones, such as PE and PP, but also polar ones such as polyethylene terephthalate (PET).[26-30] For instance, at 20°C, from the 100Hz to 1MHz, ε' of G2 drops from 10.7 to 7.5 whereas that of PET drops from 3.4 to 3 under similar conditions.[29, 30] As both the high value and strong frequency dependency of ε′ is correlated to the γ-relaxation in both systems, the dielectric spectra as

a function of frequency within the temperature range of γ-relaxation was carefully analyzed.

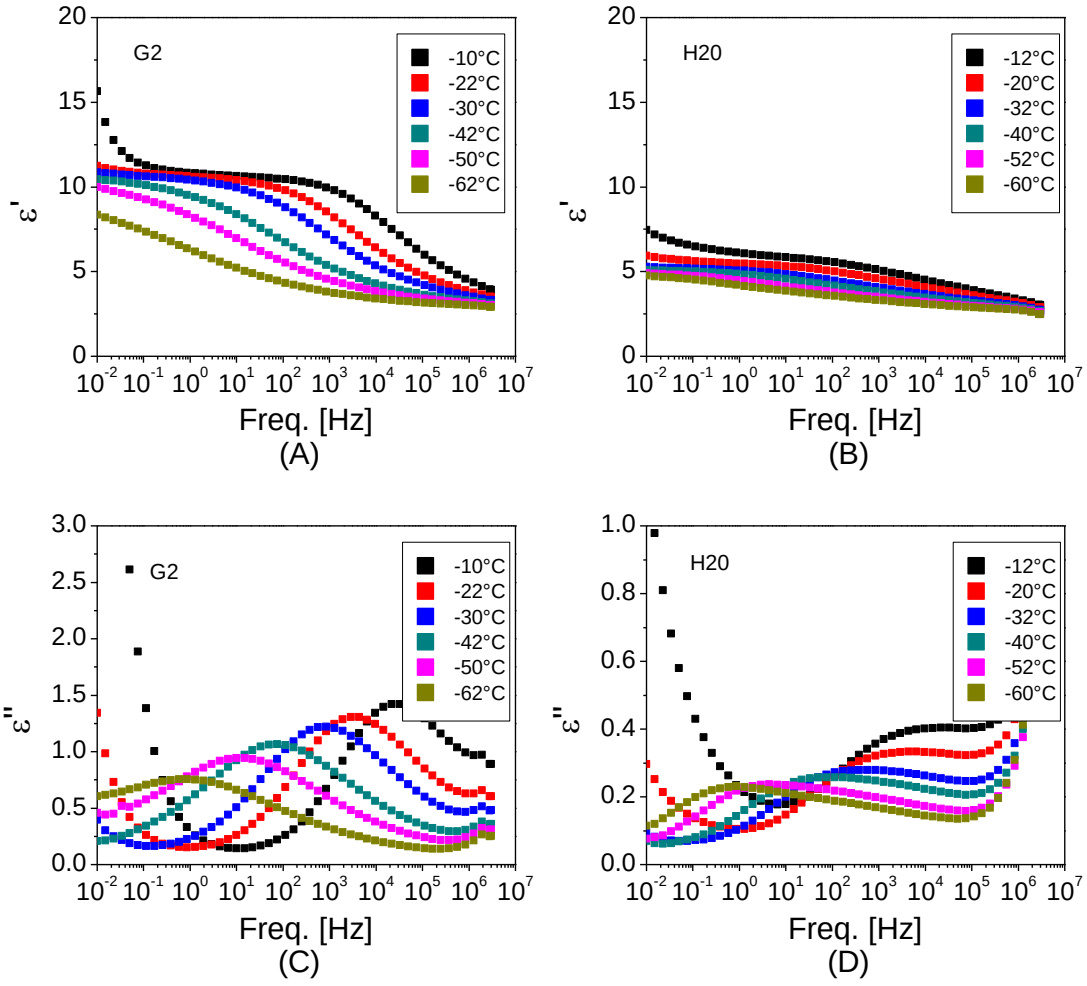

Figure 3.8 *Real ((A) and (B)) and imaginary ((C) (D)) parts of complex dielectric permittivity for G2 ((A) and (C)) and H20 ((B) and (D)) at temperatures between -60 and -10 °C.*

The real and imaginary parts of the complex permittivity for H20 and G2 as a function of frequency at temperatures from -60 to -10°C are shown in Figure 3.8. From the ε′ spectra of both systems, a plateau can be observed at low frequencies and beyond

the center point, the ε′ starts to decline with the frequency. At frequencies where ε′ starts declining, a peak starts to appear on the ε″ spectra. This confirms that high dielectric value and strong frequency dependency of ε′ is contributed by the γ-relaxation. To better analyze the γ-relaxation, the experimental data were fitted to the Havriliak-Negami (HN) equation in order to extract the dielectric constant value and the characteristic relaxation time at each temperature interval. [31, 32] The built-in HN equation of the WINFIT software by Novo-control is composed of a conductivity term and an HN term:

$$\varepsilon^* = \varepsilon' - i\varepsilon'' = -i\left(\frac{\sigma_{dc}}{\varepsilon_0 \omega}\right)^N + \sum_{k=1}^{3}\left[\frac{\Delta\varepsilon_k}{(1+(i\omega\tau_{HN})^{\alpha_k})^{\beta_k}} + \varepsilon_{uk}\right] \quad (24)$$

where the first term of the equation characterizes the conductivity effects. σ_{dc} is the DC conductivity and the exponent N reflects the degree of interconnectivity of charge hopping pathways.[33] $\varepsilon_0 = 8.854 \times 10^{-12}$ F·m^{-1}, which is the permittivity of the vacuum. $\omega = 2\pi f$, which is angular frequency. The other three terms account for the relaxation of dipole motion. For each term, $\Delta\varepsilon_k$ is the permittivity strength, which is defined by $\Delta\varepsilon_k = \varepsilon_{rk} - \varepsilon_{uk}$, where ε_{rk} and ε_{uk} are the ε' at relaxed (zero frequency) and unrelaxed state (infinity high frequency) respectively. α and β are parameters that describe the width and symmetry of the relaxation peak. [31] The Havriliak-Negami relaxation time, τ_{HN}, is related to the actual relaxation time, τ_{max}, which is determined by equation $\tau_{max} = \frac{1}{2\pi f_{max}}$, where f_{max} is the frequency at the loss peak maximum.

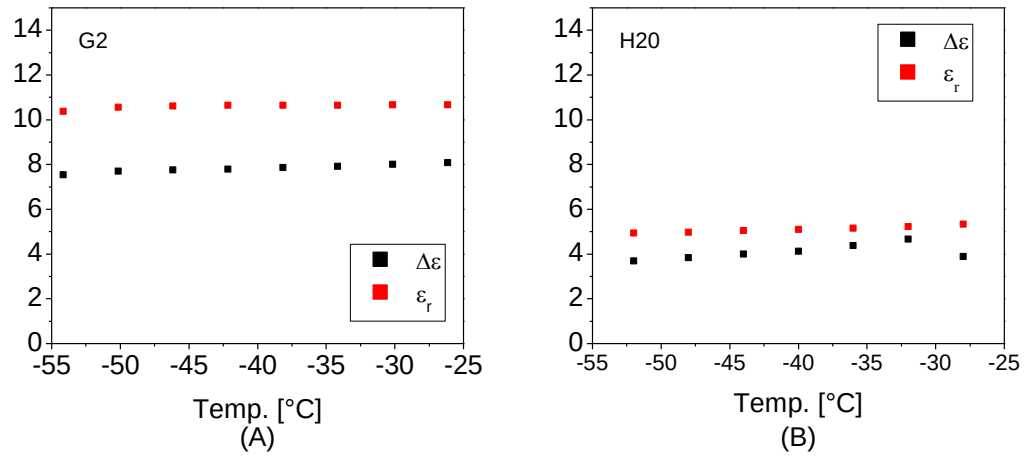

Figure 3.9 *Permittivity strength and the permittivity at the relaxed state of G2 and H20 at temperatures from -55 to -25 °C.*

Through HN analysis, $\Delta\varepsilon$ and ε_r of G2 and H20 for the γ-relaxation were determined and presented in Figure 3.9, where both values show little temperature dependence. The extracted $\Delta\varepsilon$ and ε_r for G2 approximately equal to 7.8 and 10.4 respectively and those for H20 are around 4.0 and 5.1 respectively. Those values agree well with our observation from Figure 3.9. As the γ-relaxation was ascribed to the hydroxyl motions, the high $\Delta\varepsilon$ value of both systems is correlated to the orientations of the hydroxyls. The $\Delta\varepsilon$ values of G2 and H20 are much higher than polymers containing dipoles with similar dipole moment as that of hydroxyls, which is 1.5 D.[34] For instance, the $\Delta\varepsilon$ values for secondary relaxation of PVC are around 0.7.[35] This suggests that the hydrogen bonds have a strong influence on the polarization of hydroxyls in the electric field.

The high $\Delta\varepsilon$ contributes to the high ε_r for both systems as ε_u comparably is low. Hence, we assume that the high dielectric constant of G2 and H20 is due to not only the

high concentration of hydroxyl groups but also the formation of hydrogen bonds. It was found that liquid systems of small protic molecules such as water and methanol, exhibit very high dielectric constant values at ambient conditions, which are around 80 and 30, respectively. [9, 36] Water molecules, for instance, being extensively H-bonded, respond to electric filed cooperatively in groups of about three rather than individually.[9] The association forms a larger dipole, which increases the dielectric constant. Not just small-molecule systems, linear hydroxylated polymer systems, such as polyethylene glycol (PEG) and polyvinyl alcohol (PVA), also display high dielectric constant values contributed by hydrogen bonding.[37-39] For instance, at ambient conditions, ε' of PVA are around 5, which is higher than that of other polar polymers.[40] In addition, it should be noted that the hydroxyl density per unit volume for PVA (27~30 mmol/cm^3) is much higher than those of H20 (12.3 mmol/cm^3) and G2 (13.5 mmol/cm^3), which suggests that hydroxyls in H20 and G2 are more associated via H-bonds than in PVA.

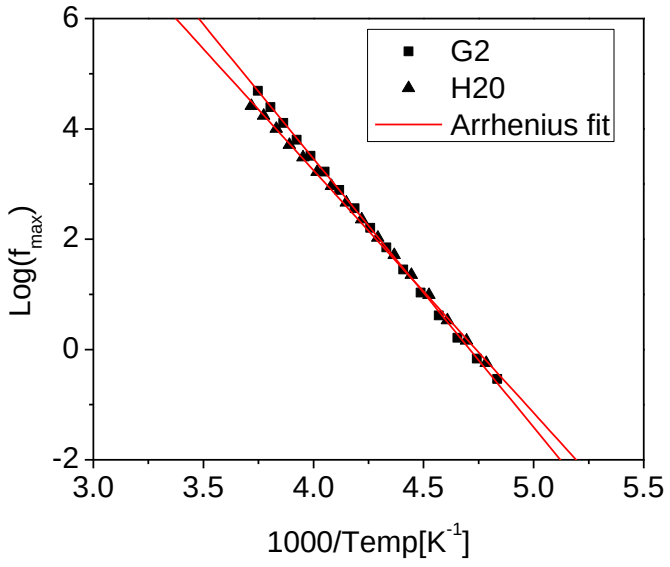

Figure 3.10 *Arrhenius plots for the γ-relaxation of G2 and H20.*

Figure 3.10 shows the temperature dependence of the f_{max} of γ-relaxation determined by NH analysis. f_{max} of γ-relaxation follows the Arrhenius dependence, which is defined as

$$f_{max} = f_0 \exp\left(\frac{E_a}{RT}\right). \quad (25)$$

where E_a is the activation energy of γ-relaxation. The E_a values of G2 and H20 were determined as 93.2 kJ/mol and 84.0 kJ/mol respectively, which are much lower than the reported one of H20, which is 139kJ/mol.[6] It has been neglected that, despite the same nomenclature of Hx0, there exist two different classes of Boltorn type HBPs: one contains PP50 as the core molecule, and one contains trimethylolpropane (TMP) core instead.[5-8] Listed in Table 3.2 are the comparison of T_g, T_γ, and E_a between the two Hx0 HBP systems, where HBPs containing TMP core are termed as Hx0-TMP, and those with PP50 core are termed as Hx0-PP50. The data reported by Androulaki etc. are not included here as the core molecules were not specified.[8] Regardless of the different testing methods, Hx0-TMPs exhibit higher T_g, T_γ, and E_a than Hx0-PP50s. Especially the E_a of Hx0-TMPs, which was determined in the range of 90 ~ 120 kJ/mole, was even higher than that of G2 despite their polydispersity and structural irregularity. As the OH number reported for H20-TMPs is similar to what we determined for H20-PP50, we anticipate that the differences in E_a values are mainly due to their different core structures. Since TMP is a simple trifunctional molecule of which size is smaller than tetrafunctional PP50, we assume that Hx0-TMPs are much smaller and more globular than Hx0-PP50s. Hence, Hx0-TMPs are more densely packed than Hx0-PP50s. Denser packing creates more constraints for motions of hydroxyls and hence increases the

activation energy. This hypothesis is supported by the higher T_g of Hx0-TMPs, which implies lower free volume content.

Table 3.2 *Comparison of T_γ, T_g and E_a between Hx0-TMPs and Hx0-PP50.*

Hx0-TMP Generation #	T_g (°C)	T_γ (°C)	E_a (kJ/mol)
2	30[6]	-58[6], -50[7]	139[6]
3	35[6]	-55[6], -62[7]	128[6], 106[7]
4	48[6],	-51[6], -57[7]	95[6], 90[7]
5	47[6]	-50.8[5],-52[6], -49[7]	94[5], 92[6], 98.8[7]
Hx0-PP50 Generation #	T_g (°C)	T_γ (°C)	E_a (kJ/mol)
2	4, 1[41]	-66	84
3	10[41]	-	-
4	22[41]	-	-

6Tg was determined by DMA at 1 Hz, Tγ was determined from M″ peak at 26Hz.

41Tg was determined by DSC.

7Tγ was determined from ε″ peak at 1 Hz.

Despite of the discrepancies with the experimental and the reported values, E_a values determined for both H20 and G2 are still much higher than those of common polymers such as Nylon 6, PP, polyimide, and PEEK, and even those of linear hydroxylated analogs such as polyvinyl alcohol (PVA) and polyally alcohol (PAA), which are around 60 kJ/mole.[42-47] This suggests constraints imposed by the hydrogen-bond network within the dendritic polymers is greater than linear systems. The pre-

exponential factor, τ_0, which is defined by $\tau_0 = \frac{1}{2\pi f_0}$, was determined for G2 and H20 as 1.84×10^{-24}s and 2.24×10^{-22}s respectively. Apparently, their pre-exponential factor τ_0 is much lower than the ideal value for Debye relaxation, which is ~10^{-13} s, especially for G2. [48, 49] The differences originate from the excess enthalpy and entropy involved in the relaxation, which suggests that the γ-relaxation of both H20 and G2 is an associative process. Therefore, we hypothesize that the γ-relaxation in H20 and G2 is corresponding to the associative motions of hydroxyls mediated via H-bonds. Higher E_a and lower τ_0 of G2 indicate that the hydroxyls in the system are more extensively bonded than those in H20. To prove our hypothesis, the dielectric properties of the esterified H20 were analyzed.

The complex permittivity for H20-50CH3 and H20-CH3 as a function of temperature at frequencies from 0.1 to 10^6 Hz are shown in Figure 3.11. A relaxation was observed on the dielectric spectra of H20-50CH3 and H20-CH3 at -10~40°C and -20~30°C respectively, which is ascribed to α-relaxation. Another relaxation was observed on H20-CH3, which is corresponding to electrode polarization. Like H20 and G2, abrupt increases of ε′ and ε″ was also observed for H20-50CH3 and H20-CH3 at above T_g. On the other hand, the existence of γ-relaxation can not be detected from Figure 3.11easily. Still, one can notice that the frequency dependence of ε′ of H20 at temperatures below T_g is significantly depressed after esterification.

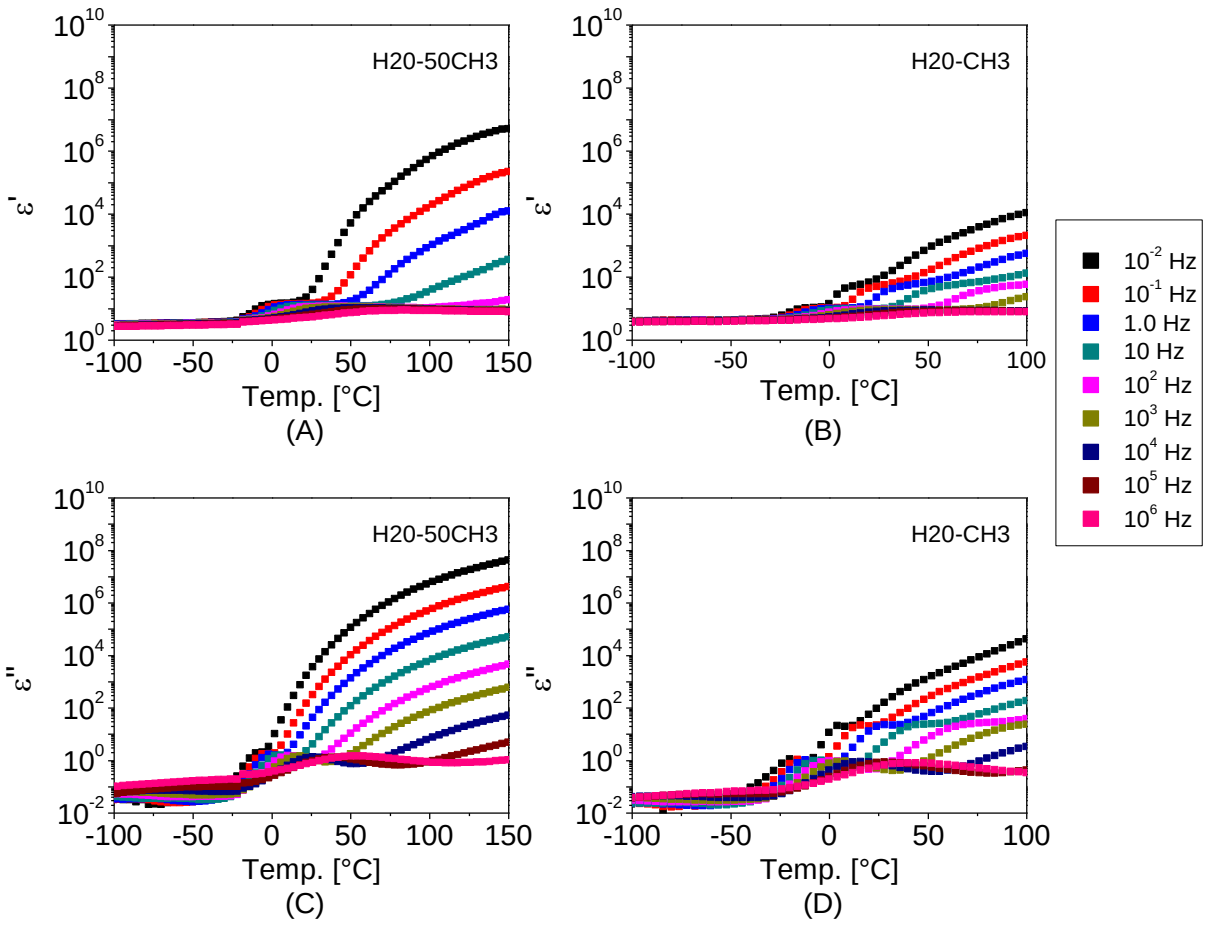

Figure 3.11 *Real ((A) and (B)) and imaginary part ((C) and (D)) of complex dielectric permittivity of H20-50CH3((A) and (C)) and H20-CH3((B) and (D)) against temperature under different frequencies.*

The γ-relaxation of H20-50CH3 and H20-CH3 was detected at a much lower temperature range, which is -70~-100°C. This indicates that the hydroxyl motions in the esterified system are less hindered and cause fewer energy losses. As shown in Figure 3.12, the intensity of the γ-relaxation peak is reduced by more than one order of magnitude for both esterified systems, specially H20-CH3, which confirms that the γ-relaxation in H20 is correlated to hydroxyls. The ε' values of H20-50CH3 and H20-CH3

were found at ~3.1 and ~4.2 respectively, which are slightly lower than that of H20. It should be noted that the dipole moment of ester groups, which is 1.8 D, is slightly higher than that of hydroxyl ones, which is 1.5 D. [34, 50] Hence, the reduction of dielectric constant in H20-50CH3, cannot be attributed to the reduction of the polarity of the system, but the disruption of the hydrogen bonding formation. H20-CH3 displays higher ε′ values than H20-50CH3 because of the effect of diminishing H-bonds is offset by increasing polarity. Therefore, it can be confirmed that high dielectric constant values of H20 and G2 are not just because of the high polarity of individual hydroxyls, but also due to the hydrogen bonds which increase dipole moment by forming associations.

The HN analysis was only performed on H20-50CH3 as the γ-relaxation of H20-CH3 can be barely resolved. Through HN analysis, the Δε for γ-relaxation of H20-50CH3 was determined as 0.8~1.3 which is considerably lower as compared to that of H20, which is around 4. Similar Δε reduction was also reported by Androulaki etc., where Δε of Boltorn HBPs was reduced from 2~6 to 0.2~0.9 when they were confined by hydrophilic sodium montmorillonite (MMT).[8] Though the hydroxyl density was unchanged, their capacity of forming hydrogen bonds was deteriorated due to spatial restriction imposed by the nanoplatelets. This also suggests that γ-relaxation of H20 and G2 are cooperative motions corresponding to hydrogen-bonded associations.

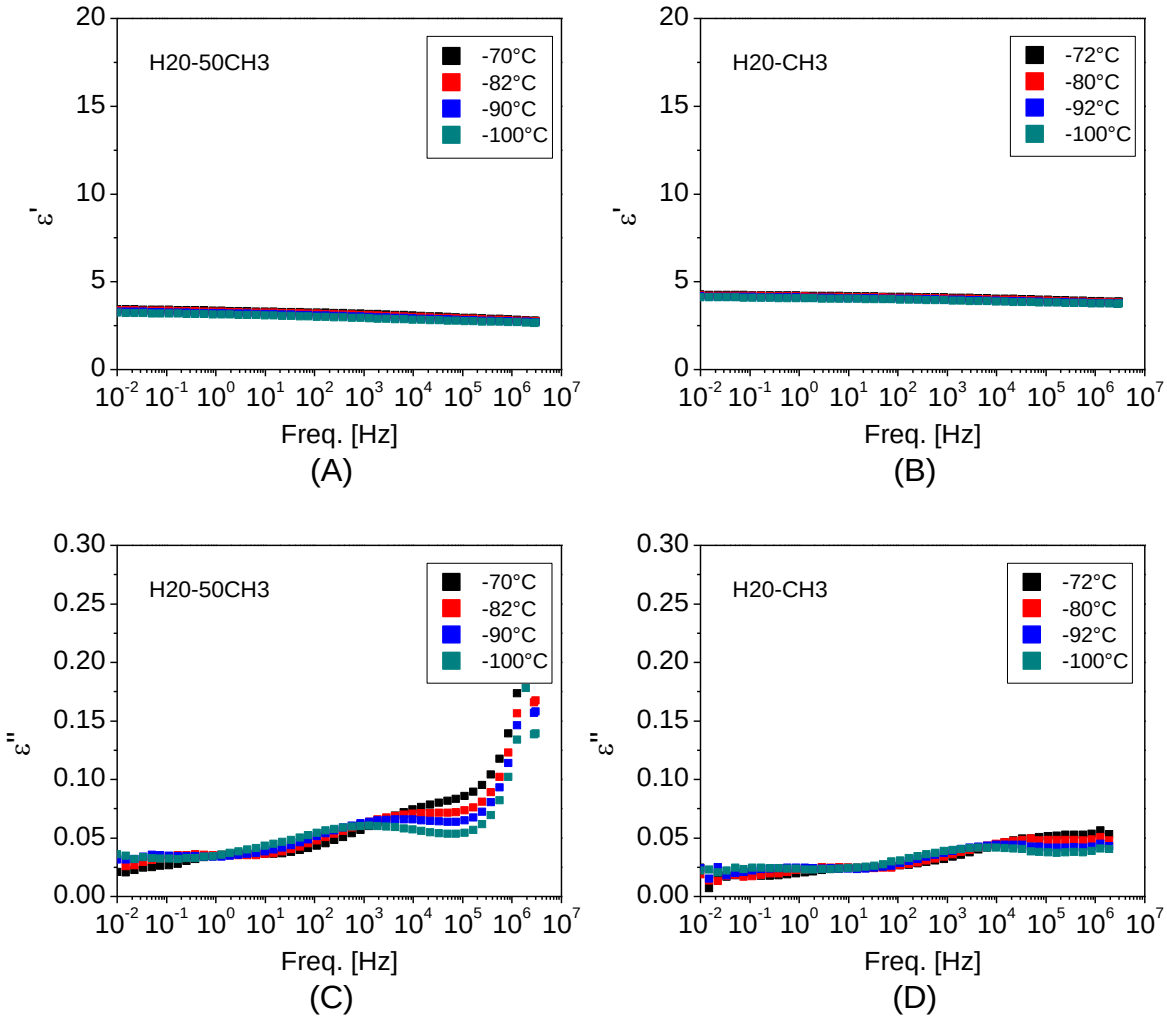

Figure 3.12 *Real ((A) and (B)) and imaginary part ((C) and (D)) of complex dielectric permittivity of H20-50CH3 ((A) and (C)) and H20-CH3 ((B) and (D)) against frequency at -70~-100°C.*

From the Arrhenius plot shown in Figure 3.13, E_a of the γ-relaxation of H20-50CH3 was determined as 34.3 kJ/mol. Comparing to the E_a of H20, which is 84.0 kJ/mol, the huge reduction in E_a after esterification indicates suggesting that the hindrance imposed on the related motion is depressed significantly. Meanwhile, the τ_0 of H20-50CH3, which was determined as 8.22×10^{-15}s, was found to be very close to that

of Debye relaxation, indicating the nature of the γ-relaxation shifted from associative to individual motions of hydroxyls upon esterification.

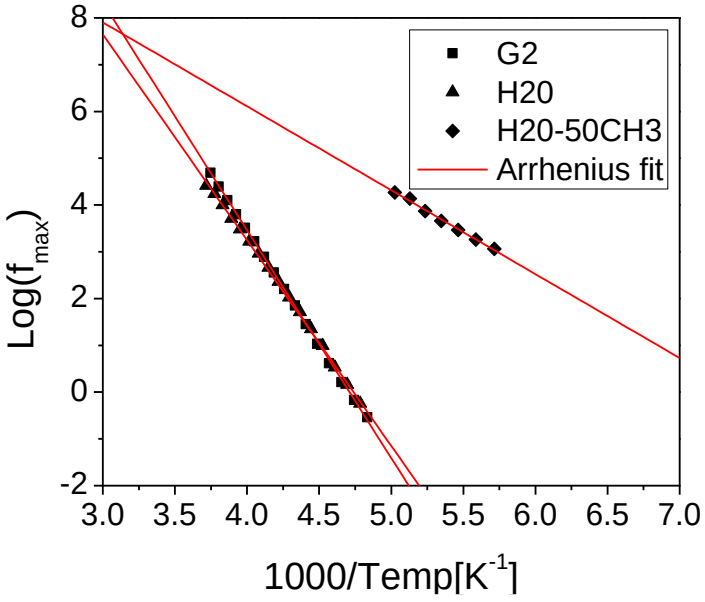

Figure 3.13 *Arrhenius plots for the γ-relaxation of H20, G2, and H20-50CH3*

So far, unique dielectric properties were found in G2 and H20, including high dielectric constant, high permittivity strength, high activation energy, and the non-Debye behavior of γ-relaxation. These features can all be attributed to the association formed between hydroxyls via hydrogen bonds. Considering the complete diminishment of these features in H20-50CH3, of which the existence of hydrogen bonding was proved by FTIR and DSC, we assume that the association cannot be formed by single H-bond. Additionally, since these features were not observed from the linear hydroxylated polymers, we hypothesize a unique hydrogen bonding association is formed within the dendritic polymers contributed by their branching structures, i.e. the chain-like hydrogen-bonded clusters.

3.3.5 MD simulation

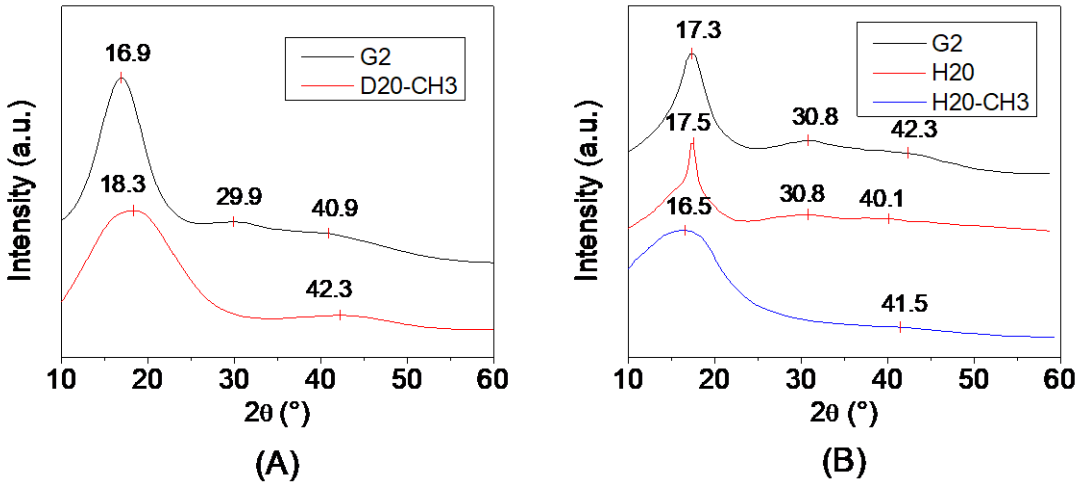

Figure 3.14 *WAXS intensity patterns (A) predicted from the final MD simulated structures of G2 and 100% esterified G2, G2-CH3 and (B) collected experimentally from G2, Boltorn™ H20, and 100% esterified H20, H20-CH3.*

MD simulations were conducted to analyze the hydrogen bonding association and visualize the structures of H20 and G2. To decouple the effects of core structure from those of branching regularity, the corresponding dendrimer of H20, D20, was also studied. The appropriateness of simulation was verified by comparing the final density of each system with the experiment values. The simulated densities agree well with the experimental data. Specifically, the simulated density of H20, 1.261 g/cm^3, is only by 1.8% lower than the experimental density of H20, 1.284 g/cm^3; the simulated density of D20, 1.248 g/cm^3, is by 2.8% lower than the experimental density of H20, 1.284 g/cm^3; the simulated density of G2, 1.278 g/cm^3, is by 2.2% lower than the experimental density of G2, 1.307 g/cm^3.

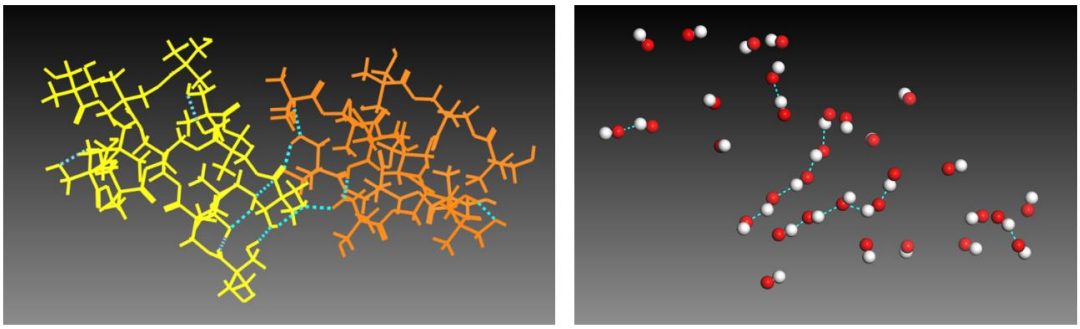

(A) (B)

Figure 3.15 *Two different visualizations of the hydrogen-bonded clusters within two G2 dendrimer molecules, where the blue dashed lines represent the hydrogen bonds. (A) shows two molecular structures in yellow and brown. (B) only shows the hydroxyl oxygen and hydrogen atoms in the two molecules, which are presented by red and white balls respectively.*

To confirm the existence of the hydrogen-bonded clusters in the G2, the X-ray scattering patterns of G2 and G2-CH3 systems were first simulated. As shown in Figure 3.14 (A), an intense reflection at $2\theta \approx 17°$ as well as two smaller and broader reflections at $2\theta \approx 30°$ and 41° were observed on the simulated X-ray patterns of G2. On the other hand, G2-CH3, displays only two peaks, one at $2\theta \approx 17°$ and one at 42°, whereas the peak at $2\theta \approx 30°$ disappears. Hence, the peak at $2\theta \approx 30°$ is corresponding to the ordering of hydroxyls, which is due to the formation of H-bonded clusters as revealed by our previous research.[2]

The simulated pattern for G2 looked virtually identical to the experiment one shown in Figure 3.14 (B). The WAXS pattern of H20 was also similar to that of G2 except for the intense peak at $2\theta \approx 17°$, which originated from the ordering of the mesophase into formed linear segments.[2] The absence of the $2\theta \approx 30°$ peak was also observed on the WAXS pattern of the H20-CH3, which again, confirms that the structural

origin of the reflection peak is specifically related to the hydroxyl end-groups. Both simulated and experimental X-ray scattering support that the H-bonded clusters exist in the G2 system.

Materials Studio program (Accelrys Software, Inc.: San Diego) was used for the preliminary visual assessment for the hydrogen-bonded clusters in G2. Shown in Figure 3.15 (A) are two G2 molecules randomly picked from the amorphous cell of the final G2 file. Hydrogen bonds, represented by dashed blue lines, were observed within and between the molecules and some of them are connected and form a string. The same structures are presented in a different form in Figure 3.15 (B), where all atoms were hidden except the hydroxyl oxygen and hydrogen atoms which are represented by red and white balls. From Figure 3.15 (B), not only single O-H···O groups but also assemblies containing multiple consecutive O-H···O groups were observed. The assemblies are the H-bonded chain-like clusters according to our previous simulation work on bis-MPA dendritic polymers. Since these two molecules were randomly picked out from 50 molecules in the amorphous cell, we assume that these clusters are abundant in the G2 system.

To further investigate the formation of the H-bonded chain-like clusters, a more thorough analysis was conducted using a custom-made program 'TracedHbonds'. Every H-bond, chain-like cluster, and force field of every proton acceptor was traced via 'TraceHbonds'. This allows us to calculate the average number of H-bonds and chain-like clusters of different lengths, and identify the contributions of oxygen atoms from hydroxyl, carbonyl, ester, and ether groups to H-bond formation. For ease of comparison, the single O-H···O was also considered as a chain-like cluster with chain length equals to

1. Figure 3.16 shows all chain-like clusters of O-H···O groups traced by the 'TracedHbonds' program in the final amorphous cell of G2 plotted in a 3-D system of coordinates. Three rotational views are conveniently displayed to help the reader. To better visualize the clusters, each cluster is represented by a hemisphere capped tube, with spline interpolation between adjacent hydrogen and oxygen atoms within the same cluster. To guide the eye, the diameter of the tubes is set at an arbitrary value. Clusters are colored by a gradient, blue to red, representing short to long lengths. In this very revealing 3-D representation, the clusters appeared as a crowded group of randomly oriented worm-like objects. Most of them are short, approximately 1 to 3 hydrogen bonds in length, but longer associations of 4-8 hydrogen bonds can also be clearly observed.

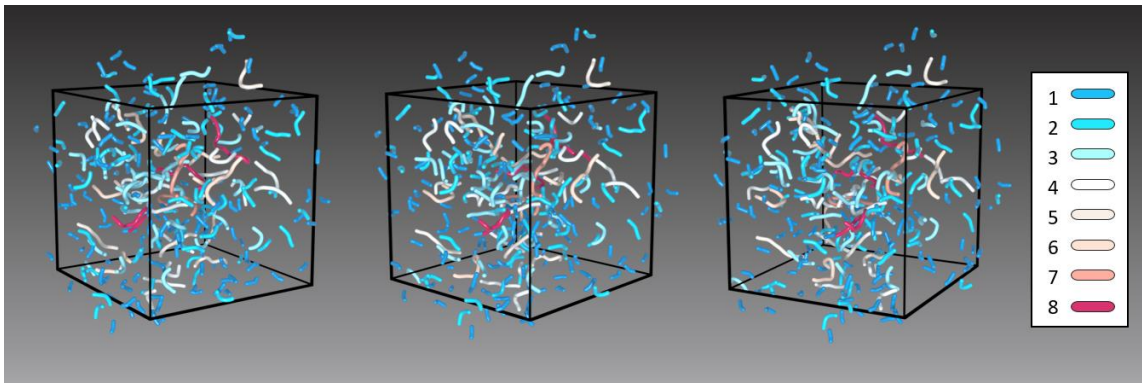

Figure 3.16 *Three-dimensional view of "chain-like-clusters" in the final relaxed amorphous cell of G2. Three rotated views of the amorphous cell are shown. Each cluster is represented by a hemisphere capped tube, with spline interpolation between adjacent atoms within the same cluster and diameter set at an arbitrary value to guide the eye. Clusters are colored by a gradient, blue to red, representing short to long lengths.*

To compare the formation of the H-boned cluster between G2, H20, and D20, a statistical analysis was performed on the 1000 frames of the final trajectory file of each

system, where the average total numbers of clusters per system were calculated as 315, 292, 278 respectively. The number distribution of clusters of different lengths in G2, H20, and D20 system was shown in Figure 3.17 (A), (B) and (C) respectively. All three systems exhibit a similar exponential decreasing trend of cluster number with increasing cluster length. H20 shows the highest number of clusters composed of single H-bond, 184, and D20 and G2 show lower number, 147. G2 displays the longest maximum chain length, 17, followed by H20, 13, and D20, 12. The fraction of clusters for each cluster length is shown in Figure 3.17(D). In each G2, H20, and D20 system, about 50~60% of clusters are composed of one H-bond and 40~50% are composed of two or more H-bonds, contributing to an average cluster length of approximately two H-bonds. The order of decreasing fraction of clusters composed of one H-bond is: H20 (55.0%) > G2 (52.6%) > D20 (50.2%), while the order of decreasing average chain length is in reverse: D20 (2.01 ± 0.04) > G2 (1.98 ± 0.04) > H20 (1.72 ± 0.04).

The effect of the core molecule on the formation of H-bonded clusters can be revealed via the comparison between G2 with D20. The fractions of clusters composed of more than 9 H-bonds were higher in G2. In addition, G2 was able to form, though low in concentration, extra-long clusters (contain more 13 H-bonds) which were absent in D20. Hence, despite the fractions of clusters composed of one H-bond is higher in G2, the average cluster lengths of both systems are almost the same. Therefore, the overall effect of the core structure on H-bonded cluster formation is not very strong, though smaller core favors the formation of very long clusters.

The effect of structural irregularity on H-bond clustering was assessed by comparing H20 with D20. H20 exhibits a higher fraction of the single-bond cluster and

the fraction curve decays faster with respect to increasing length of clusters. Hence, the average cluster length of H20 is apparently lower than that of D20. Therefore, structure irregularity has a negative effect on forming longer clusters.

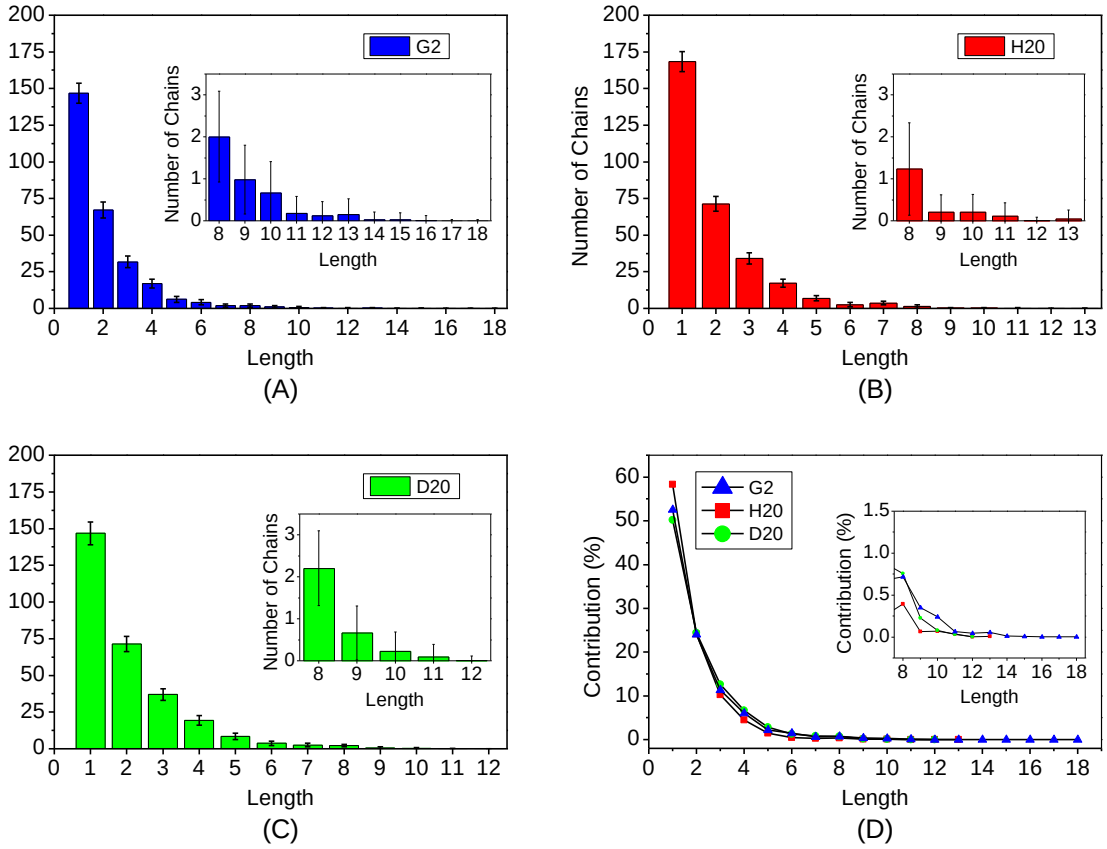

Figure 3.17 *Number distribution of chain-like clusters for each length for (A) G2, (B) H20, and (C) D20. (D) the fraction of chain-like clusters for each length. The corresponding insets display a zoomed-in view for clusters of a chain length of equal to or more than 8 hydrogen bonds.*

To reveal how structural regularity affects the clustering formation, the contributions of oxygens from different functional groups to H-bond formation were also analyzed and results are listed in Table 3.3. Of the 3 systems, hydroxyl oxygens are the predominant proton acceptors, which contributes to about 60% H-bonds, followed by

carbonyl oxygen, which contributes about 30%. Ester and ether oxygens, on the other hand, contribute only about 3%, or even lower.

H20 shows about 10% lower contribution from hydroxyl oxygens and 3% higher contribution from carbonyl oxygens as compared to D20, which indicates that decreasing the degree of branching significantly reduces the portion OH···OH bonds and slightly increases that of OH···O=C bonds in dendritic polymers. Comparing G2 with D20, its contribution of hydroxyl oxygens is about 3% higher whereas that of carbonyl oxygens is about the same as D20, which suggests that a more globular structure will further increase the preference of forming OH···OH bonds.

Table 3.3 *Participation of different oxygen 'acceptors' in hydrogen bond formation*

	Contribution to Clusters				**Total**
	Hydroxyl	**Carbonyl**	**Ester**	**Ether**	**Number of H-bonds**
G2	385 (69.8%)	163 (29.5%)	3 (0.6%)	-	552
H20	331 (56.4%)	179 (32.5%)	18(3.0%)	22 (3.8%)	551
D20	390 (66.4%)	174 (29.7%)	3 (0.4%)	20 (3.5%)	587

Note: Percentage was calculated from the total number of hydrogen bonds.

Comparing H20 with G2, H20 shows a considerably lower fraction of OH···OH and a higher proportion of OH···O=C bonds, which agrees well with our FTIR results. This explains why higher fractions of long clusters were found in regular systems. Since hydroxyl groups contain both proton donor and acceptor, they can be positioned either at

the center or the end of each cluster. On the contrary, carbonyl, ester and ether groups which only serve as proton accepter, could only be located at the end of each cluster. Thus, a higher propensity for forming H-bonds with hydroxyl oxygens increases the probability of forming a long cluster in dendrimer systems, whereas higher tendency of forming H-bonds with carbonyl, ester and ether oxygens decreases the probability of forming longer clusters in H20.

To analyze how molecular structure affects the hydrogen bonding and cluster formation, the molecular structure was visualized and analyzed using Materials Studio program. Three approximately orthogonal views of a representative molecule from the final amorphous cells of H20, D20 and G2 are shown in Figure 3.18. As expected, G2 exhibits a more compact, sphere-like structure, and the remaining two systems clearly displayed more stretched pancake-like structures. The structural asymmetry of both H20 and D20 was inherited from the PP50 core, which allows their final structures to be more stretched along the direction of the more extended ethoxylated arm. H20 was more unevenly stretched, due to its irregular branching structure which somehow intensified this asymmetry. Accordingly, H20 is the largest in size, $R_g = 8.7 \pm 0.5$ Å, followed by D20, $R_g = 8.2 \pm 0.1$ Å, and G2, $R_g = 6.7 \pm 0.2$ Å.

The spatial distribution of the end-groups, which are highlighted in yellow, was also investigated. For D20 and G2, all the terminal hydroxyls were found to be positioned at the periphery of the molecules. However, for H20, most of its end-groups gathered on the surface, some linear hydroxyls can still be detected within the molecule, which are circled in Figure 3.18. This supports our argument that structural irregularity strongly affects the preference of forming OH···O=C and OH···OH H-bonds in dendritic polymer

systems. For dendrimer systems, with all hydroxyls gathering on the surface, hydroxyls have higher chances of interacting with each other and hence increase the probability of forming O-H···O-H bonds. On the other hand, for H20, with hydroxyls being more evenly distributed within the structure, chances for terminal hydroxyls interacting with carbonyl, ester, and ether groups are increased, which decreases probability O-H···O-H bonds.

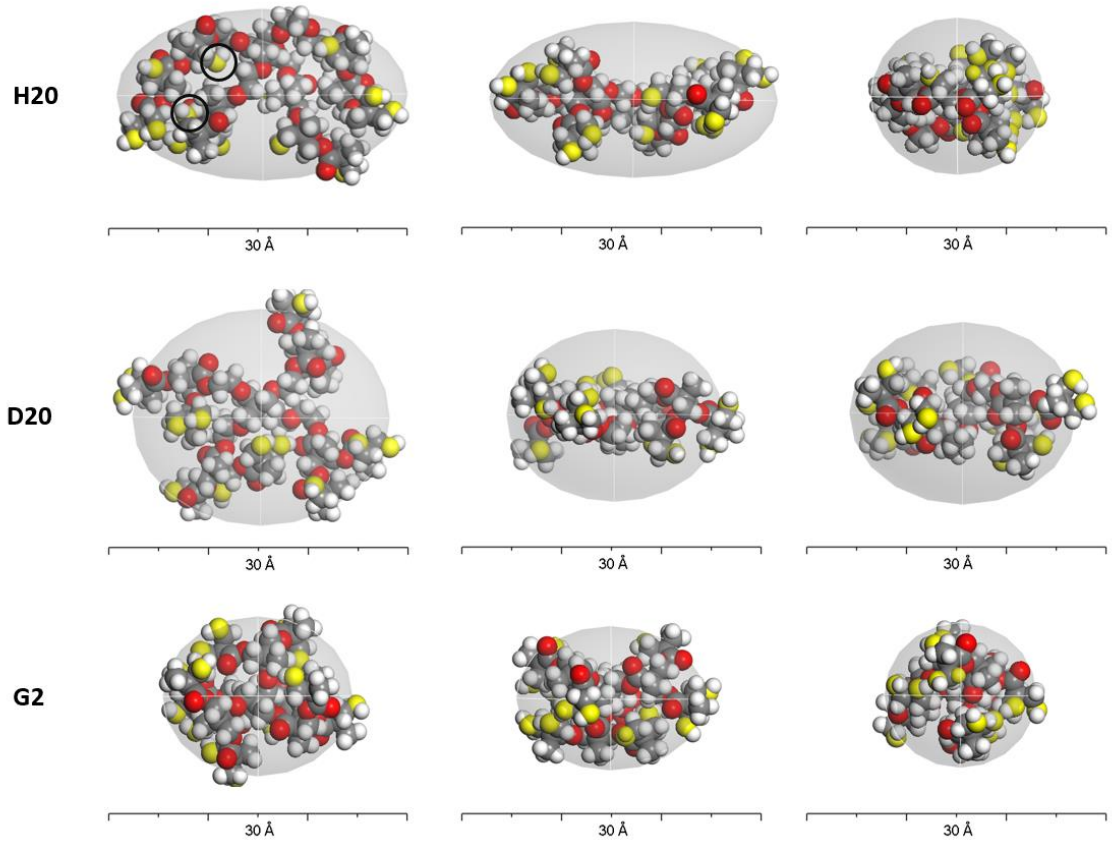

Figure 3.18 *Top, front, and right views of a representative molecule extracted from the final amorphous cell of H20, D20, and G2. The terminal hydroxyl oxygen atoms are highlighted in yellow.*

The pair correlation function between the center carbon atoms and hydroxyl oxygen atoms, $g(r)_{c\text{-}o}$, was calculated for each dendritic polymer system to analyze the

effect of molecular structure on the spatial arrangement of hydroxyls. As shown in Figure 3.19, the $g(r)_{c\text{-}o}$ functions of all 3 systems equal to 0 at r < 3.5Å, then the function starts to increase and reached a peak value at round r=8Å, and finally decays to 0. Comparing the position of the peak and the calculated R_g values, we can conclude that hydroxyls all positioned close to the molecular boundaries. The peak of G2 is higher and narrower as compared to H20 and D20, which indicates that the local concentration of hydroxyls within G2 is higher than H20 and D20. This explains why G2 displays a higher fraction of O-H···O-H bonds as compared to D20 and its capability of forming an extra-long H-boned cluster.

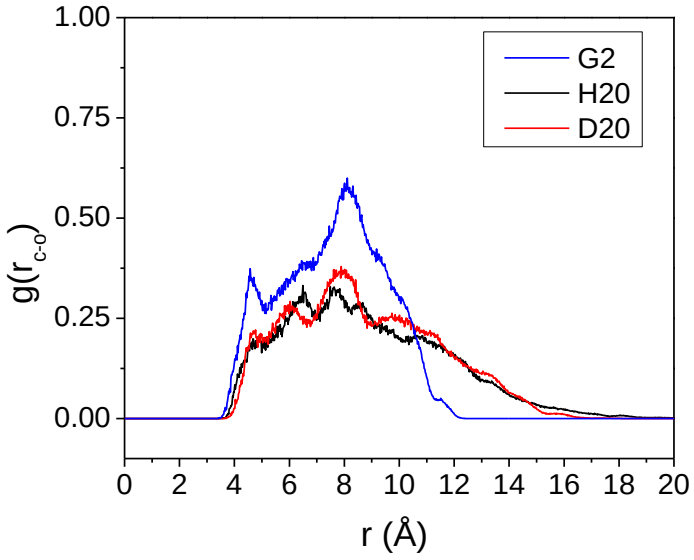

Figure 3.19 *The intramolecular pair correlation function between the center carbon atoms and the hydroxyl oxygen atoms calculated for G2, H20, and D20.*

The spatial arrangements of hydroxyls within H20 and D20 are very similar though D20 does show a slightly narrower distribution. Hence, it raises a question of what causes such a huge difference in terms of H-bond formation. It can be explained by

the formation of intra-unit H-bonds within the same bis-MPA terminal unit. Though hydroxyls in both polymers are widely distributed in a similar pattern, hydroxyls in D20 are able to form H-bonds with the hydroxyl next to it within the same terminal unit whereas those in H20 are not as likely as most of the hydroxyls are from the linear units. Therefore, with a considerably reduced portion of intra-unit H-bonds, H20 has a lower fraction of O-H···O-H bonds.

To sum up, the formation of chain-like H-bonded clusters explains unique dielectric properties of H20 and G2 perfectly, including the high dielectric constant values, and non-Debye nature of γ-relaxation. With all polar groups oriented in the same direction within the chain, the chain-like clusters are like larger dipoles, leading to high ε'. When the frequency is low, the dipoles within the same cluster rotate cooperatively with breaking and reforming H-bonds, which gives rise to the high E_a and the non-Debye τ_0 values. As frequency increases, leaving no time for H-bonds to reform, dipoles start losing their orientation. This leads to a large reduction of dielectric constant at a relaxed state and hence, high $\Delta\varepsilon$.

The higher average cluster length of G2 coincides with its higher dielectric constant and more associative dielectric behavior of the γ-relaxation. It should be noted that as the hydroxyl concentration for H20 and G2 are very close, so their dielectric properties are mainly determined by the capability of forming long H-bonded clusters.

3.4 Conclusion

The dielectric properties of H20 and G2, as well as the nature of γ-relaxation, was investigated thoroughly via dielectric spectroscopy and MD simulation. High dielectric

constant and permittivity strength was found for both G2 and H20, especially G2. Since the hydroxyl concentration of G2 and H20 are very close, higher ε' and $\Delta\varepsilon$ values of G2 were ascribed to the associations formed by hydroxyl via H-bonds. High activation energy and the low preexponential factor were determined for the γ-relaxation for both polymers, indicating that the relaxation is non-Debye, which is corresponding to associative motions of hydroxyls rather than localized motions.

Then dielectric analysis was conducted on partially and fully esterified H20, which named H20-50CH3 and H20-CH3 respectively. Before that, the actual degree of esterification for H20-50CH3 and H20-CH3 was determined via NMR as 60% and 97% respectively. Through FTIR, the existence of hydrogen bonding in H20-50CH3 can still be detected. No hydrogen bonding was found in H20-CH3. T_g of H20-50CH3 and H20-CH3 was determined as -11°C and -18°C, which is significantly lower than that of H20, due to the reduction of hydrogen bonding.

The dielectric data of both polymers shows lower dielectric constant and much lower permittivity strength as compared to H20 as the formation of hydrogen bonding association was disrupted. The γ-relaxation was shifted to a much lower temperature range. The γ-relaxation of H20-CH3 was barely detected which confirms that the γ-relaxation is correlated to hydroxyl motions. Through the Arrhenius analysis of the γ-relaxation of H20-50CH3, the E_a value was found to be significantly reduced as compared to H20. Meanwhile, a huge increase was discovered in τ_0, which became close to the ideal Debye value. Considering the complete diminishment of the non-Debye relaxation features in H20-50CH3, where hydrogen bond still exists, we assume that the association cannot be formed by single H-bond. Therefore, the high dielectric constant

and the non-Debye nature of γ-relaxation of G2 and H20 was ascribed to the formation of a unique association of OHs via multiple H-bonds within the dendritic polymers, i.e. the chain-like hydrogen-bonded clusters.

MD simulation was performed to analyze molecular structure and its effects on the H-bond and H-bonded cluster formation of G2 and H20. The existence of the H-bonded cluster in G2 was firstly confirmed via the reflection peak at 2θ≈30° on simulated and experimental X-ray scattering patterns. In a visualization of the H-bonded clusters in G2, clusters with different lengths from 1 to 8 were visable. Then the H-bonded cluster formation in G2 and H20 was analyzed and compared. To decouple the effects of core structure from those of branching regularity, the corresponding dendrimer of H20, D20, was also studied. Through a statistical H-bond analysis over 1000 frames of the final structures, in all the three systems, about 50~60% of clusters were composed of one H-bond and the rest 40~50% were composed of two or more H-bonds. The order of decreasing fraction of clusters composed of one H-bond is: H20 (58.4%) > G2 (52.6%) > D20 (50.2%). The core structure does not have a very strong effect on H-bonded cluster formation, though the smaller core shows the capability of forming very long clusters. Structure irregularity suppressed the formation of long clusters. The contributions of oxygens from different functional groups to H-bond formation were also analyzed. Of the 3 systems, hydroxyl oxygens are the predominant proton acceptors. H20 displays a lower and higher fraction of OH···OH and OH···O=C respectively as compared to G2, which agrees well with our FTIR results. A higher fraction of OH···OH in dendrimer systems increases the probability of forming a long cluster as only hydroxyl groups can be positioned either at the center or the end of each cluster.

Finally, the molecular structures of the 3 systems were analyzed. As expected, the simulated G2 exhibits a more compact, sphere-like structure, and both D20 and H20 clearly displayed more stretched, pancake-like structures, which were inherited from the core. Only hydroxyls in H20 were found to be positioned both within the molecule and at the surface. This explains why H20 showed a higher tendency of forming OH···O=C as the hydroxyl groups within the molecule have higher chances of interacting with carbonyl groups. The spatial distribution of the end-groups within the molecule was also investigated via pair correlation function. It was revealed that OHs of the 3 systems all gathered at the proximity of the molecular boundaries, with G2 showing a more concentrated distribution due to its smaller and globular molecular structure. This explains the higher fraction of OH···OH bonds in G2 as compared to D20 and its capability of forming extra-long clusters. H20 and D20 show similar spatial arrangement of OHs, suggesting that structural irregularity mainly reduces the capability of forming intra-unit H-bonds in dendritic polymers.

To correlate our finding of H-bonded clusters with the dielectric results, we conclude that the unique dielectric properties of H20 and G2, such as high ε', $\Delta\varepsilon$ and Ea values, and non-Debye τ_0 values, is originated from the H-bonded chain-like clusters.

3.5 References

1. Tanis, I.; Karatasos, K., Local dynamics and hydrogen bonding in hyperbranched aliphatic polyesters. *Macromolecules* **2009,** *42* (24), 9581-9591.
2. Syed, M. N. Hydrogen Bond-Mediated Structural Order in Hydroxylated Bis-MPA Dendritic Polymers: Experimental and Molecular Dynamics Simulation Study. Ph.D. Thesis, The University of Southern Mississippi, 2015.
3. Žagar, E.; Žigon, M., Aliphatic hyperbranched polyesters based on 2, 2-bis (methylol) propionic acid-Determination of structure, solution and bulk properties. *Prog. Polym. Sci.* **2011,** *36* (1), 53-88.
4. Komber, H.; Ziemer, A.; Voit, B., Etherification as Side Reaction in the Hyperbranched Polycondensation of 2,2-Bis(hydroxymethyl)propionic Acid. *Macromolecules* **2002,** *35* (9), 3514-3519.
5. Malmström, E.; Liu, F.; Boyd, R.; Hult, A.; Gedde, U., Relaxation processes in hyperbranched polyesters. *Polym. Bull.* **1994,** *32* (5-6), 679-685.
6. Zhu, P. W.; Zheng, S.; Simon, G., Dielectric relaxations in a hyperbranched polyester with terminal hydroxyl groups: effects of generation number. *Macromol. Chem. Phys.* **2001,** *202* (15), 3008-3017.
7. Turky, G.; Shaaban, S. S.; Schoenhals, A., Broadband Dielectric Spectroscopy On the Molecular Dynamics in Different Generations of Hyperbranched Polyester. *J. Appl. Polym. Sci.* **2009,** *113* (4), 2477-2484.
8. Androulaki, K.; Chrissopoulou, K.; Prevosto, D.; Labardi, M.; Anastasiadis, S. H., Dynamics of hyperbranched polymers under confinement: a dielectric relaxation study. *ACS Appl. Mater. Inter.* **2015,** *7* (23), 12387-12398.

9. Sharp, K. A., Water: structure and properties. *Encyclopedia of life sciences* **2001,** *10*.
10. Stillinger, F. H., Low-Frequency Dielectric Properties of Liquid and Solid Water. *The Liquid State of Matter: Fluids, Simple and Complex* **1982**, 341-431.
11. Hölter, D.; Burgath, A.; Frey, H., Degree of branching in hyperbranched polymers. *Acta Polym.* **1997,** *48* (1-2), 30-35.
12. Žagar, E.; Huskić, M.; Žigon, M., Structure-to-Properties Relationship of Aliphatic Hyperbranched Polyesters. *Macromol. Chem. Phys.* **2007,** *208* (13), 1379-1387.
13. Ihre, H.; Padilla De Jesús, O. L.; Fréchet, J. M., Fast and convenient divergent synthesis of aliphatic ester dendrimers by anhydride coupling. *J. Am. Chem. Soc.* **2001,** *123* (25), 5908-5917.
14. Elmahdy, M. M.; Chrissopoulou, K.; Afratis, A.; Floudas, G.; Anastasiadis, S. H., Effect of Confinement on Polymer Segmental Motion and Ion Mobility in PEO/Layered Silicate Nanocomposites. *Macromolecules* **2006,** *39* (16), 5170-5173.
15. Malmström, E.; Johansson, M.; Hult, A., The effect of terminal alkyl chains on hyperbranched polyesters based on 2, 2-bis (hydroxymethyl) propionic acid. *Macromol. Chem. Phys.* **1996,** *197* (10), 3199-3207.
16. Accelrys Software Inc. *Theory: Classical simulation theory: Calculating properties: Radius of gyration. In Materials Studio Online Help*, Accelrys Software, Inc.: San Diego, 2014.
17. Accelrys Software Inc. *Theory: Classical simulation theory: Calculating properties: Correlation functions: Pair correlation function. In Materials Studio Online Help*, Accelrys Software Inc.: San Diego, 2014.
18. Zarzycki, J., *Glasses and the vitreous state*. Cambridge university press: 1991.

19. Accelrys Software Inc. *Forcite: Theory in Forcite: Scattering. In Materials Studio Online Help, Accelrys Software Inc.,* Accelrys Software Inc.: San Diego, 2014.
20. Žagar, E.; Žigon, M., Molar mass distribution of a commercial aliphatic hyperbranched polyester based on 2, 2-bis (methylol) propionic acid. *J. Chromatogr. A* **2004,** *1034* (1), 77-83.
21. Zagar, E.; Huskic, M.; Grdadolnik, J.; Zigon, M.; Zupancic-Valant, A., Effect of annealing on the rheological and thermal properties of aliphatic hyperbranched polyester based on 2, 2-bis (methylol) propionic acid. *Macromolecules* **2005,** *38* (9), 3933-3942.
22. Adrjanowicz, K.; Kaminski, K.; Dulski, M.; Jasiurkowska-Delaporte, M.; Kolodziejczyk, K.; Jarek, M.; Bartkowiak, G.; Hawelek, L.; Jurga, S.; Paluch, M., Dynamic Glass Transition and Electrical Conductivity Behavior Dominated by Proton Hopping Mechanism Studied in the Family of Hyperbranched Bis-MPA Polyesters. *Macromolecules* **2014,** *47* (16), 5798-5807.
23. National Physical Laboratory Dielectric properties of materials. http://www.kayelaby.npl.co.uk/general_physics/2_6/2_6_5.html (accessed December 17, 2018).
24. Chemical Retrieval on the Web DIELECTRIC STRENGTH OF POLYMERS. https://polymerdatabase.com/polymer%20physics/Dielectric%20Strength.html (accessed December 17, 2018).
25. Haynes, W. M., Dielectric Constant of Selected Polymers. In *CRC Handbook of Chemistry and Physics*, CRC Press: 2014; pp 13-15.

26. Paul, A.; Joseph, K.; Thomas, S., Effect of surface treatments on the electrical properties of low-density polyethylene composites reinforced with short sisal fibers. *Composites Science and Technology* **1997,** *57* (1), 67-79.

27. Hoffman, J. D.; Williams, G.; Passaglia, E., Analysis of the α, β, and γ relaxations in polychlorotrifluoroethylene and polyethylene: Dielectric and mechanical properties. *Journal of Polymer Science Part C: Polymer Symposia* **1966,** *14* (1), 173-235.

28. Tjong, S. C.; Liang, G.; Bao, S., Electrical behavior of polypropylene/multiwalled carbon nanotube nanocomposites with low percolation threshold. *Scripta Mater.* **2007,** *57* (6), 461-464.

29. Neagu, E.; Pissis, P.; Apekis, L.; Ribelles, J. G., Dielectric relaxation spectroscopy of polyethylene terephthalate (PET) films. *J. Phys. D: Appl. Phys.* **1997,** *30* (11), 1551.

30. Reddish, W., The dielectric properties of polyethylene terephthalate (terylene). *Transactions of the Faraday Society* **1950,** *46*, 459-475.

31. Havriliak, S.; Negami, S., A complex plane analysis of α-dispersions in some polymer systems. *J. Polym. Sci., Part C* **1966,** *14* (1), 99-117.

32. Havriliak, S.; Negami, S., A complex plane representation of dielectric and mechanical relaxation processes in some polymers. *Polymer* **1967,** *8*, 161-210.

33. Mauritz, K. A., Dielectric relaxation studies of ion motions in electrolyte-containing perfluorosulfonate ionomers. 4. Long-range ion transport. *Macromolecules* **1989,** *22* (12), 4483-4488.

34. Ouellette, R. J.; Rawn, J. D., 1 - Structure and Bonding in Organic Compounds. In *Organic Chemistry (Second Edition)*, Ouellette, R. J.; Rawn, J. D., Eds. Academic Press: 2018; pp 1-30.

35. Williams, G.; Watts, D. C., Molecular motion in the glassy state. The effect of temperature and pressure on the dielectric β relaxation of polyvinyl chloride. *Trans. Faraday Soc.* **1971,** *67*.

36. Dannhauser, W.; Bahe, L. W., Dielectric constant of hydrogen bonded liquids. III. Superheated alcohols. *J. Chem. Phys.* **1964,** *40* (10), 3058-3066.

37. Sack, R., The dielectric properties of systems containing straight polar chains. *Aust. J. Chem.* **1952,** *5* (1), 135-145.

38. Kurosaki, S.; Furumaya, T., Hydrogen bond chains and dielectric relaxation of polyvinyl alcohol. *J. Polym. Sci.* **1960,** *43* (141), 137-148.

39. Shinyashiki, N.; Sengwa, R.; Tsubotani, S.; Nakamura, H.; Sudo, S.; Yagihara, S., Broadband Dielectric Study of Dynamics of Poly (vinyl pyrrolidone)− Ethylene Glycol Oligomer Blends. *J. Phys. Chem. A* **2006,** *110* (15), 4953-4957.

40. Sinha, S.; Chatterjee, S. K.; Ghosh, J.; Meikap, A. K., Dielectric relaxation and ac conductivity behaviour of polyvinyl alcohol–HgSe quantum dot hybrid films. *J. Phys. D: Appl. Phys.* **2014,** *47* (27), 275301.

41. Rogunova, M.; Lynch, T.; Pretzer, W.; Kulzick, M.; Hiltner, A.; Baer, E., Solid-state structure and properties of hyperbranched polyols. *J. Appl. Polym. Sci.* **2000,** *77* (6), 1207-1217.

42. Lukasheva, N. V.; Tolmachev, D. A.; Nazarychev, V. M.; Kenny, J. M.; Lyulin, S. V., Influence of specific intermolecular interactions on the thermal and dielectric properties of bulk polymers: atomistic molecular dynamics simulations of Nylon 6. *Soft Matter* **2017,** *13* (2), 474-485.

43. De La Rosa, A.; Heux, L.; Cavaillé, J. Y., Secondary relaxations in poly(allyl alcohol), PAA, and poly(vinyl alcohol), PVA. II. Dielectric relaxations compared with dielectric behaviour of amorphous dried and hydrated cellulose and dextran. *Polymer* **2001,** *42* (12), 5371-5379.
44. Ishida, Y.; Takada, Y.; Takayanagi, M., Studies on dielectric properties of polyvinyl alcohol. *Kolloid-Zeitschrift* **1960,** *168* (2), 121-124.
45. Cendoya, I.; López, D.; Alegría, A.; Mijangos, C., Dynamic mechanical and dielectrical properties of poly(vinyl alcohol) and poly(vinyl alcohol)-based nanocomposites. *J. Polym. Sci., Part B: Polym. Phys.* **2001,** *39* (17), 1968-1975.
46. Suljovrujic, E., Complete relaxation map of polypropylene: radiation-induced modification as dielectric probe. *Polym. Bull.* **2012,** *68* (7), 2033-2047.
47. Lim, B.; Nowick, A.; Lee, K. W.; Viehbeck, A., Sorption of water and organic solutes in polyimide films and its effects on dielectric properties. *J. Polym. Sci., Part B: Polym. Phys.* **1993,** *31* (5), 545-555.
48. Glasstone, S.; Eyring, H.; Laidler, K. J., *The theory of rate processes*. McGraw-Hill: 1941.
49. Rachocki, A.; Markiewicz, E.; Tritt-Goc, J., Dielectric relaxation in cellulose and its derivatives. *Acta Phys. Pol. A* **2005,** *108* (1), 137-146.
50. Saiz, E.; Hummel, J.; Flory, P.; Plavsic, M., Direction of the dipole moment in the ester group. *J. Phys. Chem.* **1981,** *85* (22), 3211-3215.

CHAPTER IV - COMPARATIVE STUDY OF DIELECTRIC RELAXATION CORRELATED TO HYDROGEN BONDING ORGANIZATION BETWEEN BIS-MPA BASED HYPERBRANCHED POLYMER AND DENDRIMER: CONDUCTIVITY RELAXATION

Abstract

In this chapter, the dielectric relaxation processes of dendrimer G2 and Boltorn™ H20 at above Tγ were analyzed and compared. Combined with dynamic mechanic analysis, the relaxation detected between Tg and Tγ for G2 and H20 from dielectric spectra was assigned to conductivity relaxation, which corresponds to the ion transport in the systems. The electrical modulus, which can suppress the effect of conductivity and electrode polarization, was employed to analyze and compare the conductivity relaxation in the G2, H20, and H20-CH3 systems. The characteristic conductivity relaxation time of G2 follows Vogel−Fulcher−Tamman (VFT) and Arrhenius relationship at above and below Tg respectively, whereas that of H20 and H20-CH3 display VFT dependence only. The difference in temperature dependence reveals that the degree of coupling of ion transport from structural motion is the greatest in G2, followed by H20, and then H20-CH3. A comparison of the ion mobility and structural dynamics between H20 and H20-CH3 suggests that ion motion in the G2 and H20 systems is mainly proton hopping through hydrogen bonds. The analysis of the time-domain function suggests that the proton hopping in the G2 system is mainly realized through the Grotthuss mechanism, whereas in H20 a more complicated process is associated with α-relaxation. As the concentration of hydroxyl groups is similar for both H20 and G2, the difference in proton hopping process was attributed to the formation of hydrogen bonding. The higher portion

of long H-bonded clusters in G2 may facilitate the proton hopping. Finally, the DC conductivity of the three investigated systems were found to follow the Barton-Nakajima-Namikawa (BNN) relationship, which confirms that the mobility of the ions dictates the conductivity.

4.1 Introduction

As it was mentioned from the previous chapter, the dielectric spectra of the bis-MPA based dendritic polymers began suffering from the effects of high DC conductivity and electrode polarization as temperature increases close to Tg. Hence, in contrast to the γ-relaxation, which was reported by all the dielectric studies so far, it was debatable whether another sub-Tg relaxation, which is denoted as β-relaxation, could be clearly resolved from the dielectric spectra of neat Boltorn HBPs. The β-relaxation was firstly identified by Malmstrom etc. from a 50/50 blend of the 5th generation Boltorn HBP with linear polyethylene and was assigned to the rotation of ester groups.[1] For neat HBPs, while research conducted by Zhu etc. revealed that the β-relaxation of Boltorn H20 to H50 was completely masked by conductivity, a similar study by Turky, etc. reported distinct β process from the dielectric spectra of the same four HBPs except for H20. [2, 3] In the most recent work by Androulaki, etc., the β-relaxation, though identified, was still covered by high conductivity or merged with γ-relaxation. Hence, to probe the β-relaxation different techniques are required as complementary methods to dielectric spectroscopy. [4]

To suppress the conductivity and electrode polarization effects on Boltorn HBPsabove Tg, the electric modulus was employed, from which another relaxation

process was detected and assigned to the translational motions of the ions. [2, 5] This relaxation, which was denoted as conductivity relaxation, was also found in other polymer electrolytes and ionic liquids. [6, 7] In these systems, since the ion diffusion is orders of magnitude higher than molecular dynamics, a decoupling phenomenon can be detected from the temperature dependence of the characteristic relaxation time where Vogel−Fulcher−Tamman (VFT) and Arrhenius behavior can be observed at above and below Tg respectively. This is because the ion transport couples with segmental motions above Tg and decouples below Tg.[5-8] Since the temperature range of the conductivity relaxation coincides with that of the β-relaxation, it is unclear whether the so-called β-relaxation is just the Arrhenius part of the conductivity relaxation.

Adrjanowicz etc. ascribed the conductivity relaxation in the HBP systems to proton hopping along hydrogen bonds based on the linear relationship between the decoupling index and the number of terminal hydroxyls. However, the correlation between proton hopping and terminal hydroxyls was not well explained. Moreover, the decoupling index values determined for Boltorn HBPs are much lower than other proton hopping systems. [8, 9]

In this study, the relaxation processes of G2 and H20 above Tγ were analyzed and compared via dielectric spectroscopy. Dynamic mechanical analysis (DMA) was utilized to check the existence of β-relaxation. The electric modulus was introduced to analyze the conductivity relaxation. In order to explore the correlation between ion transport and hydrogen bonding the fully acetylated H20, H20-CH3 was also analyzed. This study would provide us an insightful understanding of the mechanism of the conductivity relaxation in hydroxylated dendritic polymers and its correlation with the formation of

hydrogen bonding. It is hypothesized that the conductivity relaxation of the bis-MPA based dendritic polymers was due to proton hopping via the Grotthuss mechanism and the formation of long clusters assists the proton transport.

4.2 Experimental Section

4.2.1 Materials and sample preparation

The second-generation hyperbranched polyester (HBP), Boltorn™ H20, was kindly donated by Perstorp Polyols Inc. The dendritic polymer was synthesized via a one-pot method using PP50 core and bis-MPA branching monomer. The theoretical (based on composition) molecular weight of Boltorn H20 is of is 1749 g/mol. According to Chapter II, the number average molecular weight ($\overline{M_n}$) and degree of branching (DB) (using the definition given by Frey) of H20 determined by NMR was 859 g/mol and 0.258 respectively.

The dendrimer G2 was synthesized in house from bis-MPA branching monomer and pentaerythritol core using an iterative anhydride coupling approach as described elsewhere.[10, 11] The theoretical molecular weight of G2 based on its structure was calculated as 1529.5 g/mol. The molecular weight, which is 1528.8 g/mol, and monodispersity of G2 was determined and confirmed by MALDI-ToF MS. Thin films of G2 and H20 were prepared using the Carver Melt Press by following the procedure described in Chapter II.

End capping modification of H20 (targeting 100% of esterification) was carried out following the methodology by Malmstrom and Hult where 5.0g (2.86 mmol) H20 was reacted with 13.90 g triethylamine (137.6 mmol) and 7.20g acetyl chloride

(91.52mmol) to ensure the completion of the reaction.[12] The detailed procedure can be found in Chapter III.

4.2.2 Experimental methods

Thermal behavior was investigated by differential scanning calorimetry (DSC) using a TA Instruments DSC Q-100. The calibration was carried out using indium and sapphire standards. Samples were first heated to 200°C at a rate of 10°C/min to erase thermal history, quenched to -90°C at 5°C/min, and then heated to 200°C at 10°C/min. The second heating scans were reported.

Dynamic mechanical analysis (DMA) was used to investigate and compare the mechanical relaxation behavior of H20 and G2. A Thermal Analysis Q800 instrument was employed and the measurements were conducted at constant frequency 1 Hz, strain amplitude of 0.01 % and by heating samples from -90 to 60 °C with a heating rate of 3 °C/min.

Dielectric measurements were carried out by a Novocontrol GmbH Concept 80 Broadband Dielectric Spectrometer using the frequency range 0.01 to 1 MHz. G2 and H20 were measured from -100 to 100 °C and -100 to 150 °C respectively.

4.3 Results and Discussion

4.3.1 Thermal analysis

The DSC and DMA curves of G2 and H20 are shown in Figure 4.1. The glass transition temperature (T_g) of both G2 and H20 was observed at 4 °C and 49 °C respectively from their DSC curves. As was discussed in our previous work, the lower T_g

of H20 is due to its lower molecular weight, broad molecular weight distribution, and weaker hydrogen bonding interaction contributed by a lower fraction of terminal hydroxyls. In contrast to G2, of which the DSC curve is almost flat at above T_g, H20 displays an exothermic peak followed by a broad endothermic peak. According to our previous studies, the exothermic and endothermic peaks can be ascribed to the formation and melting of a mesophase formed by linear segments connected via hydrogen bonds in HBPs. [13, 14]

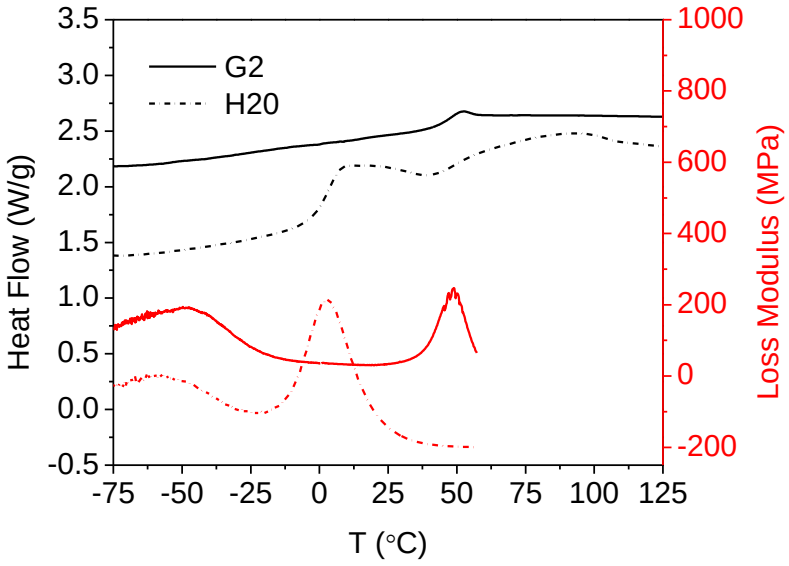

Figure 4.1 *DSC and DMA curves of G2 and H20.*

From the DMA curves, T_g values of G2 and H20 can also be determined curves as 2.4 °C and 49.2 °C respectively at 1Hz, which agree well with the DSC results. In addition, γ-relaxation can be detected from both G2 and H20 at -49°C and -57°C respectively, which is inconsistent with the previously reported γ-relaxation detected via

dielectric spectroscopy at -54°C and -60°C respectively at 1Hz. Apart from these two relaxations, no third relaxation can be observed, which indicates that there's no β-relaxation between T_γ and T_g for either polymer.

4.3.2 Dielectric analysis

From the permittivity spectra of G2 and H20 against temperature presented in Chapter III, at temperatures right above the γ-relaxation, another relaxation can be observed on the ε" spectra of G2. This relaxation was as a sub-T_g relaxation as its peak maximum was found at 26°C at 1Hz, which is about 23 °C lower than the T_g of G2 determined by DCS and DMA. A similar relaxation has been detected for bis-MPA based HBPs, which was designated as β-relaxation and attributed to the motion of ester groups according to literature. [1, 12, 15] However, this claim contradicts the DMA results of G2 where no third mechanical relaxation was observed at around 26°C. Instead of mechanical motions of either side groups or chain segments, the origin of this relaxation should be charge motions in the system. Hence the relaxation is termed as conductivity relaxation, which is denoted as c-relaxation. In contrast, from the permittivity spectra of H20, no relaxation can be observed except for γ-relaxation as ε″ starts increasing abruptly at temperature in the vicinity of T_g due to the increase of DC conductivity. [2, 3, 5] Since the T_g of H20 is very close to the reported T_c for the similar HBPs, the c-relaxation of H20, if it exists, may be masked by the high conductivity. [1, 12, 15]. For both polymers, α-relaxation was hidden by the drastic increase of ε″ at a temperature above T_g which due to the high conductivity. [2, 5, 15]

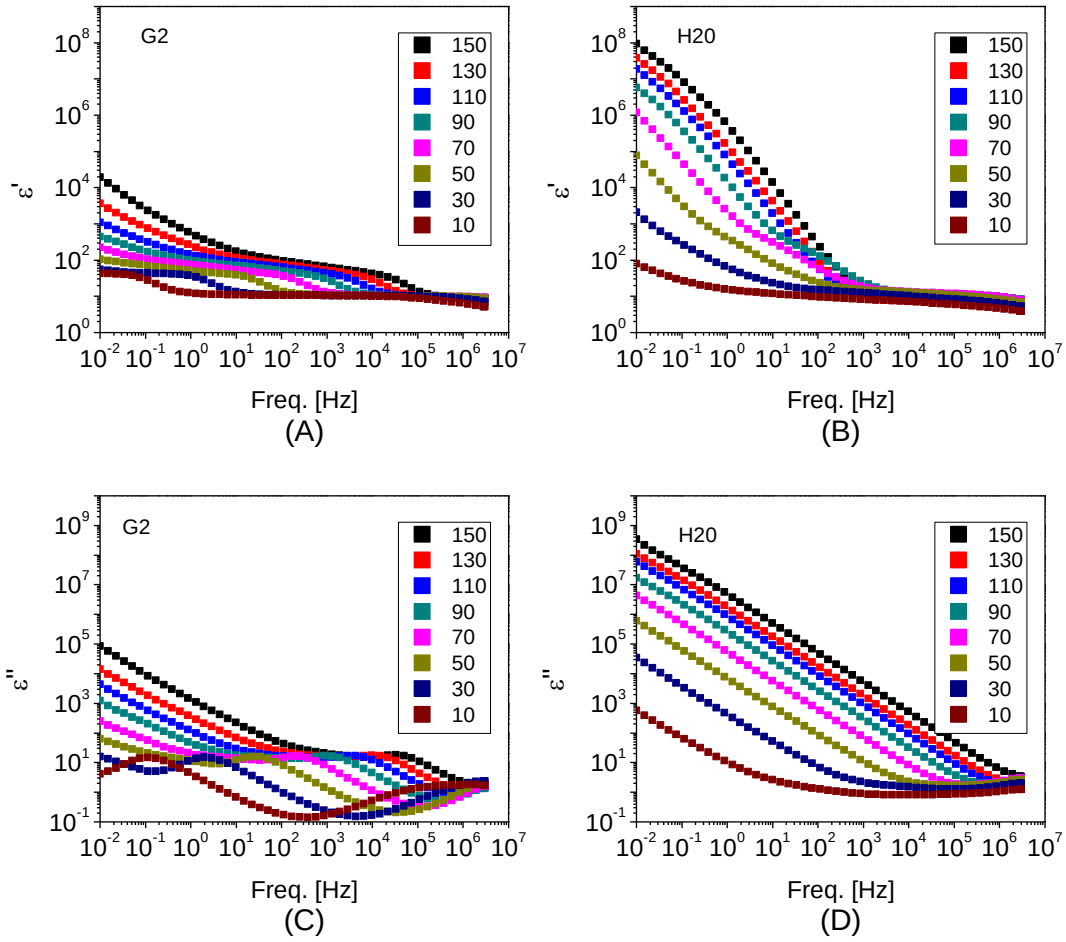

Figure 4.2 *Real ((A) and (B)) and imaginary part ((C) and (D)) of complex dielectric permittivity for G2 ((A) and (C)) and H20 ((B) and (D)) from 10 to 150°C.*

Figure 4.2 shows the real and imaginary part of the complex permittivity for G2 and H20 as a function of frequency at temperatures from 10 to 150 °C. From the permittivity loss spectra of G2, both γ- and c-relaxation can be observed. The γ-relaxation can still be detected at high frequencies at temperatures below 50°C. The c-relaxation peaks were seen within the entire temperature and frequency range with peak maximum shifting towards lower frequencies as temperature decreases. Meanwhile, on the ε′ spectra

of G2, a large increase was observed upon c-relaxation leading to a high plateau value of 40. At frequencies below c-relaxation, both ε′ and ε″ started increasing drastically as frequency decreases especially at high temperatures due to interfacial polarization and DC conductivity. [2, 5, 15]

On the other hand, on the ε″ spectra of H20, loss peaks were completely masked by the sharp increase of ε″ contributed by DC conductivity. Still, some kinks can be observed on the ε' curves at intermediate frequencies, which might be the traces of c-relaxation.

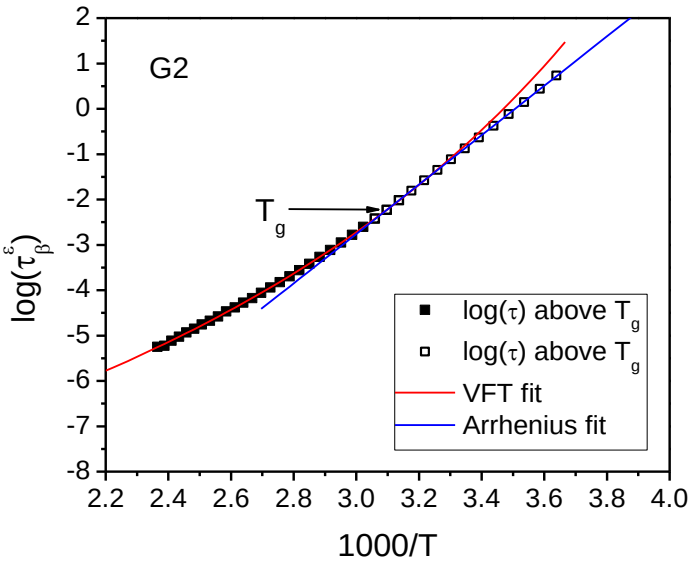

Figure 4.3 *Temperature dependence of the characteristic c-relaxation time* $\boldsymbol{\tau_c^{\varepsilon}}$ *plotted as a function of 1000/T for G2.*

The permittivity data of G2 was fitted to the Havriliak-Negami (HN) equation in order to extract the relaxation times of c-relaxation. [16, 17] The built-in HN equation of the WINFIT software by Novo-control reads:

$$\varepsilon^* = \varepsilon' - i\varepsilon'' = -i\,(\frac{\sigma_{dc}}{\varepsilon_0 \omega})^N + \frac{\Delta\varepsilon}{(1+(i\omega\tau_{HN})^{\alpha})^{\beta}} + \varepsilon_\infty \quad (26)$$

The first term accounts for the conductivity, where σ_{dc} is the DC conductivity and the exponent N reflects the degree of interconnectivity of charge hopping pathways. [18] $\varepsilon_0 = 8.854 \times 10^{-12}$ F·m^{-1}, which is the permittivity of the vacuum. $\omega = 2\pi f$, which is angular frequency. The following term accounts for the relaxation. Δε is the permittivity strength and ε_∞ is ε′ at infinity high frequency. α and β are parameters that describes the width and the symmetry of the relaxation peak.[16] The Havriliak-Negami relaxation time, τ_{HN}, is related to the actual relaxation time, τ_{max}, which is determined by equation $\tau_{max} = \frac{1}{2\pi f_{max}}$, where f_{max} is the frequency at the loss peak maximum.

As shown in Figure 4.3, the temperature dependence of the characteristic relaxation time of G2 changes from a non-Arrhenius to Arrhenius relationship as the temperature approaches T_g, which again confirms that the c-relaxation originated from charge motions rather than motions of ester groups, which would display Arrhenius behavior only. According to the literature, the transition in temperature dependence discovered in HBPs was explained by the decoupling of the translational motion of charges from the segmental dynamics when the system vitrifies. [5, 8] This decoupling phenomenon was also found in some polymer electrolytes and ionic liquids. [6, 7] At temperatures above T_g, the decoupling phenomenon is insignificant as the segmental motion is fast enough to interfere with the translational motion of charges, hence the characteristic relaxation time follows a non-Arrhenius behavior which is described by the Vogel−Fulcher−Tamman (VFT) equation which can be expressed by following forms: [19, 20]

$$\tau(T) = \tau_0 \exp\left(\frac{B}{T - T_0}\right) \tag{27}$$

where τ_0, B, and T_0 are fitting parameters. The parameter B is related to activation energy at very high temperature where Arrhenius behavior occurs. RB was considered as apparent energy where R is the ideal gas constant.[19 20]

When the temperature is approaching T_g, the decoupling becomes more remarkable as the segmental dynamics become frozen and can no longer affect charge motions. Hence, the temperature dependence of the c-relaxation starts to follow Arrhenius relationship, which is expressed as

$$\tau(T) = \tau_0 \exp\left(\frac{E_a}{RT}\right) \tag{28}$$

where E_a is the activation energy. The fitting parameters will be discussed later.

In order to probe the relaxations of H20 at temperatures close to and above T_g, it is required to suppress the effects of conductivity. Therefore, the complex electric modulus is introduced, which was expressed by the following equation:

$$M^*(\omega) = \frac{1}{\varepsilon^*(\omega)} = \frac{1}{\varepsilon' - i\varepsilon''} = \frac{\varepsilon'}{\varepsilon'^2 + \varepsilon''^2} + i\frac{\varepsilon''}{\varepsilon'^2 + \varepsilon''^2} = M' + iM'' \tag{29}$$

where M′ and M″ are the real and imaginary electric modulus respectively. [21]

The electric modulus loss spectra of G2 and H20 as a function of frequency from 10 to 150°C are shown in Figure 4.4, where both polymers display relaxation peaks at similar frequency ranges. As the peak positions showed good agreement with those resolved on the ε″ spectra of G2 and the reported values of H20, we can confirm that the relaxation peaks on M″ spectra of both polymers are corresponding to c-relaxation.[5] As temperature decreases, the c-relaxation peaks of G2 exhibit similar height and width, whereas those of H20 show apparent variation in peak height and a substantial increase in

peak width. This indicates that the c-relaxation in G2 is more Debye-like than that in H20.

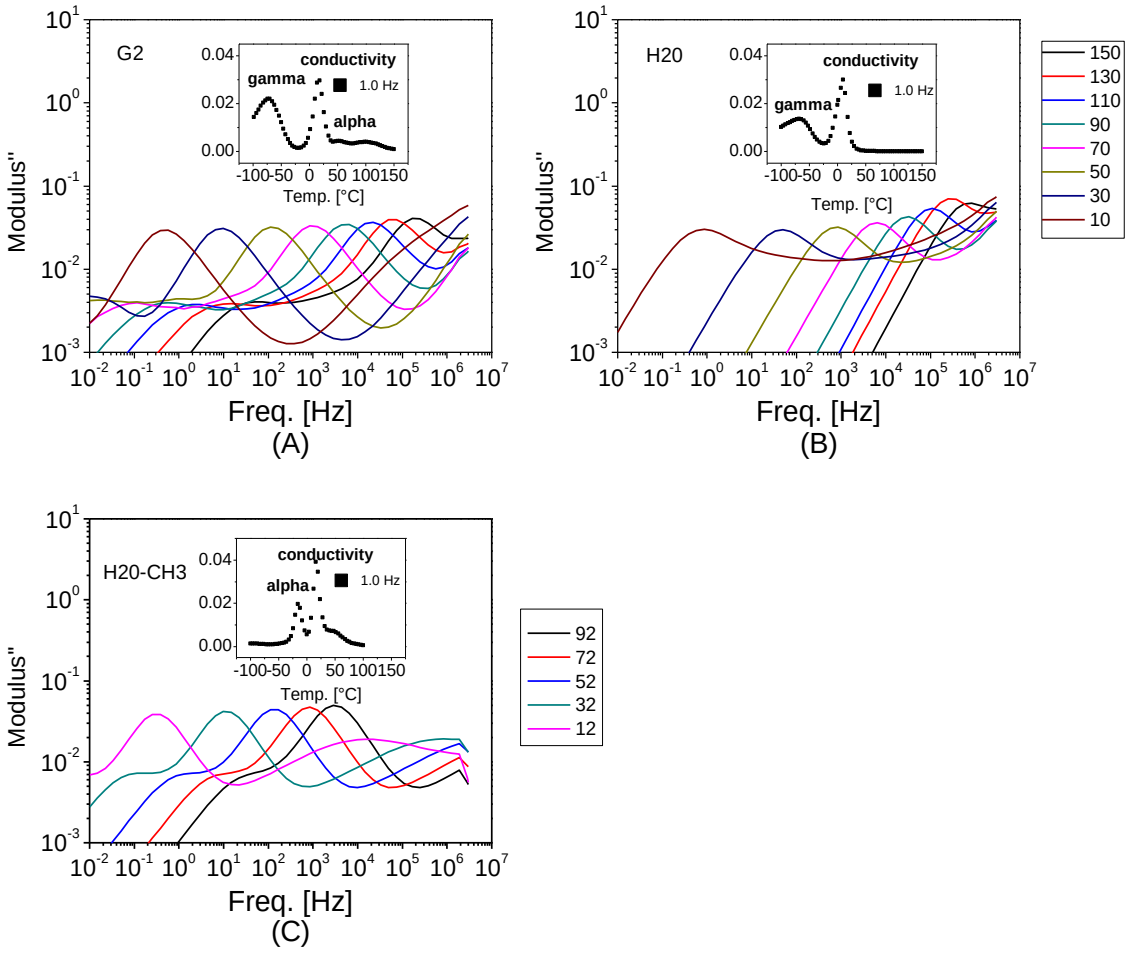

Figure 4.4 *Loss part of the complex electric modulus of G2 (A), H20 (B), and H20-CH3(C) from 10 to 150 °C as a function of frequency. The insets are the loss electric modulus as a function of temperature at 1Hz*

Additionally, two more relaxations were observed at the low-frequency side of the c-relaxation of G2: a low-frequency peak shoulder and a small peak next to it, which can only be resolved at temperatures below 70°C. The small peak was assigned to the α-relaxation as the peak maximum at 50°C was found at 1Hz, which is consistent with

DMA results. The low-frequency shoulder may be due to another conductivity relaxation at the interfaces. It is interesting that neither peak was observed on the M″ of H20. Since the T_c of H20 determined form the M″ spectra at 1Hz is very close to the T_g, it is possible that conductivity and α-relaxations merge into one. This also explains the non-Debye feature of the c-relaxation peaks of H20.

The M″ data of both G2 and H20 was also fitted to the Havriliak-Negami (HN) equation to analyze the distribution of the relaxation times. The extracted characteristic relaxation time, τ_c^M, for both polymers as a function of 1000/T is shown in Figure 4.5, where the two polymers exhibit different temperature dependencies. The τ_c^M of G2 shows similar decoupling feature as that of τ_c^ε, which follows VFT and Arrhenius relationship at temperatures above and below T_g respectively. As listed in Table 1, the fitting parameters of VFT and Arrhenius equations for both τ_c^M and τ_c^ε of G2 were approximately the same, which confirms that the relaxation detected from ε″ is the same as the one from the M″ spectra. On the other hand, the extracted τ_c^M of H20 follows VFT dependence within the entire temperature range. That is because only one data point was collected at a temperature below the T_g of H20. Other c-relaxation peaks at temperatures below 2°C were shifted out of the frequency window. Although our experimental data did not show any decoupling phenomenon from H20, it still can be detected by expanding the frequency window to much lower frequencies. [5]

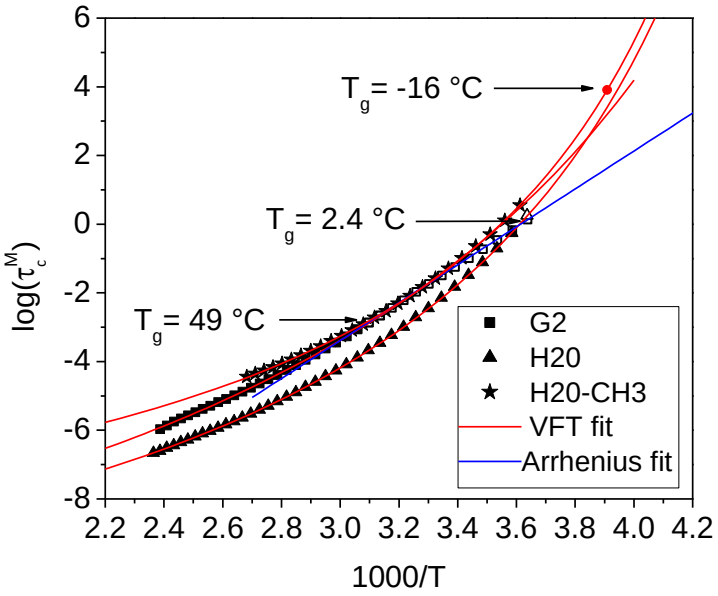

Figure 4.5 *Comparison of temperature dependence of the characteristic c-relaxation time τ_c^M between G2 and H20 and H20-CH3. Solid and open symbols represent τ_c^M above and below T_g respectively.*

The difference in the temperature dependence of the c-relaxation between G2 and H20 indicates that the decoupling feature of the charge motions in G2 is much greater than that in H20.To quantify the degree of decoupling, the decoupling index R_τ was employed as defined below[22-24]

$$R_\tau = \frac{\tau_\alpha}{\tau_c} \tag{30}$$

where τ_α is the characteristic segmental relaxation time and often assumed to be 100s or 200s at T_g measured by DSC at 10 K/min. [23, 24] To avoid any inconsistencies in this study, as the T_g values determined via DMA was collected at known frequency of 1Hz, the τ_α value was determined as the corresponding relaxation time of 1Hz, which is 0.16s. At the T_g measured by DMA at 1 Hz, τ_c of G2 and H20 was determined as 1.23×10^{-3}s and 1.36s

respectively, and the corresponding R_τ was calculated as 130.1 and 0.118 respectively. It should be noted that much greater R_τ can be determined if the τ_α value is assumed to be 100s or 200s, which suggests that the α-relaxation is much slower than c-relaxation. However, according to the M″ spectra of H20 at 1Hz shown in Figure 4.4, where the c-relaxation of H20 was detected at 10°C, which is higher than its T_g, it is more reasonable to employ the 0.16s as the τ_α value. Larger decoupling index of G2 indicates that the charge mobility in the system is much faster than the segmental motions.

Previous literature has assigned the origin of c-relaxation to the hopping of either ion impurities or protons. [2, 5] As their R_τ values are considerable low, we can hardly ascribe the origin of c-relaxation of both polymers to proton hopping via the R_τ values alone. [8, 9] Additionally, since the concentration of hydroxyl groups in G2 and H20 are very close, no direct correlation between hydroxyls and ion transport can be found. To figure out the nature of ion transport in G2 and H20, the c-relaxation of the esterified H20, H20-CH3 was also analyzed. Shown in Figure 4.4(C), the H20-CH3 also displays c-relaxation peaks on the M″ spectra with a similar shape as those of G2. In addition to that, a high-frequency peak and a low-frequency shoulder can also be observed. According to the M″ spectra at 1Hz, along with c-relaxation, H20-CH3 displays a relaxation peak at -16°C which agrees well with its T_g which determined as -18°C via DSC. No relaxation was observed below T_g. Hence, the high-frequency peak was assigned to α-relaxation. The low-frequency shoulder can be ascribed to another conductivity relaxation near the sample-electrodes interface.

The characteristic c-relaxation time of H20-CH3 is also shown in Figure 4.5, where H20 displays a lower τ_c than that of H20-CH3 within the entire temperature range.

As the T_g of H20-CH3 was lower than that of H20, the structural dynamics of H20-CH3 are faster than that of H20 at the same temperature. Hence, the higher structural dynamics and lower ion mobility of H20-CH3 as compared to H20 suggests that the charge hopping mechanisms in both systems are different. Meanwhile, at T_g where the τ_α of both H20 and H20-CH3 can be assumed to be the same, the τ_c value of H20-CH3 extrapolated via VFT fit, which is 9.33×10^3s, is about four orders of magnitude greater than that of H20. Though the types of ions may be different in both systems, their difference in mobility shall not be over one order of magnitude. [25-27] This implies that the existence of hydrogen bonding within H20 facilitates the ion motion within the H20 system. Plus, according to the preparation of H20, G2, and H20-CH3, all three systems contain protons as impurities. Therefore, the only reasonable explanation would be that the charge transport in H20 is proton hopping through hydrogen bonds via the Grotthuss mechanism. [28] For G2, since its decoupling index is even greater than that of H20, we assume that the ion transport in G2 is also proton hopping.

The fitting parameters of the VFT and Arrhenius relationships of G2, H20, and H20-CH3 are listed in Table 4.1. G2 shows the highest strength parameter B, followed by H20, and then H20-CH3, which suggests that the energy barrier at above T_g follows the trend: G2 > H20> H20-CH3. This can be explained by the free volume content, which follows the reverse order. Due to the absence of hydrogen bonding, the free volume content in H20-CH3 should be higher than H20, and the fraction free volume in H20 is higher than G2 as it was discussed in Chapter II. From the Arrhenius part, the E_a determined for G2 are close to the literature values determined for bis-MPA based HBPs reported by Malmstrom, etc.(90 kJ/mole for 5th generation), Turky, etc.(127, 114, and

116 kJ/mol for 3rd, 4th, and 5th generation respectively) and Adrjanowicz, etc.(123, 112, and 99 kJ/mol for 2nd, 3rd, and 4th generation respectively), though the first two assigned the c-relaxation to motions of ester group. [1, 3, 5, 29] Since E_a cannot be determined for H20 in the work, the E_a value of G2 was compared with the reported value of H20. Lower E_a value of G2 indicates that proton hopping is easier in G2 than in H20 at below T_g, which may be due to the formation of longer clusters in G2 as the hydroxyl concentration for polymers are the same.

Table 4.1 *Fitting parameters of G2, H20, and H20-CH3.*

Samples / Fitting parameters		G2		H20	H20-CH3
		τ_c^{ε}	τ_c^{M}	τ_c^{M}	τ_c^{M}
VFT	B (K)	2741.6	2820.7	2093.4	1640.4
	T_0 (K)	168.4	168.5	191.0	198.6
Arrhenius	Ea (kJ/mol)	104.2	103.3		

In order to describe the nonexponential decay feature of the c-relaxation of the three systems, the dielectric data was converted to the time domain and fitted to Kohlruasch-Williams-Watts (KWW) equation, which is expressed as

$$\varphi(t) = A \cdot \exp\left[-\left(\frac{t}{\tau_c}\right)^{\beta}\right] \tag{31}$$

where the stretching parameter β is between 0 and 1, which describes the departure from the Debye-type ideal exponential decay (β=1). [30] The time-domain data, as well as the KWW fitting of G2, H20, and H20-CH3, are presented in Figure 4.6. It can be observed

that the time domain function of H20 decays slower as temperatures approaches T_g whereas that of G2 shows a similar decaying rate over the entire temperature range. This difference was reflected in the β values shown in the insets. While the β value of G2 stays almost constant at about 0.78 through temperatures from 102 to 2°C, that of H20 starts to decrease from 0.7 to 0.4 from 70°C to 2°C. The lower β value of H20 indicates that the c-relaxation of the H20 deviates greatly from the Debye relaxation, which confirms our hypothesis that it merges with the α-relaxation. On the other hand, the higher β value of G2 reveals that the c-relaxation in the system is Debye-like, which indicates that the conductivity mechanism in G2 involves no structural diffusion. This confirms that ion transport in G2 is dominated by proton hopping along hydrogen bonds via the Grotthuss mechanism.

The KWW function of H20-CH3 also follows Debye-like exponential decay like G2, with its β values remaining almost constant at about 0.83. It is because the T_g of H20-CH3 is much lower than its T_c that the c-relaxations is well separated from α-relaxation. Hence the c-relaxation of H20-CH3 is only corresponding to the ion hopping in the system.

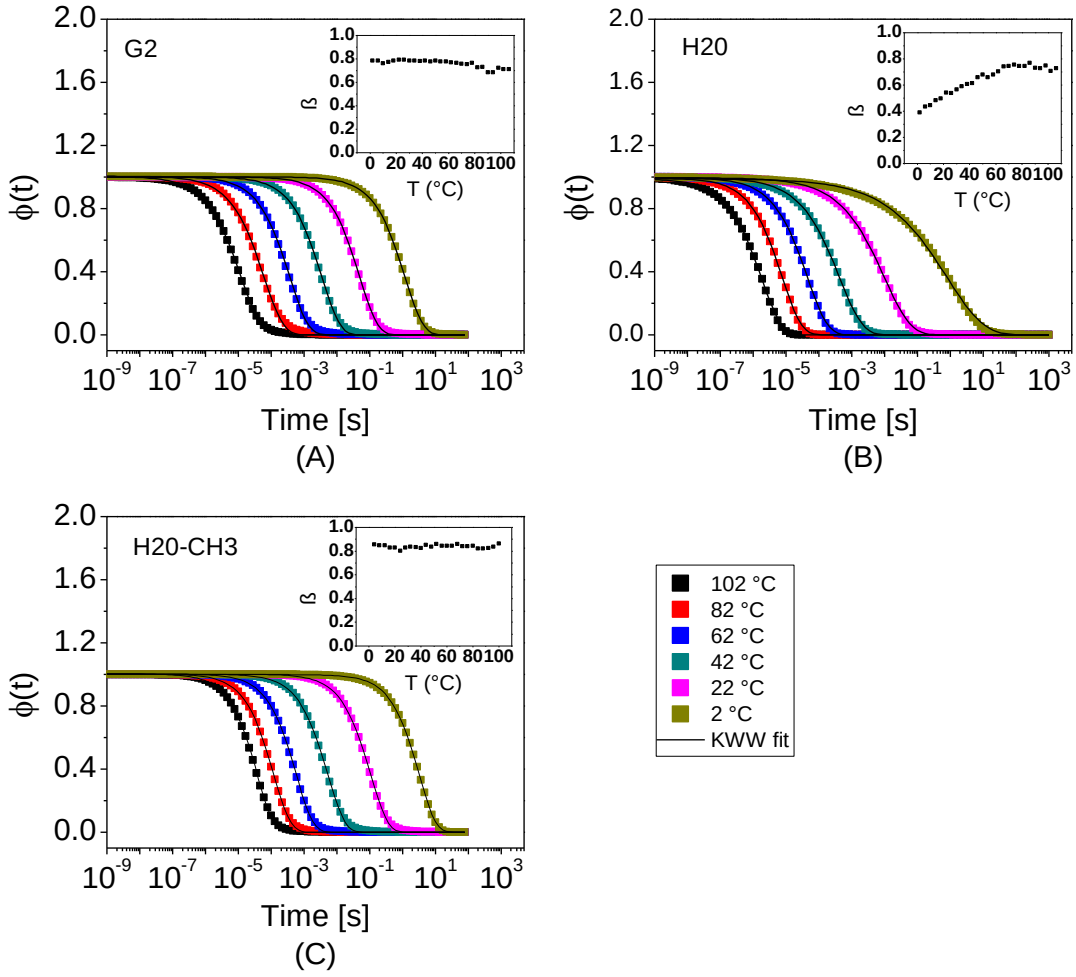

Figure 4.6 *Time domain function of electric modulus spectra and the KWW fit for G2, H20, and H20-CH3 from 102 to 2 °C. Insets were the β values from the KWW fitting for each sample.*

To investigate the relationship between the ion mobility and conductivity in G2 and H20, the real part of the complex conductivity, σ′, was analyzed. As shown in Figure 4.7, σ′ of the three investigated systems is plotted as a function of frequency. For all these three polymers, σ′ shows AC conductivity at the high frequencies which are due to the γ-relaxation, followed by a DC conductivity plateau as frequency decreases. Both the

critical frequency where the plateau starts and the corresponding plateau value increase with decreasing temperature. For both G2 and H20-CH3, as the frequency continues decreasing, σ′ decreases again, followed by a secondary plateau with very low frequency dependence. On the other hand, for H20, this plateau extends through the rest of the frequency window with the exception of a slight drop of σ′ which can be observed at high temperatures and very low frequencies.

The drop of σ′ after the high-frequency plateau of G2 and H20-CH3 is due to electrode polarization, which can be found in HBPs, ionic conducting fluids, and polymer electrolytes. [6, 7, 15, 31-33] The low-frequency plateau, which has been seldom reported in polymers, can be ascribed to the incomplete blocking layers formed by ions at the electrode-polymer interface which lead to very low DC conductivity. [31, 33] It is still unclear why the low-frequency plateau is absent from the σ′ spectra of H20. However, we can still make some plausible speculations as sometimes G2 also displays similar σ′ spectra as H20 with extended DC conductivity plateau. (Appendix Figure A.2) (It should be noted there's no difference in DC values and the critical frequencies.) The reason should lie in the experimental set up rather than the samples themselves. Since both G2 and H20-CH3 showed greater impact from electrode polarization, it is reasonable to assume that the stronger blocking layers were formed in these two systems, which can be attributed to better contact between the sample and the electrodes. On the contrary, as H20 suffered fewer effects from the electrode polarization, the contact between the sample and electrodes may not have been as good as that in G2 and H20-CH3. Therefore, we assume that there might have been some bubbles between the electrode and H20 samples which prevented the formation of strong blocking layers.

Though electrode polarization has strong effects on the low-frequency side of the σ′ spectra, it shows little effects on the high-frequency side. The following session will be mainly focused on the DC conductivity plateau on the high-frequency side. Over the three systems, H20 displays the highest DC conductivity value, followed by G2, and then H20-CH3. To better compare their DC conductivity, the σ′ spectra of the three investigated systems were analyzed and fitted to the Jonscher equation: [34]

$$\sigma'(f) = \sigma_0 + Af^n = \sigma_0[1 + (\frac{f}{f_c})^n] \quad (32)$$

where σ_0 is the DC conductivity at frequency equals to 0 and f_c is the critical frequency where σ′ begins to increase with frequency from the DC plateau. n is an empirical fitting parameter, which is generally seen between 0 and 1 though examples for which n>1 also exist. [35] The fitting curves are also shown in Figure 4.8. The temperature dependence of σ_0 values for each polymer is presented in Figure 4.8, where σ_0 exhibits virtually the exact opposite temperature dependence as τ_c^M. Still, both H20 and H20-CH3 follow VFT relationship, whereas G2 exhibits VFT and Arrhenius behavior at above and below T_g respectively. At temperature close to the T_g of H20, there's an intersection point of the two fitting curves for G2 and H20, upon which σ_0 of H20 is higher and below which the σ_0 of G2 is higher. On the other hand, σ_0 of H20 is higher than H20-CH3 over the entire temperature range. These trends of σ_0 exactly mirror with τ_c.

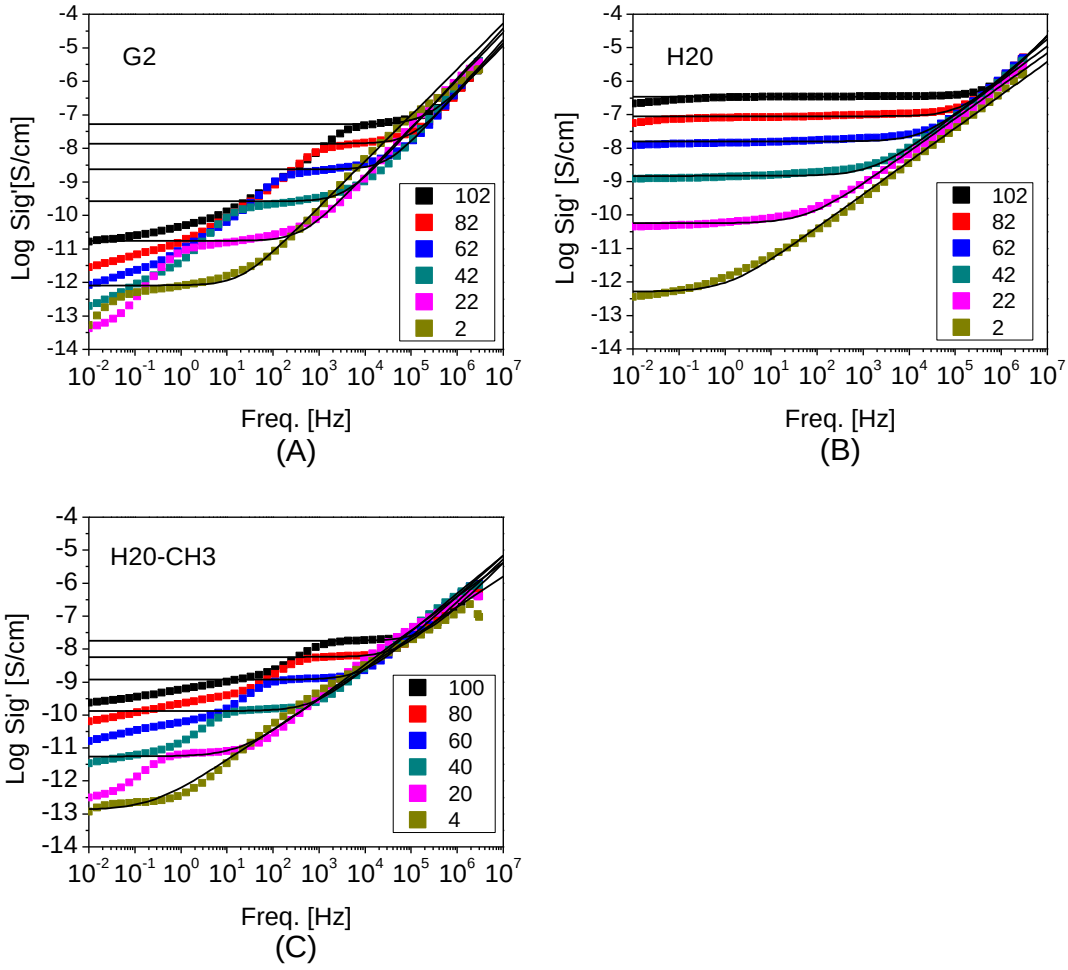

Figure 4.7 . *The real part of the complex conductivity, σ', as a function of frequency and the Jonscher fit for (A) G2, (B) H20, and (C) H20-CH3.*

In order to investigate how close the DC conductivity was correlated with the ion mobility, the σ_0 of the three investigated systems was plotted as a function of the characteristic frequency of c-relaxation, f_{max}, which is defined as $f_{max} = \frac{1}{2\pi\tau_c^M}$. It can be observed that the logarithm of σ_0 and f_{max} of all three systems follows a linear

relationship, of which the slopes are very close to unity. This indicates that the logarithm of σ_0 and f_{max} follow the Barton-Nakajima-Namikawa (BNN) relationship:

$$\sigma_0 = p\Delta\varepsilon\varepsilon_0\omega_m \text{ where } \omega_m = 2\pi f_{max} \quad (33)$$

where p is a numerical constant of order 1. [35-37] This direct correlation between the DC conductivity and the reversed c-relaxation time confirms that the nature of c-relaxation of all three systems is ion hopping which contributes to the DC conductivity. The electrode polarization shows little effect on the ion hopping and the DC conductivity in the bulk. We can also conclude that the mobility of the ions dictates the conductivity of all these three systems. H20 has the highest DC conductivity of the three polymers at temperatures above its T_g due to its high segmental dynamics and the associated proton hopping. At temperature below T_g, since the proton hopping in H20 is much less decoupled from the structural dynamics as compared to G2, its DC conductivity becomes lower than G2. The greater degree of decoupling in G2 may be contributed by its higher fraction of long H-bonded clusters. H20-CH3 shows the lowest DC conductivity as its charge transport mechanism is not proton hopping, though its segmental dynamics is the fastest.

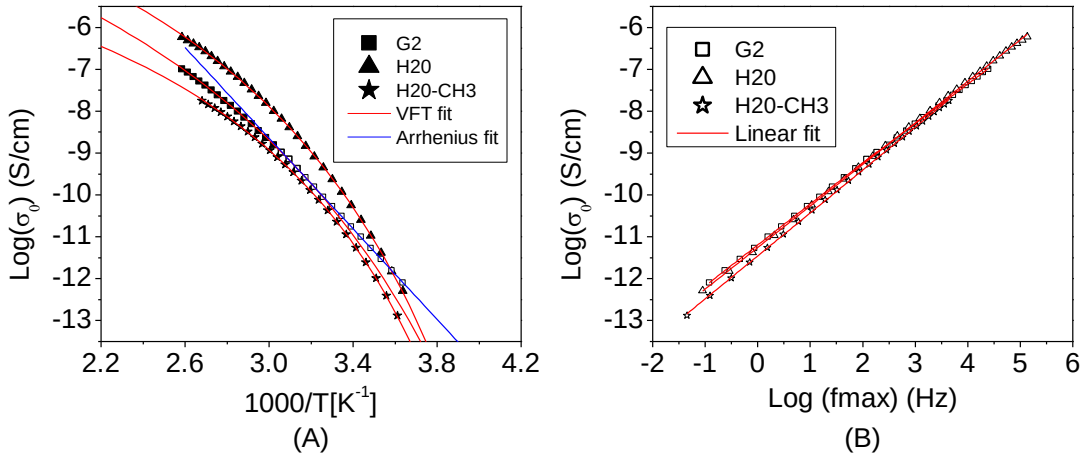

Figure 4.8 *Temperature dependence (A) and frequency dependence (B) of DC conductivity for G2, H20 and H20-CH3.*

4.4 Conclusion

The molecular relaxation, as well as the conductivity properties of a second-generation dendrimer G2, a hyperbranched polymer Boltorn^{TM} H20, and the alkyl, terminated H20, H20-CH3, were studied using a broadband dielectric spectrometer. A secondary relaxation was detected on the M″ spectra of all three systems. Due to its absence in the DMA data, the relaxation was ascribed to ion transport and termed as c-relaxation.

The characteristic c-relaxation time of G2 shows the decoupling feature which follows the VFT relationship above T_g and Arrhenius below T_g. This is due to the fact that ion translational motion couples with segmental motion at above T_g, and then decouples with it when the system vitrifies at below T_g. Higher ion mobility and lower structural dynamics of H20 as compared to H20-CH3 suggested that hydrogen bonding

facilitates the ion motion in H20. The existence of protons in all three systems implies that the ion motion in H20 and G2 systems are dominated by proton hopping.

Through the analysis of time-domain function, the exponential-like decay was observed in G2, which suggests that the proton hopping in the system is mainly realized through the Grotthuss mechanism. The non-Debye behavior of H20 suggests that ion conduction in H20 is associated with α-relaxation. As the concentration of hydroxyl groups is similar for both H20 and G2, the difference in the degree of decoupling and decay behavior lies in the formation of hydrogen bonding. A higher fraction of longer H-bonded clusters in G2 allows the proton hops to occur orders of magnitude faster than its segmental motion. The conductivity data of the three investigated systems follow the Barton-Nakajima-Namikawa (BNN) relationship. This confirms that the mobility of the ions dictates the conductivity.

4.5 References

1. Malmström, E.; Liu, F.; Boyd, R.; Hult, A.; Gedde, U., Relaxation processes in hyperbranched polyesters. *Polym. Bull.* **1994,** *32* (5-6), 679-685.
2. Zhu, P. W.; Zheng, S.; Simon, G., Dielectric relaxations in a hyperbranched polyester with terminal hydroxyl groups: effects of generation number. *Macromol. Chem. Phys.* **2001,** *202* (15), 3008-3017.
3. Turky, G.; Shaaban, S. S.; Schoenhals, A., Broadband Dielectric Spectroscopy On the Molecular Dynamics in Different Generations of Hyperbranched Polyester. *J. Appl. Polym. Sci.* **2009,** *113* (4), 2477-2484.
4. Androulaki, K.; Chrissopoulou, K.; Prevosto, D.; Labardi, M.; Anastasiadis, S. H., Dynamics of hyperbranched polymers under confinement: a dielectric relaxation study. *ACS Appl. Mater. Inter.* **2015,** *7* (23), 12387-12398.
5. Adrjanowicz, K.; Kaminski, K.; Dulski, M.; Jasiurkowska-Delaporte, M.; Kolodziejczyk, K.; Jarek, M.; Bartkowiak, G.; Hawelek, L.; Jurga, S.; Paluch, M., Dynamic Glass Transition and Electrical Conductivity Behavior Dominated by Proton Hopping Mechanism Studied in the Family of Hyperbranched Bis-MPA Polyesters. *Macromolecules* **2014,** *47* (16), 5798-5807.
6. Sangoro, J. R.; Iacob, C.; Agapov, A. L.; Wang, Y.; Berdzinski, S.; Rexhausen, H.; Strehmel, V.; Friedrich, C.; Sokolov, A. P.; Kremer, F., Decoupling of ionic conductivity from structural dynamics in polymerized ionic liquids. *Soft Matter* **2014,** *10* (20), 3536-3540.
7. Gainaru, C.; Stacy, E. W.; Bocharova, V.; Gobet, M.; Holt, A. P.; Saito, T.; Greenbaum, S.; Sokolov, A. P., Mechanism of conductivity relaxation in liquid and

polymeric electrolytes: Direct link between conductivity and diffusivity. *J. Phys. Chem. B* **2016,** *120* (42), 11074-11083.

8. Sangoro, J. R.; Turky, G.; Abdel Rehim, M.; Iacob, C.; Naumov, S.; Ghoneim, A.; Kärger, J.; Kremer, F., Charge Transport and Dipolar Relaxations in Hyperbranched Polyamide Amines. *Macromolecules* **2009,** *42* (5), 1648-1651.
9. Mizuno, F.; Belieres, J. P.; Kuwata, N.; Pradel, A.; Ribes, M.; Angell, C. A., Highly decoupled ionic and protonic solid electrolyte systems, in relation to other relaxing systems and their energy landscapes. *J. Non-Cryst. Solids* **2006,** *352* (42), 5147-5155.
10. Ihre, H.; Padilla De Jesús, O. L.; Fréchet, J. M., Fast and convenient divergent synthesis of aliphatic ester dendrimers by anhydride coupling. *J. Am. Chem. Soc.* **2001,** *123* (25), 5908-5917.
11. Elmahdy, M. M.; Chrissopoulou, K.; Afratis, A.; Floudas, G.; Anastasiadis, S. H., Effect of Confinement on Polymer Segmental Motion and Ion Mobility in PEO/Layered Silicate Nanocomposites. *Macromolecules* **2006,** *39* (16), 5170-5173.
12. Malmström, E.; Johansson, M.; Hult, A., The effect of terminal alkyl chains on hyperbranched polyesters based on 2, 2-bis (hydroxymethyl) propionic acid. *Macromol. Chem. Phys.* **1996,** *197* (10), 3199-3207.
13. Zagar, E.; Huskic, M.; Grdadolnik, J.; Zigon, M.; Zupancic-Valant, A., Effect of annealing on the rheological and thermal properties of aliphatic hyperbranched polyester based on 2, 2-bis (methylol) propionic acid. *Macromolecules* **2005,** *38* (9), 3933-3942.

14. Syed, M. N. Hydrogen Bond-Mediated Structural Order in Hydroxylated Bis-MPA Dendritic Polymers: Experimental and Molecular Dynamics Simulation Study. Ph.D. Thesis, The University of Southern Mississippi, 2015.
15. Turky, G.; Shaaban, S. S.; Schöenhals, A., Broadband dielectric spectroscopy on the molecular dynamics in different generations of hyperbranched polyester. *J. Appl. Polym. Sci.* **2009,** *113* (4), 2477-2484.
16. Havriliak, S.; Negami, S., A complex plane analysis of α-dispersions in some polymer systems. *J. Polym. Sci., Part C* **1966,** *14* (1), 99-117.
17. Havriliak, S.; Negami, S., A complex plane representation of dielectric and mechanical relaxation processes in some polymers. *Polymer* **1967,** *8*, 161-210.
18. Mauritz, K. A., Dielectric relaxation studies of ion motions in electrolyte-containing perfluorosulfonate ionomers. 4. Long-range ion transport. *Macromolecules* **1989,** *22* (12), 4483-4488.
19. Metatla, N.; Soldera, A., The Vogel−Fulcher−Tamman Equation Investigated by Atomistic Simulation with Regard to the Adam−Gibbs Model. *Macromolecules* **2007,** *40* (26), 9680-9685.
20. Ferry, J. D., *Viscoelastic properties of polymers*. John Wiley & Sons: 1980.
21. McCrum, N. G.; Read, B. E.; Williams, G., *Anelastic and dielectric effects in polymeric solids*. Wiley: New York, 1967.
22. Angell, C. A., Mobile Ions in Amorphous Solids. *Annu. Rev. Phys. Chem.* **1992,** *43* (1), 693-717.
23. Angell, C. A., Dynamic processes in ionic glasses. *Chem. Rev.* **1990,** *90* (3), 523-542.

24. Angell, C. A., Fast ion motion in glassy and amorphous materials. *Solid State Ionics* **1983,** *9-10*, 3-16.

25. Jaffrezic-Renault, N.; Dzyadevych, S. V., Conductometric microbiosensors for environmental monitoring. *Sensors* **2008,** *8* (4), 2569-2588.

26. Atkins, P. W.; De Paula, J.; Keeler, J., Atkins' physical chemistry. Oxford university press: 2018; p 019.

27. Varcoe, J. R.; Atanassov, P.; Dekel, D. R.; Herring, A. M.; Hickner, M. A.; Kohl, P. A.; Kucernak, A. R.; Mustain, W. E.; Nijmeijer, K.; Scott, K., Anion-exchange membranes in electrochemical energy systems. *Energy & Environmental Science* **2014,** *7* (10), 3135-3191.

28. Agmon, N., The Grotthuss mechanism. *Chem. Phys. Lett.* **1995,** *244* (5), 456-462.

29. Malmström, E.; Hult, A.; Gedde, U.; Liu, F.; Boyd, R., Relaxation processes in hyperbranched polyesters: influence of terminal groups. *Polymer* **1997,** *38* (19), 4873-4879.

30. Williams, G.; Watts, D. C., Non-symmetrical dielectric relaxation behaviour arising from a simple empirical decay function. *Trans. Faraday Soc.* **1970,** *66* (0), 80-85.

31. Emmert, S.; Wolf, M.; Gulich, R.; Krohns, S.; Kastner, S.; Lunkenheimer, P.; Loidl, A., Electrode polarization effects in broadband dielectric spectroscopy. *Eur. Phys. J. B* **2011,** *83* (2), 157.

32. Turky, G.; Sangoro, J. R.; Abdel Rehim, M.; Kremer, F., Secondary relaxations and electrical conductivity in hyperbranched polyester amides. *J. Polym. Sci., Part B: Polym. Phys.* **2010,** *48* (14), 1651-1657.

33. Serghei, A.; Tress, M.; Sangoro, J.; Kremer, F., Electrode polarization and charge transport at solid interfaces. *Phys. Rev. B* **2009,** *80* (18), 184301.

34. Jonscher, A. K., The 'universal' dielectric response. *Nature* **1977,** *267* (5613), 673-679.

35. Dyre, J. C.; Schrøder, T. B., Universality of ac conduction in disordered solids. *Rev. Mod. Phys.* **2000,** *72* (3), 873.

36. Macdonald, J. R., Universality, the Barton Nakajima Namikawa relation, and scaling for dispersive ionic materials. *Phys. Rev. B* **2005,** *71* (18), 184307.

37. Dyre, J. C., The random free-energy barrier model for ac conduction in disordered solids. *J. Appl. Phys.* **1988,** *64* (5), 2456-2468.

CHAPTER V – STEREOCHEMICAL AND SEQUENCE EFFECTS ON HYDROGEN-BONDING AND BARRIER PROPERTIES OF POLY (NORBORNENE DIMETHANOL)-*CO*-POLY(NORBORNENE) COPOLYMERS

Abstract

Novel dimethanol-functionalized polynorbornene copolymers, the hydrogenated poly(endo, endo-norbornene dimethanol)-co-poly(norbornene) (H-PddNBdOH-co-PNB) and poly(endo, exo-norbornene dimethanol)-co-poly(norbornene) (H-PdxNBdOH-co-PNB), were synthesized and probed for gas barrier properties. With about the same OH content, H-PddNBdOH-co-PNB exhibits much higher permeability than H-PdxNBdOH-co-PNB, of which permeability is comparable to EVOH with equivalent mol% OH content. PAL measurements revealed that the free volume hole size in the endo, endo copolymer is much larger than that in the endo, exo counterparts. The combination of experimental and computational simulation infers a relationship between H-bond organization (inter-, intramolecular, and intra-unit H-bonding) and barrier property. It was discovered that endo–exo isomerism of the norbornene dimethanol strongly affects the formation of hydrogen bonding. A higher fraction of intra-unit H-bonds in H-PddNBdOH-co-PNB increases the chain rigidity, which leads to greater free volume hole size and higher oxygen permeability as compared to H-PdxNBdOH-co-PNB.

5.1 Introduction

EVOH is a random copolymer of ethylene and vinyl alcohol, which has one of the lowest oxygen permeability among the commonly used packaging polymers.[1, 2] It is due to the formation of H-bonds, which reduces the free volume in the system. In general, the

commercial production of EVOH is a step-process which involves free radical polymerization of vinyl acetate and ethylene monomers followed by saponification.[3, 4] Despite its excellent barrier properties; however, EVOH is very sensitive to humidity due to its hygroscopic nature. At high OH content, water molecules would plasticize the copolymer and weaken inter- and intramolecular hydrogen bonding, which leads to an increase in free volume which contributes to an undesirable decrease in gas barrier performance.[1, 5]

A norbornene-based EVOH copolymer mimic, hydrogenated poly(norbornene dimethanol)-co-polynorbornene (H-PNBdOH-co-PNB), was designed to achieve high barrier polymer with low hygroscopicity. Since the OH bearing repeat unit of the H-PNBdOH-co-PNB has a low overall O/C ratio of 2/9 as compared to that of vinyl alcohol (1/2), it may be possible to incorporate greater hydroxyl content without sacrificing barrier performance due to plasticization. On the other hand, different spatial positions of OH groups introduced by the stereoisomerism of the norbornene dimethanol may influence the hydrogen bonding formation in copolymer systems and lead to different gas barrier performance. Therefore, two H-PNBdOH-co-PNB copolymers with endo, endo, and endo, exo norbornene dimethanol units were investigated for the influence of stereochemistry on hydrogen bonding organization and, correspondingly, permeability.

In Chapter III, we managed to probe the hydrogen bond organization in dendritic polymer via MD simulation and study the correlation between the formation of H-bonded clusters and the dielectric properties. Then a question was poised that whether we could extend a similar study to linear systems. Hence, in this chapter, MD simulation and H-bond

analysis were performed on these two hydroxylated linear polymer systems to investigate the correlation between gas permeability and H-bond formation.

5.2 Experimental Section

5.2.1 Materials and sample preparation

The hydrogenated poly(endo, endo-norbornene dimethanol)-co-poly(norbornene) (H-PddNBdOH-co-PNB) and poly(endo, exo-norbornene dimethanol)-co-poly(norbornene) (H-PdxNBdOH-co-PNB).were kindly provide by Simon Research Group (SRG). The copolymers were synthesized via ring-opening metathesis polymerization (ROMP) catalyzed via a ruthenium-based, Grubb's third-generation catalyst. The composition of the norbornene component was targeted at 10 mol%. Each polymer was synthesized via two different methods: slow addition and one-pot methods. The prepared samples were denoted as H-aPddNBdOH-co-bPNB, where a and b stand for the molar percentage of the norbornene dimethanol and norbornene content, respectively.

5.2.2 Experimental methods

Polymer films were melt pressed in a Carver Press (4386) at 2000 psi, 10 to 20 ^{o}C above their measured melting temperature (T_m) determined by DSC. Synthesized polymer (~1g) was placed between two fiber glass-lined metal plates with 200 um metal shim spacers.

The density of each sample was determined by using the Archimedes' principle. Detailed procedures were described in Chapter II.

The average free volume hole-size of all the melted pressed samples at room temperature was experimentally probed using positron annihilation lifetime spectroscopy (PALS). Positrons ($e+$) are positively charged antiparticles of the electron, which undergo annihilation events when combined with electrons. When emitted to condensed materials, a free positron can bound with an electron, forming a positron-electron pair which is termed as positronium atom (Ps). Electrons and positrons with the opposite spin states form para-positronium (*p*-Ps), and those with the same state form ortho-positronium (*o*-Ps). The o-Ps can last for a few nanoseconds till it picks off an electron with antiparallel spin.[6] Hence, the lifetime of the *o*-Ps (τ_3) can be utilized to determine the free volume hole sizes in the samples using the following equation.

$$\tau_3 = \frac{1}{2}\left[1 - \frac{R}{R+d} + \frac{1}{2\pi} sin\left(\frac{2\pi R}{R+d}\right)\right]^{-1} \quad (34)$$

where R is the average hole radius, and d = 0.1656 nm is the empirically determined electron layer thickness. The average size of a free volume hole can then be calculated as $vh = 4/3\pi R^3$.[6]

PALS experiments were conducted with a fast-fast coincidence system, which was described elsewhere.[7, 8] PALS samples were prepared by cutting the polymer films into small disks with 1cm in diameter, stacking them together till the total thickness reached ~1mm, and then wrapping them with aluminum foil. Two samples were prepared for each polymer in order to sandwich the Na^{22} positron source. All the samples were vacuum dried overnight prior to tests. Each measurement took over an hour, obtaining a total of 1×10^6 counts in the resulting PALS spectrum. The PALS spectra were processed

using PATFIT-88 software. The error associated with determining τ3 values using this software was approximately ±2%.

Oxygen permeability was measured at 23 ºC, 0% relative humidity (RH), and 1 atm partial oxygen pressure difference using a commercially manufactured diffusion apparatus OX-TRAN® 2/21 ML (MOCON). To avoid the overflow of the oxygen sensor, each sample was sandwiched between two aluminon foil masks with an exposed area of 5 cm^2 and was tested using 4% O_2/N_2 gas. The oxygen transmission rate was then recalculated for 100% O_2.

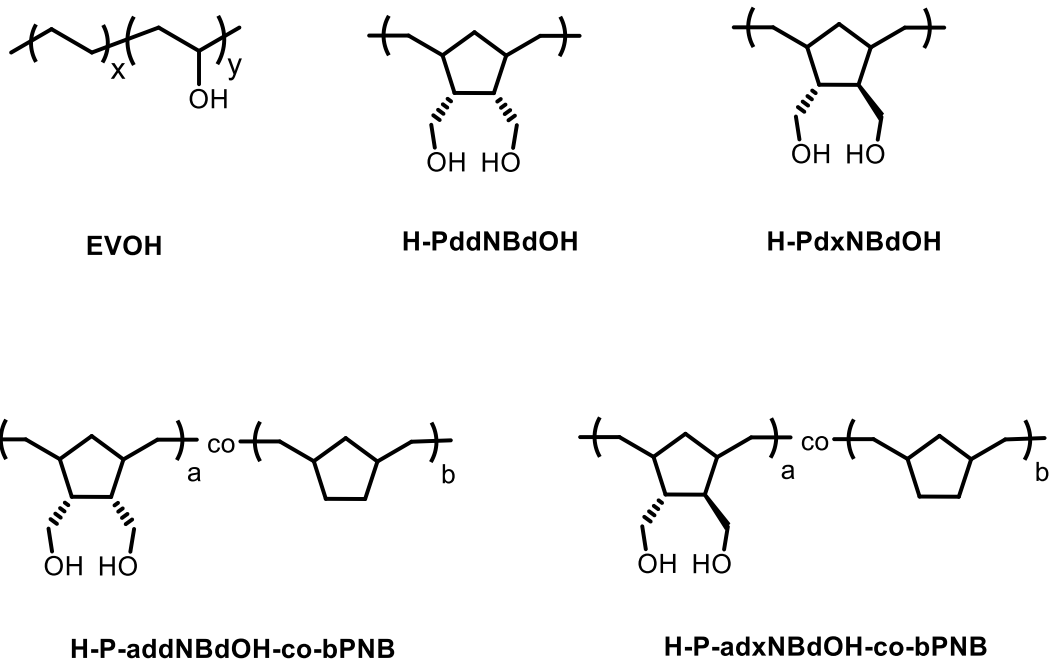

Figure 5.1 *Chemical structures of all simulated systems.*

MD simulations were used to model the structures of EVOH, H-PNBdOH homopolymer, H-PddNBdOH-co-PNB, and H-PdxNBdOH-co-PNB copolymer systems which are shown in Figure 5.1.

Simulation studies were conducted using Material Studio (Accelrys Software, Inc., San Diego) and Large-scale Atomic/Molecular Massively Parallel Simulator (LAMMPS). The vinyl alcohol content of modeled EVOH was set at 44.4% (mol/mol) to match the OH/C ratio of the H-PNBdOH homopolymer, which is 2/9. DP of each polymer chain was set to 150. In Material Studio, an amorphous cell was first constructed for each system with a starting density of 0.4 g/cm3 using the CVFF forcefield. The amorphous cell of EVOH contains 20 molecules, and those of NBdOH-containing polymers contain 10 molecules. Subsequently, using LAMMPS, all the systems were subjected to energy minimization followed by MD runs of alternating NVT and NPT ensembles, between 650 K and 298 K and 750-0.1 MPa to obtain a relaxed amorphous cell at 298 K and 1 atm. The atom-based summation method with a cut-off radius of 20 Å was used for all energy calculations unless otherwise mentioned. The appropriateness of the forcefield and the simulation protocol adopted for the systems were verified by comparing the final densities obtained from simulations with corresponding densities determined experimentally. In the final stage of the simulation, 0.1 ns production runs (NVE ensembles) with a time step of 1 fs and frame-saving frequency of 1ps were performed, creating final trajectory files consisting of 100 frames, which were used for further analysis. Ewald summation method was used in the last NVT and NPT runs and the following NVE ensemble to increase the accuracy of the calculation. Hydrogen bonds in each amorphous cell were studied by a 'TraceHbonds' using the trajectory files created in the production run. The H-bond was defined by a maximum hydrogen acceptor distance of 2.5 Å and a minimum donor-acceptor angle of 90°. Inter- and intramolecular, intra-unit H-bonds were also identified using the 'TraceHbonds' software.

5.3 Results and Discussion

5.3.1 Oxygen permeability

The results of barrier tests for the H-PNBdOH-co-PNB copolymer systems were listed in Table 5.1, where the actual molar content of the norbornene dimethanol of each polymer was listed in the brackets. In general, endo, exo systems display lower flux and permeability as compared to the endo-endo ones. With the same OH content, H-P-10(12.2)ddNBdOH-co-90PNB exhibits much higher permeability than H-P-10(12.1)dxNBdOH-co-90PNB, which suggest that stereochemistry of the norbornene dimethanol may have a strong effect on the gas permeability. Within the endo-endo and endo, exo systems, since the actual contents of OH of polymers prepared via one-pot and slow addition are not the same, it is not so clear that whether the resulting differences in sequence would affect the gas barrier properties.

Table 5.1 *Flux and permeability of H-PNBdOH-co-PNB copolymers*

Samples	Flux (cc/m2-day))	Permeability (cc-cm/m2-day-atm)
H-P-10(5.8)ddNBdOH-co-90PNB-one-pot	367.50	8.783
H-P-10(12.2)ddNBdOH-co-90PNB-slow addition	2330	62.67
H-P-10(9.1)dxNBdOH-co-90PNB-one-pot	97.72	2.304
H-P-10(12.1)dxNBdOH-co-90PNB-slow addition	69.274	1.756

Regardless of different synthetic methods, the permeability of the samples exhibits a decreasing trend with increasing OH content except for H-P-10(12.2)ddNBdOH-co-

90PNB. The decreasing trend of permeability against OH content is due to the increasing secondary interaction induced by hydrogen bonding, which squeezes out the free volume. As shown in Figure 5.2, except H-P-10(12.2)ddNBdOH-co-90PNB, the permeability values of the rest three polymers matched very well with the permeability of EVOHs with same OH content, which indicates that polynorbornene based can also obtain excellent barrier properties as EVOH be by introducing OH content.

Still, the why H-P-10(12.2)ddNBdOH-co-90PNB is off the trend is unclear. As the permeability is strongly affected by the hydrogen bonding, it is hypothesized that the chemical stereochemistry of the norbornene methanol may affect the formation of hydrogen bonding.

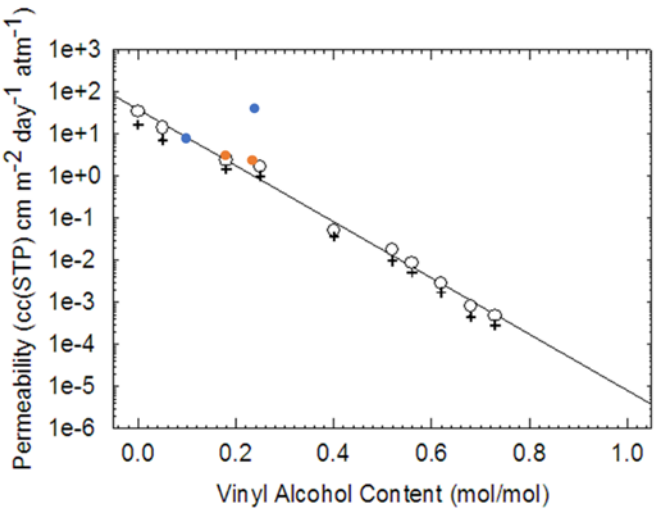

Figure 5.2 *Permeability of EVOH systems as a function of the vinyl alcohol content. The blue and orange points represent the permeability of H-P-ddNBdOH-co-PNB.and H-P-dxNBdOH-co-PNB, respectively.*

5.3.2 PALS

The free volume hole size of each polymer sample determined by PALS was listed in 5.2. In general, the free volume hole size decreases with the increase of OH content, which agrees well with the permeability results. In terms of stereoisomerism, H-P-10(12.2)ddNBdOH-co-90PNB displays a significantly larger hole size (91.4 $Å^3$) than its endo, exo isomer (83.1 $Å^3$), suggesting that the spatial arrangements of the methanol arms may affect the packing of the polymer chains.

Since H-P-10(5.8)ddNBdOH-co-90PNB is not available for the PALS measurements, H-P-10(6.5)ddNBdOH-co-90PNB, which has a close OH content, was measured instead. However, it shows a very high free volume hole size as compared to that of H-P-10(12.2)ddNBdOH-co-90PNB, which contradicts with the permeability data. This suggests that the structures and properties of endo-endo systems are not stable from batch to batch.

Table 5.2 *Free volume hole sizes of H-PNBdOH-co-PNB copolymers.*

Polymer	Avg. Free Hole Volume ($Å^3$)
H-P-10(5.8)ddNBdOH-co-90PNB-one-pot	NA
H-P-10(6.5)ddNBdOH-co-90PNB-one-pot	101.2 ± 4.01
H-P-10(12.2)ddNBdOH-co-90PNB-slow addition	91.4 ± 4.31
P-10(9.1)dxNBdOH-co-90PNB-one-pot	85.5 ± 2.86
H-P-10(12.1)dxNBdOH-co-90PNB-slow addition	83.1 ± 4.81

5.3.3 MD Simulation

The appropriateness of simulation methodology was verified by comparing the final density of each system with the experimental values. As shown in Table 5.3, the simulated densities agree well with the experimental data. Specifically, the simulated densities of H-PddNBdOH and H-PdxNBdOH, which are1.116 and 1.114 g/cm^3 respectively, are only by 12% and higher than the experimental density of hydrogenated PNB, which is 0.995 g/cm^3. The simulated densities of H-PddNBdOH-*co*-PNB copolymers are in the range of 0.950 to 0.996 g/cm^3, deviate about 7.6~3.1% from experimental density of H-P-10(12.2)ddNBdOH-co-90PNB, which is 1.028 g/cm^3; those of H-PdxNBdOH-*co*-PNB copolymers are in range of 0.966 to 0.995 g/cm^3, are about 6.1~9.1% lower than the experimental density of H-P-10(9.1)dxNBdOH-co-90PNB, which is 1.056 g/cm$^{.3}$.

Table 5.3 *Comparison between the simulated density and the experimental value of the simulated systems.*

Systems	Simulated Density (g/cc)	Experimental Density (g/cc)
EVOH	0.991	1.06(extrapolated from experimental data)
H-PddNBdOH	1.116	0.995 (literature value for h-polynorbornene)
H-P-10ddNBdOH-co-90PNB	0.950	1.028 (experimental value of H-P-10(12.2)ddNBdOH-co-90PNB)
H-P-20ddNBdOH-co-80PNB	0.976	

Table 5.3 (continued)

H-P-30ddNBdOH-co-70PNB	0.996	1.028 (experimental value of H-P-10(12.2)ddNBdOH-co-90PNB)
H-PdxNBdOH	1.114	0.995 (literature value1 h-polynorbornene)
H-P-10dxNBdOH-co-90PNB	0.966	1.056 (experimental value of H-P-10(9.1)dxNBdOH-co-90PNB 1.056 (experimental value of H-P-10(9.1)dxNBdOH-co-90PNB
H-P-10dxNBdOH-co-90PNB	0.972	
H-P-10dxNBdOH-co-90PNB	0.995	

The density of EVOH with 44.4% alcohol content was determined via extrapolating the data from the linear fit of the densities of EVOH copolymers against alcohol content. All the density points shown in Figure 5.3 were measured using a density gradient column constructed from a solution of toluene and carbon tetrachloride in accordance with ASTM-D Standard 1505 Method B. The simulated density of EVOH (0.991 g/cm^3) is only by 6.5% lower than the experimental density of EVOH (1.06 g/cm^3).[9]

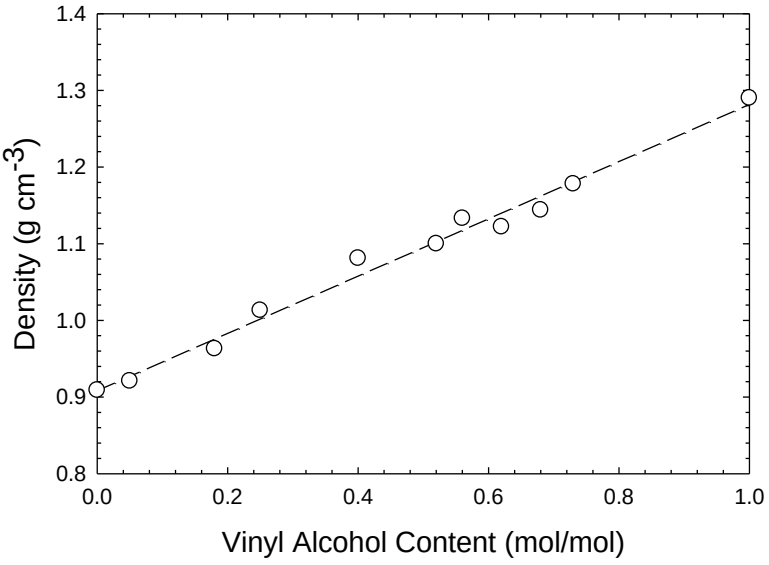

Figure 5.3 *Density as a function of vinyl alcohol content in EVOH copolymers.*[9]

Total number of H-bonds, degree of H-bonding, number and percentage of intramolecular H-bond and intra-unit H-bonds determined for all the simulated systems via using 'TracedHbonds' were listed in Table 5.4. The degree of H-bonding is defined as the number of H-bonds divided by the number of OHs. The intra-unite H-bonds are referring to the H-bonds formed within the same norbornene dimethanol repeat unit. The percentage of intramolecular and intra-unite H-bonds were determined as the number fraction of corresponding H-bonds in the total H-bonds.

Comparing the hydrogen bonding formation of the three homopolymers, the degree of hydrogen bonding of follows the trend: H-P*dd*NBdOH (63.9%) >EVOH (58.5%)> H-P*dx*NBdOH (49.3%). Interestingly, the fraction of intramolecular H-bonds in these homopolymers follows the same order: H-P*dd*NBdOH (61.9%) >EVOH (54.2%)> H-P*dx*NBdOH (30.6%). While EVOH displays little preference of forming inter- or intra-molecular H-bonds, the endo, endo homopolymer shows a propensity of forming intra-

molecular H-bonds whereas the endo, exo one exhibits the opposite tendency. Moreover, higher intra-unit H-bonding contribution was found in the endo, endo homopolymer (23.1%) than the endo,exo one (7.0%). This suggests that stereochemistry plays an important role in hydrogen bonding formation in norbornene dimethanol based systems.

Copolymers show a lower degree of hydrogen bonding than the homopolymers as a result of reduced OH content, especially for endo, exo copolymers, of which degree of H-bonding is about half of endo, exo homopolymer. Similar to homopolymers, endo, endo copolymers also exhibit a higher degree of hydrogen bonding, a higher fraction of intramolecular and intra-unit H-bonds than their endo, exo counterparts. This suggests stereochemistry also significantly affects the hydrogen bonding formation in copolymer systems. Moreover, both endo, endo, and endo, exo copolymers display higher proportions of the intramolecular and intra-unit H-bonds as compared to corresponding homopolymers. It should be noted that the preference of endo, endo structure for forming intra-unit H-bonds is exaggerated in copolymers as ~60% of the H-bonds in endo, endo copolymers are formed within the same repeat unit. This can be explained as norbornene dimethanol units become isolated in the copolymer chain, leaving the neighboring OH within the same repeat unit the most feasible one for H-bond formation.

Table 5.4 *Results of H-bond analysis for all simulated systems.*

Polymer	Total H-bonds	Deg. of H-bonding	Intramolecular. H-bonds	Intra-unit H-bonds
EVOH	784.3	58.5%	542.0 (54.2 %)	NA
H-P*dd*NBdOH	1916.3	63.9%	1186.7 (61.9 %)	442.7 (23.1 %)

Table 5.4 (continued)

H-P*dx*NBdOH	1479.0	49.3%	453.0 (30.6 %)	104.0 (7.0 %)
H-P-10*dd*NBdOH-co-90NB	145.4	48.5%	125.3 (86.2 %)	89.8 (61.8 %)
H-P-20*dd*NBdOH-co-80NB	318.6	53.1%	254.2 (79.8 %)	185.5 (58.2 %)
H-P-30*dd*NBdOH-co-70NB	490.1	54.5%	392.2 (80.0 %)	280.4 (57.2 %)
H-P-10*dx*NBdOH-co-90NB	59.9	20.0%	37.3 (62.4 %)	28.5 (47.5 %)
H-P-20*dx*NBdOH-co-80NB	149.5	24.9%	73.1 (48.9 %)	51.3 (34.3 %)
H-P-30dxNBdOH-co-70NB	295.5	32.8%	128.7 (43.5%)	81.6 (27.6%)

With increasing OH content, both endo, endo, and endo, exo copolymers show decreases in degree of H-bonding and increases in the fractions of intramolecular and intra-unit H-bonds. This is because that as OH concentration gets higher, OHs from different chains become more feasible, leading to an increase in the fraction of intermolecular H-bonds. Nevertheless, since the endo, endo structure favors intra-unit H-bond, the fraction of intra-unit H-bond decreases slower with increasing OH content (from 61.8% to 57.2%) in endo, endo copolymers as compared to endo, exo ones (from 47.5% to 34.3%).

Considering the permeability PALS measurements in conjunction with the simulation studies, we can conclude that higher free volume hole size of H-P*dd*NBdOH-co-PNB films, which contributes to higher oxygen permeability, is correlated with their higher fraction of intra-unit H-bonds. This can be explained as the formation of intra-unit H-bonds may increase the chain rigidity which reduces the packing density and hence

increases the free volume hole size. Moving forward towards high-performance barrier materials, an appropriate balance of inter-, intramolecular, and intra-unit H-bonding organization is necessary to achieve efficient permeability characteristics, where an excess of intra-unit H-bonding has been proved to have a negative impact on oxygen permeability.

5.4 Conclusion

The oxygen permeability of H-PddNBdOH-co-PNB and H-PddNBdOH-co-PNB was measured and compared via MOCON. With about 10% NBdOH content, H-PddNBdOH-co-PNB exhibits much higher permeability than H-PdxNBdOH-co-PNB, of which permeability is comparable to EVOH with same OH content. PAL measurements revealed that the free volume hole size in the endo, endo copolymer is much higher than that in the endo, exo counterparts. The H-bond analysis was performed on the simulated structures of EVOH, PNBdOH homopolymers, and H-PNBdOH-co-PNB copolymers with NBdOH content from 10% to 30%. It was discovered chemical stereochemistry of the norbornene methanol affects the formation of hydrogen bonding. For both homo- and copolymers, endo, endo structure has a preference of forming intra-unit H-bonds, which contributes to a higher fraction of intramolecular H-bonds and a higher degree of hydrogen bond than endo, exo polymers. This propensity is even greater in copolymers as the OHs are more isolated which leaves the neighboring OH the only choice for H-bond formation. The fraction of intra-unit H-bonds in copolymers reduces with OH content as OHs from different chains become more feasible. Therefore, it is concluded that higher oxygen permeability of the H-PddNBdOH-co-PNB is due to its higher fraction of intra-

unit H-bonds, which increases the chain rigidity and hence increases free volume hole size.

5.5 References

1. Lagaron, J. M.; Catalá, R.; Gavara, R., Structural characteristics defining high barrier properties in polymeric materials. *Mater. Sci. Technol.* **2004,** *20* (1), 1-7.
2. Mokwena, K. K.; Tang, J., Ethylene vinyl alcohol: a review of barrier properties for packaging shelf stable foods. *Crit. Rev. Food Sci. Nutr.* **2012,** *52* (7), 640-650.
3. Ramakrishnan, S.; Chung, T. C., Poly(5-hydroxyoctenylene) and its derivatives: synthesis via metathesis polymerization of an organoborane monomer. *Macromolecules* **1990,** *23* (21), 4519-4524.
4. Iwanami, T.; Hirai, Y., Ethylene vinyl alcohol resins for gas-barrier material. *Tappi J.* **1983,** *66* (10), 85-90.
5. Maes, C.; Luyten, W.; Herremans, G.; Peeters, R.; Carleer, R.; Buntinx, M., Recent Updates on the Barrier Properties of Ethylene Vinyl Alcohol Copolymer (EVOH): A Review. *Polym. Rev.* **2018,** *58* (2), 209-246.
6. Consolati, G.; Quasso, F., Morphology of Free-Volume Holes in Amorphous Polymers by Means of Positron Annihilation Lifetime Spectroscopy. In *Polymer Physics*, John Wiley & Sons, Inc.: 2010; pp 391-419.
7. Kobayashi, Y.; Zheng, W.; Meyer, E.; McGervey, J.; Jamieson, A.; Simha, R., Free volume and physical aging of poly (vinyl acetate) studied by positron annihilation. *Macromolecules* **1989,** *22* (5), 2302-2306.
8. Kluin, J. E.; Yu, Z.; Vleeshouwers, S.; McGervey, J. D.; Jamieson, A. M.; Simha, R.; Sommer, K., Ortho-positronium lifetime studies of free volume in polycarbonates of different structures: influence of hole size distributions. *Macromolecules* **1993,** *26* (8), 1853-1861.

9. Brandt, J. P. The influence of nanoporous crystalline structure on low molecular weight mass transport in syndiotactic polystyrene. Ph.D. Thesis, The University of Southern Mississippi, 2010.

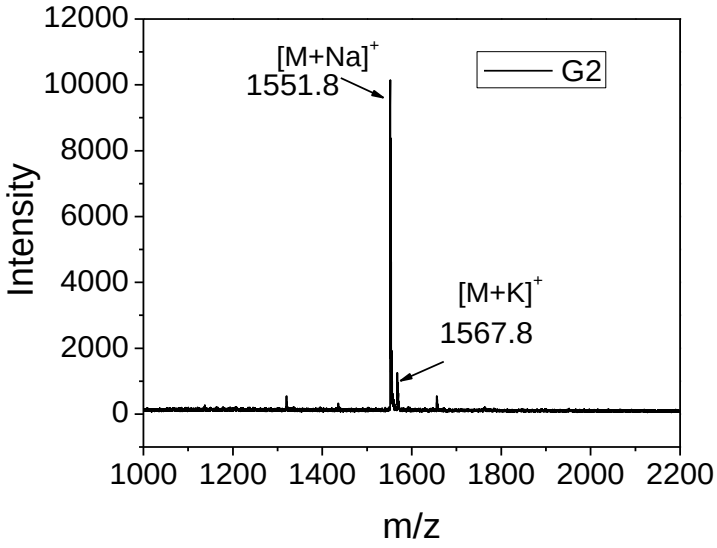

Figure A.1 *MALDI-TOF trace for the dendrimer G2 with a theoretical molecular weight of 1529.5 Da.*

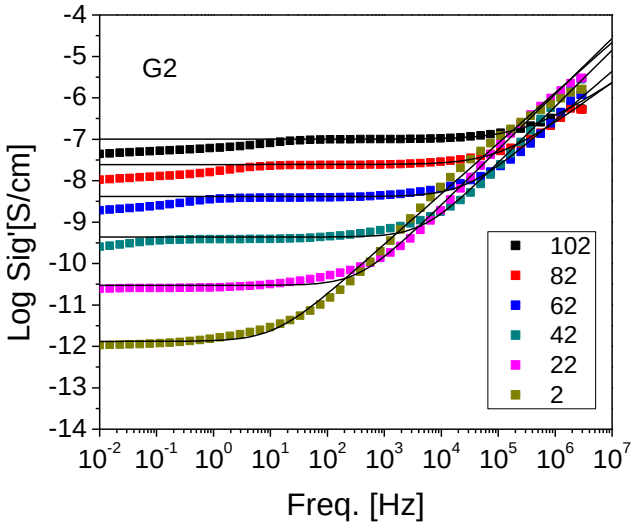

Figure A.2 *The real part of the complex conductivity, σ', as a function of frequency and the Jonscher fit for G2 (when the electrode polarization effect is not significant)*